technische universität
dortmund

Dissertation zur Erlangung des akademischen Grades
Doctor rerum naturalium (Dr. rer. nat.)
in der Physik

Mobile-Ion and Matrix Dynamics in Dinitrile- and Cycloalcohol-based Lithium Electrolytes studied by Solid-State NMR, Dielectric Spectroscopy and Rheology

Sofiane Lansab
geboren in Oran

AG Böhmer
Fakultät Physik
Technische Universität Dortmund

Erstgutachter:	Prof. Dr. Roland Böhmer
Zweitgutachter:	Prof. Dr. Claudia Schmidt
Abgabedatum:	20.03.2024

Abstract

Dinitrile-based lithium electrolytes were investigated through a comprehensive approach integrating nuclear magnetic resonance (NMR), dielectric spectroscopy, and viscosimetry. The reorientational motion within the succinonitrile-glutaronitrile (SN-GN) matrix was elucidated and the impact of lithium salt additions examined. Effect of enhanced molecular rigidity was investigated by incorporating fumaronitrile (FN) molecules with double central bond (C=C). Additionally, deuterated SN facilitated ^{2}H NMR investigations of the reorientational dynamics, while ^{7}Li NMR probed the charge carrier's dynamics. Viscosimetry, along with proton and lithium diffusion NMR measurements, offered insights interpreted via a paddle-wheel mechanism. Moreover, an exhaustive compilation and comparison of all available conductivity data for nitrile-based electrolytes was performed, with a specific focus on contextualizing the findings of this research. Ultimately, a comparative analysis was undertaken between the SN-GN matrix and an alternative hosting matrix comprised of cyclohexanol and cyclooctanol (HEX-OCT). This project involved dielectric spectroscopy and NMR investigations on various HEX-OCT-based electrolyte samples, expanding the approach employed for the SN-GN matrix on another substance class. In contrast to the dinitrile mixture, the HEX-OCT-based Li electrolytes were found to exhibit a revolving door mechanism, with volume effects playing a lesser role.

Kurzfassung

Dinitril-basierte Lithiumelektrolyte wurden durch einen umfassenden Ansatz unter Einbeziehung von Kernspinresonanz (NMR), dielektrischer Spektroskopie und Viskosimetrie untersucht. Die Reorientierungsbewegung innerhalb der Succinonitril-Glutaronitril (SN-GN)-Matrix wurde aufgeklärt, und die Auswirkungen von Zugaben von Lithiumsalzen wurden untersucht. Der Effekt einer erhöhten molekularen Steifigkeit wurde durch den Einbau von Fumaronitril (FN)-Molekülen mit doppelter Zentralbindung (C=C) untersucht. Darüber hinaus ermöglichte deuteriertes SN ^{2}H-NMR-Untersuchungen der Reorientierungsdynamik, während ^{7}Li-NMR die Dynamik der Ladungsträger detektiert. Viskosimetrie sowie Protonen- und Lithiumdiffusions-NMR-Messungen lieferten Erkenntnisse, die über einen Schaufelradmechanismus interpretiert wurden. Außerdem wurde eine umfassende Zusammenstellung und ein Vergleich aller verfügbaren Leitfähigkeitsdaten für dinitrilbasierte Elektrolyte durchgeführt, wobei der Schwerpunkt auf der Kontextualisierung der Ergebnisse dieser Forschung lag. Schließlich wurde eine vergleichende Analyse zwischen der SN-GN-Matrix und einer alternativen Trägermatrix, bestehend aus Cyclohexanol und Cyclooctanol (HEX-OCT), durchgeführt. Dies beinhaltete die dielektrische Spektroskopie und NMR-Untersuchungen an verschiedenen Elektrolytproben auf HEX-OCT-Basis, um den für die SN-GN-Matrix verwendeten Ansatz auf eine weitere Substanzklasse auszuweiten. Im Gegensatz zur Dinitrilmischung wurde festgestellt, dass die HEX-OCT-basierten Li-Elektrolyte einen Drehmechanismus aufweisen, wobei Volumeneffekte eine geringere Rolle spielen.

Acknowledgements

I would like to extend my sincere gratitude to *Prof. Dr. Roland Böhmer* for providing me with the opportunity to pursue a PhD within his research group. I am deeply grateful for his unwavering support, extensive expertise, and patient guidance throughout the duration of my research journey.

I extend my appreciation to *Prof. Dr. Claudia Schmidt* for her willingness to evaluate my research work and for her sincere and invaluable guidance in the field of NMR, which has been instrumental in shaping my academic pursuits from my undergraduate studies to my current doctoral research.

I wish to acknowledge *Dr. Joachim Beerwerth* for his consistent availability and thorough explanations on NMR and electronics, which have greatly enriched my understanding in these areas. Special thanks are also due to *Philipp Münzner* and *Dr. Kevin Moch* for their assistance in dielectric spectroscopy and rheology.

I am grateful to all members of the research group for fostering a friendly and collaborative atmosphere, which has positively contributed to my research work. I will sincerely miss working with such colleagues.

I would also like to express my appreciation to my circle of friends, whose unwavering support and encouragement have been a constant source of strength throughout this challenging journey of completing a PhD thesis. Special thanks to *Dr. Davide Vodola* for his invaluable advice and unwavering support.

Un grand merci à mes parents pour leurs sacrifices et leur soutien indéfectible tout au long de cette aventure. Je suis conscient du poids financier et mental que mon départ en Europe pour mes études a pu représenter. Je leur suis ainsi qu'à tous mes frères et ma soeur, infiniment reconnaissant.

Lastly, I am very grateful to my dearest friend, *Raffaele*, whose words of encouragement and friendship will forever remain in my heart despite his untimely departure.

Contents

1 Introduction

Over the past two decades, battery devices have undergone remarkable advancements, marking a crucial milestone since the discovery of the galvanic cell by Luigi Galvani in the late 18^{th} century. These breakthroughs have emerged from extensive research and a keen exploration of diverse battery materials and concepts. As of today, a substantial number of materials have been investigated ranging from simple organic substances to highly complexed compounds. The heightened interest in batteries is evident in the significant increase of more than 7000 patents related to electrical storage in 2018, marking a sevenfold rise compared to the year 2000.[1]

In addition to being a crucial component in every portable device and a determining factor in the lifespan of our daily-used electronics, batteries play a key role in the successful transition to green energy solutions. Indeed, many green energy production systems rely on natural factors, such as wind speed for wind turbines or daylight for photovoltaic modules. However, these natural factors do not always align with electricity demand peaks, often resulting in insufficient or excessive energy production.

In this context, energy storage systems, such as batteries, have proven to be efficient solutions for avoiding grid overload.[2, 3] Lithium ion batteries in particular, have gained major importance and are subject of numerous current research works.[4–8] This interest has opened the door for a wide range of applicability alongside with unprecedented challenges such as Li dendrites growth or limited temperature range of the conductivity.[9–11] One focus of battery research to overcome these challenges consists in studying of lithium-based electrolytes.[12–15] Indeed, the electrolyte is a critical component in the cell since it is directly involved in the Li ion migration.[16, 17] Thus, finding the right electrolyte material can have a significant impact on the overall performances of the battery.

In recent years, dinitrile-based (N≡C–$(CH_2)_n$–C≡N) electrolytes have been subject to extensive investigations.[18–29] Previously considered unsuitable for battery applications due to their inability to form a solid-electrolyte-interphase (SEI), they have lately undergone several molecular dynamics studies.[30–36] In particular for their impressive room-temperature conductivity (10^{-3} S/cm),[18] their large electromechanical stability window (up to 6 V vs. Li^+ /Li)[23] along with their low flammability. The outstanding characteristic of these electrolytes is however, their ability to form a so-called *plastic phase*.[37]

In the plastic phase, dinitrile chains occupy fixed lattice positions while retaining a certain degree of orientational freedom. The plasticity imparts high mechanical flexibility to the electrolyte, broadening its applicability from stretchable batteries to portable medical devices.

An exemplary material in this class is succinonitrile (SN, $n = 2$), which, when combined with a sufficent amount of glutaronitrile (GN, $n = 3$), exhibits both higher ionic conductivity and absence of an ordered crystalline phase.[38, 39] The temperature range of the plastic phase of this mixture depends on the proportion of GN to SN.[32] Furthermore, the addition of lithium salts, such as lithium bis(trifluoromethanesulfonyl)imide (LiTFSI) or lithium hexafluorophosphate ($LiPF_6$) to the mixture, significantly enhances the overall conductivity by almost three orders of magnitude.[39] These compelling features make this system worthy of further investigation.

In this regard, understanding the possible correlation between the molecular orientation of the dinitriles and the translational motion of the Li ions, could help elucidate the ionic transport mechanism involved in these materials. From a more general perspective, it could contribute significantly in the improvement of ionic migration in plastic electrolytes and thus provide useful guidelines for their conception. In this sense, investigating the impact of incorporating longer molecular chains or increased molecular rigidity (e.g., fumaronitrile in the SN-GN mixture) on the molecular dynamics and the ionic conductivity can be particularly helpful. Moreover, comparison with other previously investigated plastic crystals (PCs), such as cycloalcohols (e.g., cyclohexanol and cyclooctanol), may offer valuable insights, especially considering some contradictory observations reported in the literature regarding the potential coupling between matrix and charge carrier.

In addition to their suitability as plastic electrolytes, dinitriles exhibit a high dipole moment,[40] enabling them to dissolve significant amounts of lithium salts. This characteristic has paved the way for further investigations, with a focus on highly concentrated electrolytes.[41, 42] In fact, dinitriles can be studied from a different perspective as *deep eutectic solvents*. These types of electrolytes are known to demonstrate extraordinary properties, including high reductive and oxidative stability, as well as an elevated carrier density.[43–47] All of these factors hold great promise for advancements in the field of battery technology.

In this context, Nuclear Magnetic Resonance (NMR) has established itself as a powerful technique to investigate lithium electrolytes.[48–56] Indeed, a *sine qua non* condition for NMR spectroscopy, is the existence of a spin number ($I \neq 0$) or in other terms, the existence of a stable isotope. The lithium nucleus happens to have two of such, ^{6}Li ($I = 1$) and ^{7}Li ($I = 3/2$). Under NMR conditions, each isotope would resonate at a unique *Larmor frequency* directly correlated with its immediate environment and the type of interactions involved. Thus, one can access valuable information on the dynamics of the charge carrier. With that in mind, we investigate in this work dinitrile-based plastic and liquid electrolytes using NMR spectroscopy. Proton (^{1}H) and deuterium (^{2}H) NMR are employed to gain insights into the system's dynamics from the matrix perspective. ^{7}Li NMR on the other hand provides a good tool to acces the dynamics of the Li ions within the plastic structure. Additionally, combining NMR results with other spectroscopy techniques, such as dielectric spectroscopy, suited for molecules with high dipolar moments like SN and GN, and viscosity data obtained through rheology, facilitates the understanding of ionic conductivities and molecular viscosities in the matrix.

2 Plastic crystals

In the liquid state, the molecules of a substance exhibit full degree of freedom as they are interconnected by weak intermolecular bonds. These bonds can be disrupted by rising temperatures, causing a transition to the gaseous state, or by cooling, resulting in crystallization if the material reaches a low enough temperature.

In addition, some materials possess an intermediate, thermostable state between the liquid and solid phases, commonly referred to as the plastic phase. These materials constitute a unique class of substances and are called *plastic crystals*. In the plastic phase, the constituent polyatomic molecules enjoy a certain degree of freedom, either rotational or conformational. Rotatory phases in particular, have molecules that occupy fixed lattice positions while engaging in unrestricted thermal rotatory motions.

In this work, special attention is placed on exploring the characteristics of the plastic phase and plastic crystals; for a comprehensive understanding of the liquid phase, readers are invited to consult classical texts on the state of matter.

Table 2.1 presents some relevant parameters of the PCs investigated in this study. Data for the plastic phase of camphor is provided for comparison.

Plastic crystals	Camphor	Succinonitrile	Cyclohexanol
Melting point T_m/K	453	331	297
Entropy of melting ΔS_m	2.8	2.7	1.4
Transition point T_t/K	250	235	263
Entropy of transition ΔS_t	7.6	3.8	7.45
Structure of the plastic phase	fcc	bcc	fcc (I)

Table 2.1: Characteristics of selected PCs. T_t is the transition temperature from crystal phase to the PC phase. ΔS_m and ΔS_t are the entropies of fusion and transition, respectively, in cal/deg·mol. Data were collected from ref.[57–60].

Upon reviewing table 2.1 it becomes clear that PCs possess some intriguing characteristics. In fact, they have relatively high melting points, accompanied by exceptionally low entropy of melting, ΔS_m. This obervation was initially reported by Timmermans *et al.*[61], who proposed a guideline for PCs, stipulating that ΔS_m for this type of materials should be less than 5 cal/deg·mol. However, subsequent research has demonstrated that certain PCs may deviate from this rule, exhibiting slightly higher entropy values.[57]

The plastic phase is commonly observed in simple globular-shaped molecules.[59, 61] These materials often display elevated crystallographic symmetry within a cubic structure, hence they are occasionally termed *non-amphiphilic cubic mesophases*.[62] Prominent examples of such materials include cyclohexane or methane.[59] However, it is essential to note that the cubic symmetry and molecular shape are not stringent prerequisites for the formation of a plastic phase. Orientationally disordered phases are also identified in less symmetrical molecules.[63–65] Generally, determining the crystal structure of PCs proves to be a challenging task. Molecular crystals with orientational disorder yield only a limited number of diffracted X-rays beams at low Bragg angles indicative for a high Debye-Waller factors.[59]

Upon scrutinizing the literature pertaining to PCs, it becomes evident that establishing universal guidelines for the classification of these materials remains difficult. While certain PCs may exhibit commonalities in aspects such as crystal structure or the nature of disorder, we prefer to delve into the specific characteristics of each investigated PC separately. We therefore dedicate Section 2.1 to succinonitrile and Section 2.2 to cyclohexanol.

2.1 Succinonitrile

Succinonitrile (N≡C–$(CH_2)_4$–C≡N) has been the focus of extensive research in recent years due to its distinctive properties and potential applications in battery technology.[18–22, 24, 26, 27, 30–36] Notably, succinonitrile exhibits a large electrochemical stability window and a high dissociation rate for lithium salts. The former attribute makes SN a preferred cosolvent for enhancing thermal stability in electrolytes that are inherently less stable.[66–69] The latter characteristic facilitates a high degree of lithium doping, potentially leading to improved conductivity values.

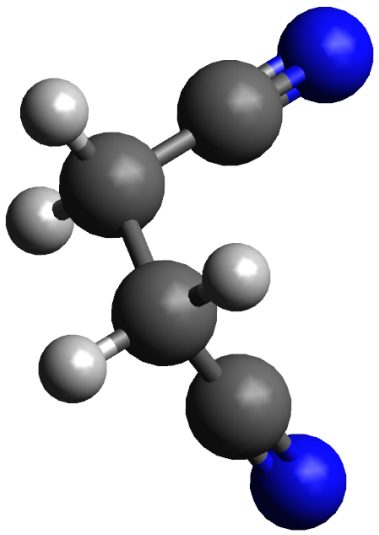

Figure 2.1: The SN molecule, here shown in the *gauche* conformation.

However, of particular significance is the existence of a plastic phase for succinonitrile. This phase manifests within the temperature range of 235 K to 330 K and is characterized by enhanced ionic conductivity upon lithium doping.[37]

In the plastic phase, succinonitrile adopts a cubic structure with *Im3m* symmetry group, featuring a lattice constant of a = 6.341 Å and containing two molecules per unit cell.[37] The molecule has three isomers, namely a *trans* conformation and two *gauche* conformations.[37] Notably, the central C–C bond in the molecule can align along the four threefold axes of the unit cell, see Figure (2.2).

The reorientational motion of SN in the plastic phase arises essentialy from its isomeric behavior. Indeed, the molecule undergoes constant isomeric reorientations, which involve 120° rotations of $H_2C–C{\equiv}N$ groups about one of the threefold axes (*trans* ⟶ *gauche*) or 90° rotations of the entire molecule about one of the fourfold axes (*trans* ⟶ *trans*). Thus, the twelve equilibrium positions resulting from this reorientational motion can be deduced as follows: each isomer can occupy three positions obtained through a 120° rearrangement about one of the four threefold axes.[37]

The population ratios of the SN isomers exhibit a temperature-dependent variation. The *trans* isomer constitutes approximately 23% of the isomeric distribution at room temperature and demonstrates an increasing prevalence with elevated temperatures.[70] Conversely, when the temperature descends below approximately 233 K, succinonitrile undergoes a phase transition into an orientation-ordered phase. In this phase, all molecules adopt the gauche conformation.[70]

The incorporation of the longer glutaronitrile chain to succinonitrile has been found to have remarkable effects on its properties.[38, 39] The resulting compound exhibits an exceptionally high ionic conductivity at room temperature. Furthermore, this addition suppresses the transition to the orientationally ordered phase, significantly enlarging the temperature window under which the plastic phase exists.

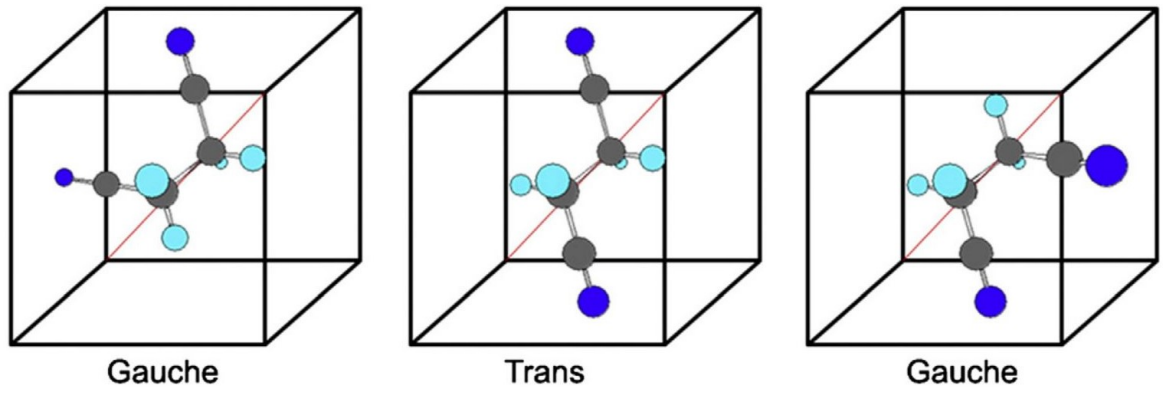

Figure 2.2: The three isomers of the SN molecule where the central C-C bond is aligned along the diagonal (red line) of the cubic unit cell. Figure taken from ref.[71].

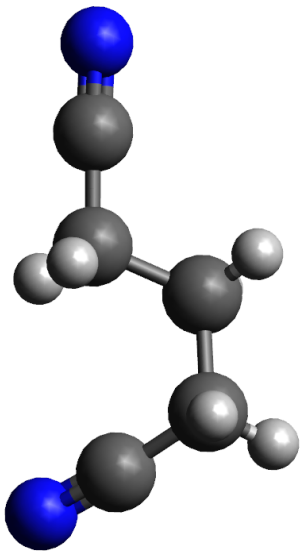

Figure 2.3: The GN molecule.

Figure 2.4 illustrates the phase diagram of the binary mixture SN-GN, as reported by Götz *et al.*[32]. When the concentration of GN in the mixture is at or below 10%, a plastic phase is observed. Within this concentration range, the PC phase cannot be supercooled. As the GN concentration increases within the range of 15% to 95%, supercooling becomes possible, resulting in the formation of a glassy material.

For high GN concentrations ranging from 70% to 80%, and at temperatures exceeding the crystallization temperature (see the shaded region in Figure 2.4), a complex behavior takes place. This behavior is contingent upon the material's thermal history and the rate at which cooling or heating is applied.[32]

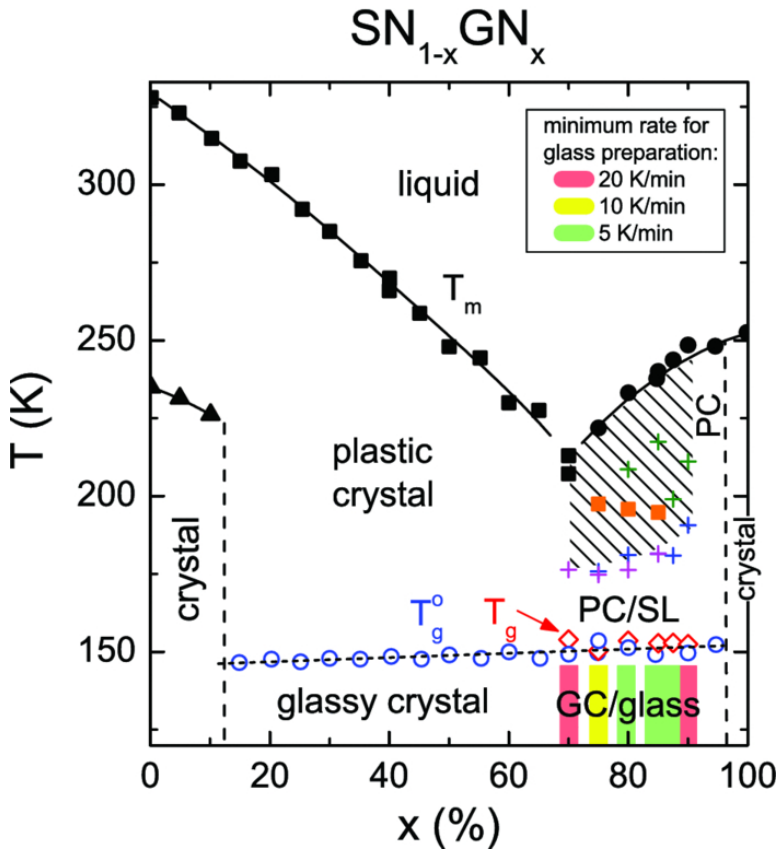

Figure 2.4: Phase diagramm of the binary mixture SN-GN as published in ref.[32].

2.2 Cyclohexanol

Cyclohexanol ($C_6H_{11}OH$) is another plastic crystal that has undergone extensive investigations.[72–79] Despite its seemingly simple structure, cyclohexanol reveals an intricate phase diagram.

Figure 2.5 illustrates a schematic diagram of cyclohexanol's phase behavior as reported by Suzuki *et al.*[79] based on the heat capacity investigation of Adachi *et al.*[72]. The phase diagram is characterized by the presence of metastable phases and a significant sensitivity to the thermodynamic trajectory. Indeed, cyclohexanol displays numerous crystalline phases, each characterized by distinct hydrogen bonding arrangements. This complex polymorphic behavior originates from the inherent conformational flexibility of the compound and its propensity for hydrogen bonding.[78]

The plastic phase of cyclohexanol, phase I, occurs within the temperature range of 298 to 265 K and features an *fcc* lattice structure. In this phase, both axial and equatorial orientational configurations of the hydroxyl group and orientational disorder of the cyclohexyl ring are included.[78] Additionally, the volume occupied by each molecule reaches its maximum in this phase (167.8 $Å^3$ at 250 K).[78] Below 265 K, cyclohexanol undergoes a phase transition into a thermodynamically stable state of perfect order, phase II.[78]

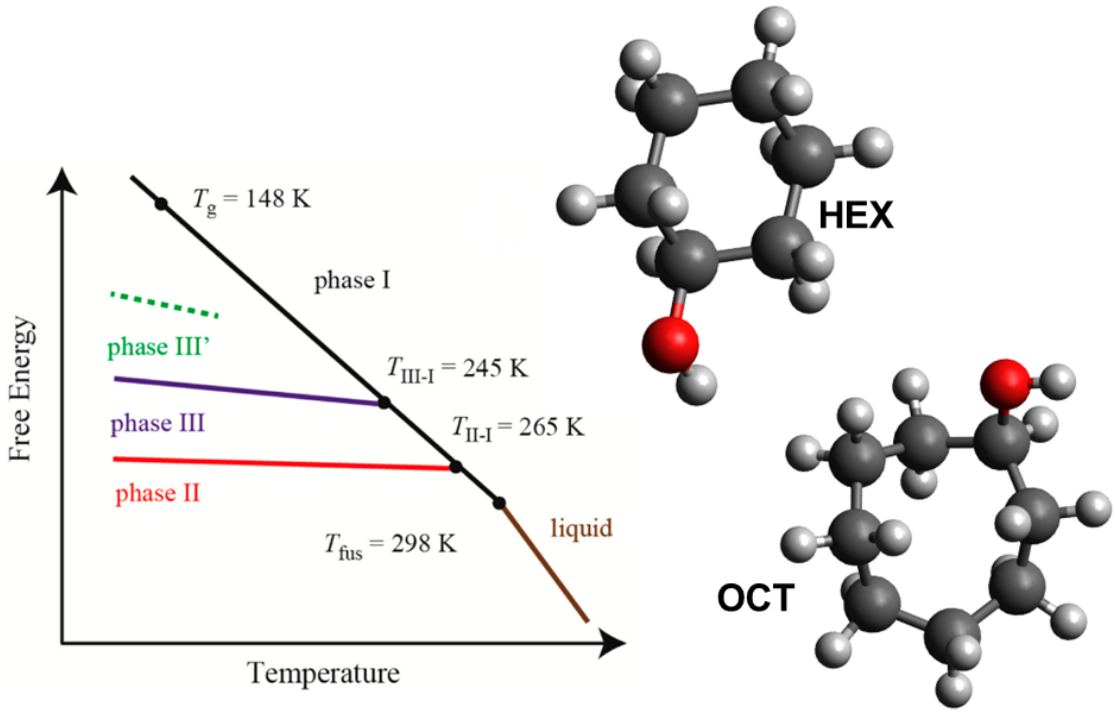

Figure 2.5: Phase behavior of cyclohexanol as outlined in ref.[79] (left). The cyclohexanol (HEX) and cyclooctanol (OCT) molecules (right).

Phase I can be supercooled below its glass transition temperature of 148 K.[79] Additionally, quenching the plastic phase to a temperature of 100 K and subsequently raising it to approximately 195 K leads to the creation of the ordered metastable Phase III.[78] The thermal treatment applied to Phase III determines its behavior: it undergoes a III–I transition at 245 K or undergoes an irreversible transformation to Phase II when heated to a range between 220 and 240 K.[78]

Furthermore, an alternative method for generating Phase III involves the creation of an intermediate fourth phase III'.[78] This fourth phase is grown from the supercooled Phase I at approximately 200 K. Phase III' is kinetically unstable and can be sustained for only 15 min.[79]

Analogous to the succinonitrile-glutaronitrile mixture, the incorporation of a longer cycloalkanol ring can be explored by adding cyclooctanol (see Figure 2.5). Indeed, Reuter *et al.*[80] conducted a dielectric spectroscopy investigation on mixtures of cyclohexanol (HEX) and cyclooctanol (OCT) doped with 1 mol% $LiPF_6$, where a "revolving door" mechanism was revealed.

In these doped cycloalcohol mixtures, the temperature dependence of the ionic conductivity closely parallels that of the reorientational relaxation, exhibiting a greater degree of similarity compared to the SN-GN mixture.[80] However, the conductivity of the doped $(HEX)_{1-x}(OCT)_x$ plastic crystals was found to be significantly lower than that observed in the dinitrile system.[80] This difference was attributed to interactions between Li ions and the polar hydroxyl groups of the ring alcohols.[80]

Different from the SN-GN system, the introduction of the larger cyclooctanol component to the smaller cyclohexanol component results in a decrease in the overall conductivity.[80] Apart from the aforementioned investigations, HEX and OCT underwent thorough additional analyses involving dielectric studies,[81–87] NMR spectroscopy,[88–91] neutron scattering,[76] and EPR spectroscopy.[92] The insights derived from these studies will be revisited as necessary when discussing the outcomes of the current research.

3 Molecular & ionic transport in plastic electrolytes

Battery research has pursued multiple strategies to enhance battery performance. These approaches typically concentrate on specific battery components, such as electrodes or electrolytes, employing various methodologies to address targeted challenges.[93–97] In this sense, efforts to enhance electrolytes have involved the utilization of diverse matrix materials, different charge carrier types, and, more recently, the incorporation of plasticizers. These methods are directed toward augmenting the overall conductivity of the material while concurrently preserving battery functionality. Additionally, advanced concepts are oriented towards addressing more challenging issues, including applicability concerns such as the absence of a solid electrolyte interphase or the growth of lithium dendrites.[98–100]

In this regard, Section 3.1 recalls the components and the operating concept of a Li ion battery, while Sections 3.2 and 3.3 revisit relevant notions regarding the glass transition and ion diffusion, respectively. Additionally, Section 3.4 delves further into dynamics correlations between the hosting matrix and the charge carrier, building upon previously reported findings.

3.1 The lithium ion battery

To comprehend the challenges associated with the conception and utilization of lithium electrolytes, it is important to first understand the operational principles of a Li ion battery. Figure 3.1 shows the distinct components of a Li ion battery throughout its charging and discharging phases. The fundamental cell typically comprises two electrodes, a positive electrode (cathode), and a negative electrode (anode), which are separated by a permeable membrane. Subsequently, the cell is filled with an electrolyte solution. Conventional materials employed for the cathode include lithium metal oxides, such as lithium cobalt(III) oxide ($LiCoO_2$), while graphite is commonly utilized for the anode.

Due to the low affinity of lithium ions (Li^+) for the graphite matrix, these ones are liberated during discharge from the graphite matrix and migrate towards cobalt oxide. The migration of the Li^+ occur from the anode to the cathode through the electrolyte. Simultaneously, electrons migrate in the same direction through the external circuit. The oxidation half-reactions at both electrodes are as follows:

At the positive electrode (+): $LiCoO_2 \longrightarrow Li^+ + CoO_2 + e^-$

At the negative electrode (-): $LiC_6 \longrightarrow Li^+ + C_6 + e^-$

During the charging process, the reactions at the positive and negative electrodes and the resulting charge transports occur in the opposite direction. Electrons move from the positive electrode to the negative electrode through the external circuit, releasing Li^+ ions from cobalt oxide, which then traverse the electrolyte and eventually enter the graphitic phase.

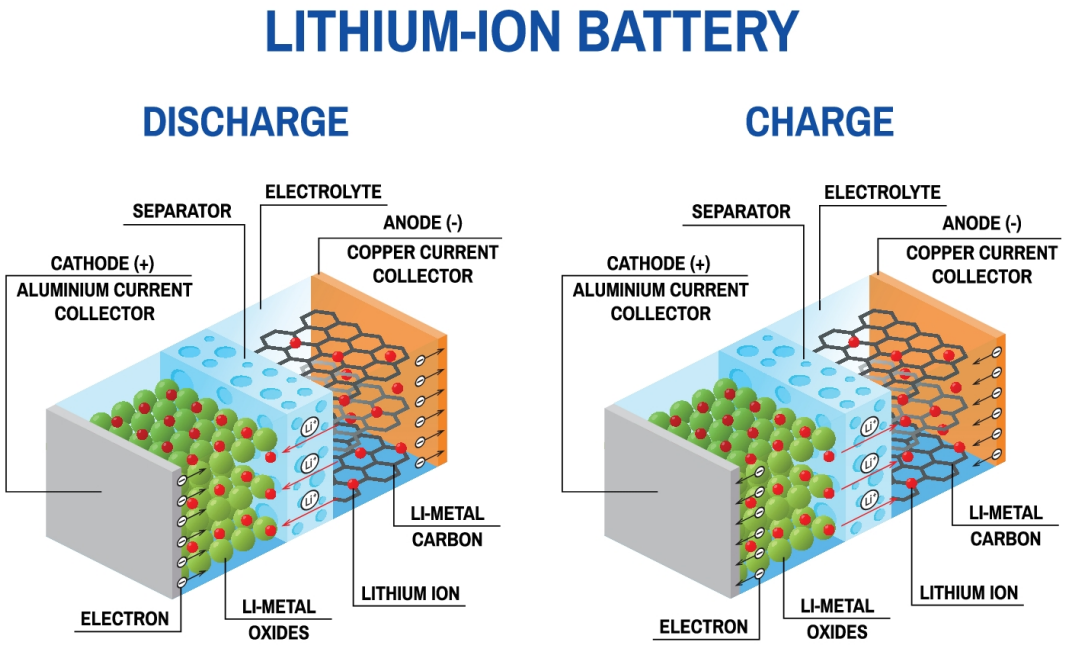

Figure 3.1: Schematic of a lithium battery.[101]

The electrolyte plays a crucial role in facilitating the transport of ions between the two electrodes. Commonly employed electrolytes for lithium-ion batteries are typically composed of nonaqueous organic solvents, such as ethylene carbonate, and/or a polymeric matrix like poly(ethylene oxide). The lithium ions (Li^+) are introduced through doping with a lithium salt, such as lithium bis(trifluoromethanesulfonyl)imide (LiTFSI) or lithium hexafluorophosphate ($LiPF_6$).

3.2 The glass transition

Most prior investigations of lithium-doped electrolytes have shown the presence of an optimal lithium concentration, typically around 1 mol/L, to achieve maximized ionic conductivity.[45] Below the optimum concentration, ionic conductivity rises proportionally to the increased

number of charge carriers provided by higher lithium salt concentrations. Conversely, beyond this optimum, a decline in ionic conductivity is evident, typically accompanied by an elevation in viscosity.[45]

At elevated lithium concentrations, strong Coulombic interactions emerge, leading to the formation of neutral ion pairs that do not contribute to ionic transport. In this regard, previous studies on polymer electrolytes have established a connection between the viscoelastic characteristics of the polymeric matrix and the overall ionic conductivity.[102, 103] A good indicator of these properties is the glass transition, where increased T_g values, indicative of decreased polymeric chain mobility, lead to a corresponding reduction in conductivity.

A similar behavior may be postulated for plastic electrolytes, wherein the reduction in rotational motion of the hosting plastic structure, as reflected in elevated T_g values, may result in a reduction of the ionic conductivity.

In the terms of timescale, T_g corresponds to dynamics on the order of 100 seconds.[104] This tends to occur at approximately 2/3 of T_m, where T_m is the crystalline state's melting point.[105] From an experimental perspective, T_g is achieved by subjecting the sample to sufficiently high cooling rates. This rapid cooling is employed to circumvent the crystalline state, a process commonly referred to as *quenching*.

In terms of viscosity, T_g can alternatively be defined by a viscosity value of 10^{12} Pa·s.[104] Subsequent to the glass transition, viscosity exhibits a pronounced temperature dependence, which can often be represented by the Vogel-Fulcher-Tammann (VFT) equation:[106–108]

$$\eta = \eta_\infty \cdot \exp\left(\frac{D_\eta T_\eta}{T - T_\eta}\right). \tag{3.1}$$

Analougouly, other parameters such as the conductivity, resistivity or the relaxation contant, can be described by a VFT law. The general expression for Eq. (3.1) takes on the form:

$$F = F_\infty \cdot \exp\left(\frac{D_F T_F}{T - T_F}\right), \tag{3.2}$$

where F represents various physical quantities such as σ_{DC}, ρ_{DC} or τ. Here, D_F denotes the strength parameter governing the temperature dependence of the observable F in a supercooled liquid according to the Arrhenius law, and T_F signifies the divergence temperature or the ideal glass transition temperature. At T_F, the quantity F of the system is expected to become extremely sensitive to changes in temperature.

Upon reaching the glass transition temperature T_g, the fragility parameter m, defining the slope of the T_g-scaled Arrhenius plot (Angell plot) for viscosity or relaxation time in a glass-forming liquid, is given by:[109, 110]

$$m = \left.\frac{d\log_{10}(k)}{d(T_g/T)}\right|_{T=T_g}, \tag{3.3}$$

where k represents either the viscosity η or the relaxation constant τ.

Figure 3.2 depicts the Angell plot illustrating α-relaxation times for various (supercooled) plastic crystals, as reported by Lansab *et al.*[111]. The dashed and dotted lines represent fragility values corresponding to $m = 16$ and $m = 170$, respectively. *Fragile plastic crystals* where weak van der Waals interactions takes place,[112] such as Freon and AGP, exhibit elevated m values. Conversely, *strong plastic crystals*, characterized by strong covalent directional bonds,[112] demonstrate low m. Noteworthy instances of strong liquids include C_{60} and PCT. The binary plastic crystal $SN_{0.6}GN_{0.4}$ investigated in this work, aligns with highly fragile liquids, while cyclohexanol and cyclooctanol can both be considered intermediate plastic crystals.

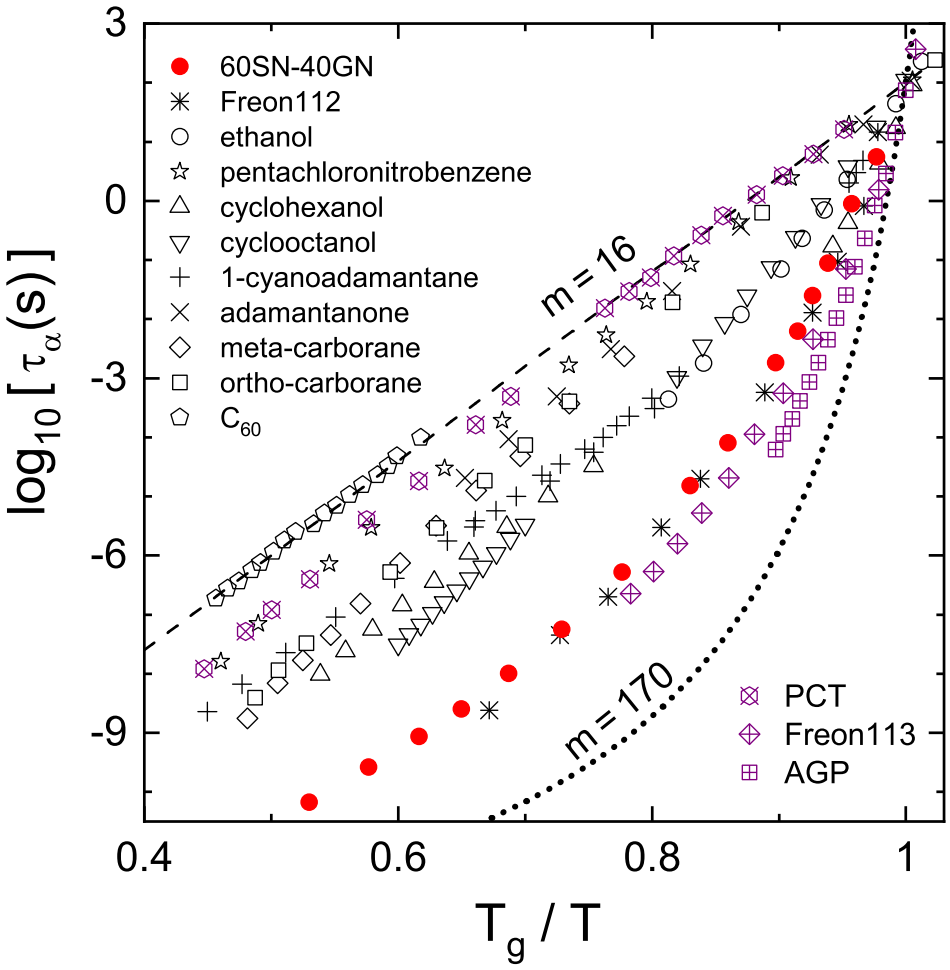

Figure 3.2: Angell plot of the α-relaxation times for a variety of (supercooled) plastic crystals as published in ref. [111]. The materials presented on the left have been previously documented in [31], which offers additional details and references. Data for Freon113 with Tg = 72 K,[113] 1,6-anhydro-β-D-glucopyranose (AGP) with Tg = 245 K,[114] and pentachloro-toluene (PCT) with Tg =162 K,[115] are also incorporated.

3.3 Ion diffusion

A simplified concept for elucidating ion transport in lithium doped plastic crystals involves treating the Li^+ as non-interacting particles diffusing within a non-rigid crystal matrix. A comparable approach has frequently been employed in the characterization of polymer electrolytes, wherein conductivity can be assumed as diffusion-dominated even in the presence of ion-ion interactions.[116] This assumption is particularly accurate when strong correlations exist between the hosting matrix and charge carrier,[116] as it could be expected for plastic electrolytes.

In this sense, plastic electrolytes exhibit electrical conductivity achieved by the mobility of ions within the plastic structure. The charge diffusion coefficient for non-interacting ions is defined by the Nernst-Einstein relation as following:[117]

$$D_\sigma = \frac{k_B T \sigma_{DC}}{N_{ions} q^2}, \tag{3.4}$$

σ_{DC} is the DC conductivity, k_B the Boltzmann constant, N_{ions} the number of ions and q the elementary charge. In terms of cation and anion contributions, Eq. (3.4) becomes:[117]

$$D_\sigma = D_{\sigma C} + D_{\sigma A} = \frac{k_B T \sigma_C}{N_C q^2} + \frac{k_B T \sigma_A}{N_A q'^2} \tag{3.5}$$

where σ_C and σ_A denote the partial conductivities of the cation and the anion, respectively.

D_σ has no Fickian meaning and is a rather a quantity which interprets σ_{DC} in terms of an effective equivalent diffusion coefficient.[117] In order to quantify the derivations from the ideal behavior, where every diffused ion contributes to a successful ionic conduction, one defines the Haven ratio H_R as the ratio of the tracer diffusion coefficient D^* and the charge diffusion coeffcient D_σ:[117]

$$H_R = \frac{D^*}{D_\sigma}. \tag{3.6}$$

Additionally, one can obtain the DC conductivity σ_{DC} from the plateau observed in the conductivty spectra $\sigma(\omega)$ acquired with dielectric spectroscopy (see Section 5.1).

For spherical particles with radius r diffusing through a liquid, the diffusion coefficient is also related to the viscosity η by the Stokes–Einstein equation as follows:[117]

$$D_\eta = \frac{k_B T}{6\pi\eta r}. \tag{3.7}$$

3.4 The paddle-wheel mechanism

3.4.1 The case of lithium sulfate – Li_2SO_4

The first model of correlated dynamics between charge carrier and matrix, was established in a study of the high temperature phase of lithium sulfate (α-Li_2SO_4) by Kvist and Bengtzelius [118]. The theory behind this discovery is particularly useful for understanding the ionic transport in plastic electrolytes. In fact, α-Li_2SO_4 happens to share some similarities with the organic rotator phases investigated in this work, for e.g., in terms of rheology.[119, 120]

By taking a closer look at the temperature dependent conductivity of lithium sulfate (Fig. 3.3), one observes a sudden increase for T > 580°C. This observation was reported by Benrath and Drekopf in 1921 [121] and was discussed almost forty years later by Førland and Krogh-Moe [122]. Indeed, the latter authors determined the crystal structure of α-Li_2SO_4 to fcc and suggested that a solid-solid phase transition, taking place around T = 575°C, is most likely responsible for the increase in the ionic conductivity.

In this fcc-structure (shown in Fig.3.4), the sulfate groups can rotate by 45° about one of the three fourfold axes and the lithium ions can exchange between the tetrahedral and octahedral lattice positions [122]. A strong translational coupling between the sulfate group and the Li ions was therefore implied. This finding was later on supported by results for the electrical conductivity, found to be on the same order of magnitude in the high temperature structure as in the fused state [123].

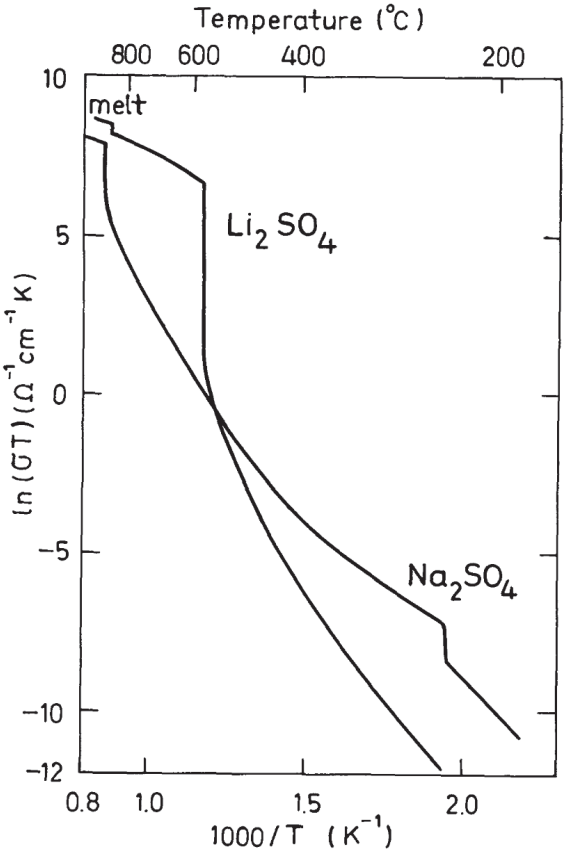

Figure 3.3: Conductivity of α-Li_2SO_4 as function of temperature reported in ref.[124]

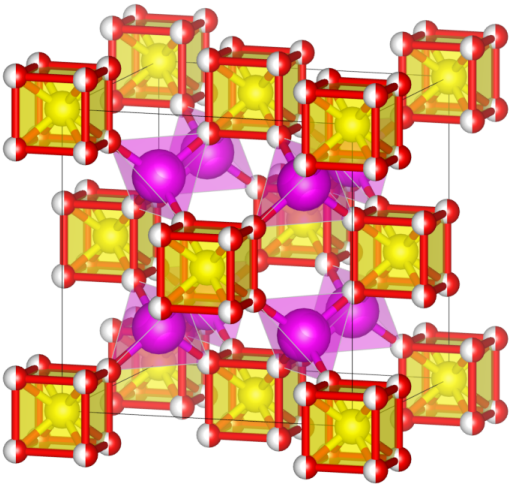

Figure 3.4: *fcc* structure of α-Li_2SO_4 made with VESTA using parameters from [125].

Further diffusion studies carried out by Lunden *et al.*[126] on α-Li_2SO_4 and similar high-temperature sulfate phases, revealed some interesting aspects regarding their ionic transport. Monovalent ions with high activation energies, such as Li^+ or Na^+, showed fast ionic diffusion while those with low activation energies, such as Rb^+ or Cs^+, showed lower diffusivites. Additionally, monovalent ions with low ionic radius were found to diffuse faster than those with higher radius.

Moreover, neutron diffraction studies on α-Li_2SO_4 showed that 90% of the Li-ions occupy the tetrahedral lattice positions (1/4, 1/4, 1/4) and none of them occupy the octahedral positions.[125, 127] In other terms, lithium hopping between these two lattice sites could not be detected and a new concept to describe the ionic transport in this material was needed.

Interestingly, the remaining 10% of the Li ions in α-Li_2SO_4 were found in the proximity of the sulfate ions.[127] In addition, molecular dynamics studies on various lithium sulfate compositions, revealed that the cations are bonded to one or two oxygen atoms of neighboring sulfate groups.[128] Moreover, similarities were found for the activation energies obtained from the reorientational motion of the sulfate groupe, from the Li ion diffusion as well as that obtained from the conductivity (see Table 3.1).[126]

Table 3.1: Activation energies obtained for α-Li_2SO_4 using conductivity data (σT), diffusion data of the Li ion (D^+) and the reorientation motion of SO_4^- based on Raman spectroscopy. The values were reported in ref.[126] with a comprehensive listing of all the sources from which they were collected.

E_A	eV
σT	0.43
D^+	0.34
Raman	0.40

Likewise, Mellander *et al.*[126] reported Li^+ jumpy frequencies that were calculated from the electrical conductivity of α-Li_2SO_4, and found these in the same order as those obtained from neutron diffraction or Raman scattering.

In the light of these obervations, Kvist and Bengtzelius proposed a transport model named "cog-wheel mechanism" to describe these dynamics correlations in cubic sulphates.[118] Subsequently, Lunden *et al.*[129] conducted further investigations on the same materials and described thoroughly what was later refered to as "paddle-wheel mechanism".

3.4.2 Prerequisites for a paddle-wheel mechanism

The paddle-wheel model proposed by Lunden *et al.*[129], implies several requirements on the local structure and the type of coupling between matrix and cation. These requirements are key for the definition of this mechanism and are necessary to establish a paddle-wheel like dynamics in a material.

First, the structure of the matrix needs to provide sufficient free volume to allow an unhindered reorientational motion of the rotating molecules or polyanions. In that sense, the rotator have to be of limited volume and simple symmetry with no long-range covalent interactions. Long chain molecules, for example, are more likely to have a restricted reorientational motion within a covalent network. Additionally, the ionic radius of the cation is a determining factor for its spatial distribution within the crystal structure of the matrix. Cations with large or too small ionic radii with respect to the hosting matrix, may fail in establishing the necessary spatial coupling between them and the rotating phase.

Another major prerequisite for the existence of the paddle-wheel mechanism is the energetical or rather temporal coupling between the cation translational motion and the reorientational motion of the matrix. Following this prerequisite, both motions have to be on the same time scale. In terms of energy barrier, the activation energy required for a Li ion to undergo a translation motion, must be of the same order of magnitude as the activation energy needed for the rotating polyanion or molecule to undergo a complete reorientational movement.

It is important to note that various models exist to describe the dynamic correlation between cations and matrix. Jansen [130] offers a useful classification of such mechanisms, among which the revolving door mechanism is included. This mechanism bears resemblance to the paddle-wheel model, with a notable distinction lying in the strong interaction between cations and anions. In this model, the mobile anions exhibit an evasive motion towards the passage of cations. While both models imply a similar temperature dependence of the characteristic time scales, in the case of revolving door mechanism, the values may not necessarily align. Additionally, the revolving door mechanism doesn't necessarily depend on having sufficient free volume; rather, it requires an ample number of molecules to rotate or "doors" to open for effective charge transport.

4 Nuclear Magnetic Resonance

4.1 Quantum description

In the presence of a static magnetic field, the energy levels of the nuclei are split into equidistant levels according to (2 I + 1) with $\Delta E = \hbar\omega_L$. This is known as the *Zeeman effect*. Assuming a non interacting spin in a uniform static magnetic field $\vec{B}$ along the z-axis, $\vec{B} = (0, 0, \vec{B_z^0})$, one obtains for the Zeeman Hamiltonian:[131]

$$\hat{H}_{ZE} = -\vec{M} \cdot \vec{B} = -\gamma\hbar\hat{I}_z B_z^0, \tag{4.1}$$

where $\vec{M}$ is the magnetic moment describing the bulk magnetization of the sample and $\hat{I} = (\hat{I}_x, \hat{I}_y, \hat{I}_z)$ is the nuclear spin operator.

Following a quantum mechanical approach, the orientation dependence of the nuclear energy is contained in the total spin hamiltonian as follows:

$$\hat{H}_{tot} = \hat{H}_{\mathrm{ZE}} + \hat{H}_{\mathrm{RF}} + \hat{H}_{\mathrm{int}}. \tag{4.2}$$

$\hat{H}_{\mathrm{RF}}$ describes the applied radiofrequency (RF) excitation. Assuming a $\vec{B_{\mathrm{RF}}}$ along the x-axis, $\hat{H}_{\mathrm{RF}}$ can be written in the rotating frame as:[132]

$$\hat{H}_{\mathrm{RF}} = -\gamma\hbar B_{RF}\hat{I}_x \cos(\omega_{RF} t). \tag{4.3}$$

$\hat{H}_{\mathrm{int}}$, on the other hand, contains the various interactions in the spin system and can be described as the sum of these interactions. Sections 4.1.1 to 4.1.3 delve into the interactions relevant for an NMR experiment and provide a detailed description of the $\hat{H}_{\mathrm{int}}$ hamiltonian.

4.1.1 Chemical shielding

The electrons surrounding the nucleus produce a secondary field that can effect the magnetic field. This phenomenon is known as the *chemical shielding*. The resulting frequency shift in the NMR spectrum due to this field superposition is referred to as *the chemical shift*. The adjustment of the Zeeman Hamiltonian in Eq. (4.1), accounting for the impact of chemical shielding, is expressed as follows:[132]

$$\hat{H}_{ZC} = -\gamma\hbar\hat{I}_z(1 - \sigma)B_z^0, \tag{4.4}$$

where σ is second-rank tensor.

The chemical shielding tensor can be decomposed to symmetric and antisymmetric component $\sigma = \sigma^s + \sigma^{as}$, where in NMR, usually only the symmetric component (σ^s) is relevant.[132] Furthermore, the coordinate system for defining the shielding tensor is often chosen so σ^s is diagonal. This system is refered to as *the principal axes frame* where the components of σ^s can be represented by a 3×3 matrix as follows:[132]

$$\sigma^s = \begin{bmatrix} \sigma_{xx}^{PAF} & 1/2(\sigma_{xy}^{PAF} + \sigma_{yx}^{PAF}) & 1/2(\sigma_{xz}^{PAF} + \sigma_{zx}^{PAF}) \\ 1/2(\sigma_{xy}^{PAF} + \sigma_{yx}^{PAF}) & \sigma_{yy}^{PAF} & 1/2(\sigma_{yz}^{PAF} + \sigma_{zy}^{PAF}) \\ 1/2(\sigma_{xz}^{PAF} + \sigma_{zx}^{PAF}) & 1/2(\sigma_{yz}^{PAF} + \sigma_{zy}^{PAF}) & \sigma_{zz}^{PAF} \end{bmatrix}. \tag{4.5}$$

Moreover, using the components of the matrix (4.5), one definies the isotropic value σ_{iso}, the *anisotropy* Δ and the *asymmetry* η_{CS} as:[132]

$$\sigma_{iso} = 1/3(\sigma_{xx}^{PAF} + \sigma_{yy}^{PAF} + \sigma_{zz}^{PAF}) \tag{4.6}$$

$$\Delta = \sigma_{zz}^{PAF} - \sigma_{iso} \tag{4.7}$$

$$\eta_{CS} = (\sigma_{xx}^{PAF} - \sigma_{yy}^{PAF})/\sigma_{zz}^{PAF}. \tag{4.8}$$

With the parameters mentioned above, the chemical shift frequency is defined as:[132]

$$\omega_{CS} = -\omega_L \sigma_{iso} - \frac{1}{2}\omega_L \Delta \left(3\cos^2(\theta) - 1 + \eta_{CS}\sin^2(\theta)\cos(2\phi)\right). \tag{4.9}$$

The angles θ and ϕ refer to the spherical coordinates; θ represents the polar angle between the z-axis and the principal axes frame of the chemical shift and ϕ is the azimuthal angle.

4.1.2 Dipole-dipole interaction

The nuclear magnetic moments associated with each spin $\vec{\mu}$ undergo an interaction known as dipole-dipole interaction, wherein they interact through space with other spins. In solutions, the effects of the dipole-dipole interaction are usually mitigated by averaging them as a result of the molecular tumbling. However, in solids, this interaction remains prominent and becomes a significant contributor to line broadening.

In the case of dipolar coupling, one differentiates between homonuclear and heteronuclear dipolar couplings. The respective Hamiltonians are given by:[132]

$$\hat{H}_D^{II} = -\hbar\frac{\mu_0}{4\pi r_{ik}^3}\gamma_I^2(3\cos 2\theta - 1)\left(3\hat{I}_z\hat{I}_z - \hat{I}\cdot\hat{I}\right), \tag{4.10}$$

and

$$\hat{H}_D^{IS} = -\hbar\frac{\mu_0}{4\pi r_{ik}^3}\gamma_I\gamma_S(3\cos 2\theta - 1)\left(\hat{I}_z\cdot\hat{S}_z\right), \tag{4.11}$$

r_{ik} is the internuclear distance and the angle θ represents here the polar angle between the z-axis and the line connecting the nucleus of interest. Additionally, d_{ik} is the dipolar-coupling constant and is given by:[132]

$$d_{ik} = \hbar \left(\frac{\mu_0}{4\pi} \right) \frac{1}{r_{ik}^3} \gamma_I \gamma_S. \tag{4.12}$$

In the case of homonuclear dipolar coupling, where the interacting nuclei have the same spin quantum number, S can be equal to I in the equation above. Similarly to the chemical shielding, one can also express the dipolar interaction between two spins I and S with a hamiltonian in tensorial form:[132]

$$\hat{H}_D = -2\hat{I} \cdot D \cdot \hat{S}. \tag{4.13}$$

D is the dipolar coupling tensor described by three principal values of $-d/2$, $-d/2$ and $+d$.

4.1.3 Quadrupolar interaction

In addition to a dipolar moment, nuclei with a spin number I ≥ 1 possess a quadrupolar moment Q. This latter one can interact with electric field gradients at the nuclear site and affect the nuclear spin energy levels. The quadrupolar Hamiltonian is given by:[132]

$$\hat{H}_Q = \frac{eQ}{6I(2I-1)\hbar} \hat{I} \cdot V \cdot \hat{I} \tag{4.14}$$

where e is the elementary charge and V the electric field gradient (EFG) tensor. It's important to note that the EFG tensor is traceless, implying it lacks an isotropic component.[132]

By utilizing the PAF, wherein the EFG tensor becomes diagonal, one can define the *quadrupole coupling constant* χ and the *asymmetry paraemter* η_Q as:[132]

$$\chi = 2\pi \cdot C_Q = 2\pi \cdot \frac{e^2 q_{zz}^{PAF} Q}{h}, \tag{4.15}$$

and

$$\eta_Q = \frac{q_{xx}^{PAF} - q_{yy}^{PAF}}{q_{zz}^{PAF}}. \tag{4.16}$$

In the PAF, the quadrupole Hamiltonian in Eq. (4.14) becomes:[132]

$$\hat{H}_Q = \frac{e^2 q_{zz}^{PAF} Q}{4I(2I-1)\hbar} \left[3\hat{I}_{z^{PAF}}^2 - \hat{I}^2 + \eta \left(\hat{I}_{x^{PAF}}^2 - \hat{I}_{y^{PAF}}^2 \right) \right]. \tag{4.17}$$

The quadrupolar interaction leads to a shift of the energy levels according to the *quadrupolar frequency* given by:[132]

$$\omega_Q = \frac{3\pi C_Q}{4I(2I-1)} \left(3\cos^2(\theta) - 1 + \eta_Q \sin^2(\theta) \cos(2\phi) \right). \tag{4.18}$$

4.2 Semiclassical approach – Bloch equations

The semiclassical approach for interpreting NMR experiments involves utilizing the so-called *vector model*.[133] While it may not fully capture all aspects of the NMR experiment, the vector model offers the advantage of simplifying the interpretation process, making it more accessible and easier to understand.

In this approach, the magnetic moment $\vec{M}$ describing the bulk magnetization of a sample, is defined as the sum of the magnetic moments originating from each constituent nucleus that carries a spin:

$$\vec{M} = \sum_i \vec{\mu}_i. \tag{4.19}$$

Since the nuclear magnetic moment is related to the nuclear spin by $\vec{\mu} = \gamma\vec{I}$, where γ denotes the gyromagnetic ratio, only elements from the periodic table with isotopes possessing a non-zero spin number ($I \neq 0$) exhibit a nuclear magnetic moment and are considered NMR active.

During the NMR experiment, the sample is placed in a uniform magnetic field usually oriented along the z-axis. The magnetic moment will then experience a torque $\vec{N}$ that can be expressed as:[131]

$$\frac{d}{dt}\sum_i \vec{I}_i = \frac{1}{\gamma}\frac{d\vec{M}}{dt}. \tag{4.20}$$

The torque $\vec{N}$ and the magnetization vector $\vec{M}$ are related by: $\vec{N} = \vec{M} \times \vec{B}$. Thus, the expression in Eq. (4.2) leads to:[131]

$$\frac{dM_x(t)}{dt} = M_y(t)\gamma B_z^0, \tag{4.21}$$

$$\frac{dM_y(t)}{dt} = -M_x(t)\gamma B_z^0, \tag{4.22}$$

$$\frac{dM_z(t)}{dt} = 0. \tag{4.23}$$

Considering a Larmor precession about the $\vec{B}$ axis with a Larmor frequency $\omega_L = \gamma B_z^0$, the solutions of the aforementioned equations augmented by the relaxation times T_1 and T_2, give the Bloch equations as follows:[131]

$$\vec{M}(t) = \begin{bmatrix} M_x(t) \\ M_y(t) \\ M_z(t) \end{bmatrix} := \begin{bmatrix} (M_x^0 \cos\omega_0 t - M_y^0 \sin\omega_0 t)e^{-t/T_2} \\ (M_y^0 \cos\omega_0 t + M_x^0 \sin\omega_0 t)e^{-t/T_2} \\ M_z^0 + (1 - e^{-t/T_1})(M_z^\infty - M_z^0) \end{bmatrix}. \tag{4.24}$$

A useful concept of an NMR experiment involves manipulating the vector $\vec{M}$ away from its equilibrium state and observing its return to this state. This manipulation is accomplished by applying a RF pulse, which typically has the same frequency as the Larmor precession of the nuclei.

In a rotating coordinate system that matches the frequency of the Larmor precession, the magnetization vector $\vec{M}$ resulting from the precession appears static. The effective magnetic field in this rotating frame is expressed as:[133]

$$\Delta B = -\frac{\omega_L - \omega_{\text{rot. frame}}}{\gamma}. \tag{4.25}$$

Similarly, the application of a resonant RF pulse ($\omega_{RF} = \omega_L$) generates a seemingly static magnetic field $\vec{B_{\text{RF}}}$ of sufficient strength to perturb $\vec{M}$ from its equilibrium state. The RF pulse is usually applied for a time delay sufficiently long enough to flip the magnetization about a 90° angle, for instance. This duration is commonly refered to as t_{90°.

4.3 Spin relaxation

After the spins are perturbed from their equilibrium state by applying an RF pulse, they tend to revert to their equilibrium state. This phenomenon is commonly referred to as spin relaxation. The concept of relaxation in NMR is intricate, necessitating the incorporation of various theories that lie beyond the scope of this work. However, a simplified explanation can be derived using the vector model outlined in Section 4.2.

In NMR, distinction is made between longitudinal relaxation and transversal relaxation. Longitudinal relaxation, also known as spin-lattice relaxation, elucidates the return to equilibrium along the external magnetic field $\vec{B}$ and is characterized by the time constant T_1. Following the application of an RF pulse for t_{90°, the magnetization vector undergoes a 90° flip. Subsequently, the magnetization vector initiates an exponential growth back to its equilibrium value. The time constant T_1 represents the time required for the z-magnetization to attain $(1 - 1/e) \approx 63.2\%$ of its final steady-state value.

On the other hand, transverse relaxation, or spin-spin relaxation, delineates the dephasing of transverse magnetization and is characterized by the time constant T_2. Upon the application of a 90° pulse and concurrent with longitudinal relaxation, dephasing of transverse relaxation (magnetization in the xy-plane) occurs. The xy-magnetization undergoes a characteristic exponential decay, and T_2 is the time at which only $(1/e) \approx 36.8\%$ of the xy-magnetization persists.

4.3.1 Spectral densities

Molecular motion directly influences the direction and magnitude of the time-varying local fields arising from the interactions discussed in Section 4.1 [133].

In NMR, the fluctuations related to the molecular motion can be described by correlation functions. The simplest form of a correlation function is an exponential decay, characterized by a time constant τ_c, known as the correlation time:[133]

$$G(t) = G(0) \cdot \exp\left(-\frac{t}{\tau_c}\right). \tag{4.26}$$

For $t < \tau_c$, $G(t)$ remains close to its initial value, indicating that the correlation between the spins remains significant; that is, the system retains memory of its initial state. As time surpasses τ_c, $G(t)$ approaches zero, signifying that the system reaches a state of equilibrium where the correlations between spins are lost and the spins are said to be uncorrelated. The parameter τ_c provides valuable information about the system, as it directly depends on molecular size, shape and viscosity.

The Fourier transform of the correlation function yields the *spectral density*. In NMR, the Fourier transform of Eq.(4.26) is known as the Bloembergen-Purcell-Pound (BPP) spectral density:[133]

$$J_{BPP}(\omega, \tau_c) = \frac{2\tau_c}{1 + (\omega\tau_c)^2}. \tag{4.27}$$

The Havriliak-Negami (HN) form is another example of a spectral density and is given by:[134]

$$J_{HN}(\omega, \tau_c, \gamma, \alpha) = \frac{2}{\omega} \sin\left[\gamma \arctan\left\{\frac{(\omega\tau_c)^\alpha \sin(\alpha\pi/2)}{1 + (\omega\tau_c)^\alpha \cos(\alpha\pi/2)}\right\}\right] \times \left[1 + 2(\omega\tau_c)^\alpha \cos(\alpha\pi/2) + (\omega\tau_c)^{2\alpha}\right]^{-\gamma/2}, \tag{4.28}$$

where α is the Cole-Cole exponent and γ the Cole-Davidson exponent, with α and $\gamma \in (0, 1]$. If $\alpha = 1$ or $\gamma = 1$, Eq. (4.28) describes the Cole-Davidson (CD) or the Cole-Cole (CC) spectral density, respectively:[134]

$$J_{CD}(\omega, \tau_c, \gamma) = \frac{2}{\omega}\left\{\frac{sin\left[\gamma \arctan(\omega\tau_c)\right]}{(1 + \omega^2\tau_c^2)^{\epsilon/2}}\right\}, \tag{4.29}$$

and

$$J_{CC}(\omega, \tau_c, \alpha) = \frac{2}{\omega} \sin\left(\frac{\alpha\pi}{2}\right)\left[\frac{(\omega\tau_c)^\alpha}{1 + (\omega\tau_c)^{2\alpha} + \{2\cos(\alpha\pi/2)\}(\omega\tau_c)^\alpha}\right], \tag{4.30}$$

4.3.2 General expressions for the relaxation rates

The contributions to longitudinal relaxation resulting from various interactions, as detailed in Section 4.1, can be computed utilizing one of the spectral density functions mentioned above. For convenience, the longitudinal relaxation rate ($1/T_1$) arising from the quadrupolar interaction of a nuclei with a spin number I is reported in this work:[135]

$$\frac{1}{T_1} = \frac{3}{200}(\chi)^2(1+\eta_Q^2/3)\frac{2I+3}{I^2(2I-1)}\left[J(\omega_L)+4J(2\omega_L)\right]. \tag{4.31}$$

Similary, the contribution of the quadrupolar interaction to the transverse relaxation ($1/T_2$) is given by:[135]

$$\frac{1}{T_2} = \frac{3}{400}(\chi)^2(1+\eta_Q^2/3)\frac{2I+3}{I^2(2I-1)}\left[3J(\omega_Q)+5J(\omega_L)+2J(2\omega_L)\right]. \tag{4.32}$$

4.3.3 Deuterium NMR

Hydrogen is inherent in organic materials and manifests in three isotopes: ^{1}Hydrogen (I = 1/2), ^{2}Deuterium (I = 1), and ^{3}Tritium (I = 1/2). While all three isotopes can be studied through NMR spectroscopy, deuterium and tritium exhibit low natural abundance, approximately $\sim 10^{-4}$ and $\sim 10^{-18}$, respectively.

Although opting for proton NMR (^{1}H) seems instinctive for material investigation due to its high natural abundance, it can be, however, quite challenging. Indeed, the primary challenge with ^{1}H NMR arises from strong dipole-dipole interactions among proton spins. In solid-state NMR, proton spectra are characterized by multiple lines, stemming from interactions between each spin and its neighboring spins. This interaction results in broad lines in the NMR spectrum.

One strategy to address this issue is isotope enrichment (separation), involving an increase in the concentration of a specific isotope. Given tritium's radioactivity, deuterium is the preferred choice in a process commonly referred to as *Deuteration*. In this method, Hydrogen atoms within a molecule are either entirely or partially replaced by deuterium.

The dominant interaction in deuterium NMR is usually the quadrupolar interaction. Based on Eq. (4.31) and Eq. (4.32), where $I = 1$ and $\eta_Q = 0$, the spin-lattice (T_1) and spin-spin (T_2) relaxation times for deuterium are given by:

$$\frac{1}{T_{1D}} = \frac{3}{40}(\chi_D)^2\left[J(\omega_L)+4J(2\omega_L)\right], \tag{4.33}$$

and

$$\frac{1}{T_{2D}} = \frac{3}{80}(\chi_D)^2\left[3J(\omega_Q)+5J(\omega_L)+2J(2\omega_L)\right]. \tag{4.34}$$

The quadrupole coupling constant for deuterium ($\delta_D = 3/4 \cdot \chi_D$) is typically around $2\pi \cdot 125$ kHz.[136]

4.3.4 Lithium NMR

Lithium NMR investigations can be conducted using two stable isotopes: ^{6}Lithium (I = 1) and ^{7}Lithium (I = 3/2). With a natural abundance of only 4.85%, ^{6}Lithium is often less suitable than ^{7}Lithium, which has a natural abundance of 95%. Indeed, despite ^{7}Lithium's higher quadrupolar moment leading to broader NMR lines, it is the preferred isotope, especially in scenarios where lithium is present in low percentages, as commonly observed in lithium electrolytes.

Similarly to deuterium, in solid-state ^{7}Li NMR the predominant interaction is the quadrupolar coupling. The spin-lattice (T_1) and spin-spin (T_2) relaxation times are given by:

$$\frac{1}{T_{1Li}} = \frac{1}{50}(\chi_{Li})^2 \left[J(\omega_L) + 4J(2\omega_L)\right], \tag{4.35}$$

and,

$$\frac{1}{T_{2Li}} = \frac{1}{100}(\chi_{Li})^2 \left[3J(\omega_Q) + 5J(\omega_L) + 2J(2\omega_L)\right]. \tag{4.36}$$

The ^{7}Li quadrupole coupling constant ($\delta_{Li} = 1/2 \cdot \chi_{Li}$) typically ranges between 40 and 110 kHz.[137]

4.4 NMR techniques employed in this work

In NMR the resonance frequency of the charge carrier is intricately linked to its surrounding environment. This fundamental principle serves as the foundation for investigating conducting materials using NMR spectroscopy. Indeed, the motion of the charge carrier, responsible for the conductivity process, results in variations in its surrounding environment. Similarly, the reorientational motion of the hosting matrix leads to a change in the resonant frequency as well. Monitoring these changes directly allows for valuable insights into the conductivity mechanism. In this context, NMR provides a range of experiments, from basic spectroscopy to sophisticated two-dimensional correlation experiments.

4.4.1 Spectroscopy

The most basic NMR experiment involves the application of a 90° pulse, aligning the magnetization vector $\vec{M}$ in the xy-plane. As the non-equilibrium magnetization undergoes precession about the external magnetic field, it induces an oscillating voltage in the detection coil surrounding the sample. The resulting signal is termed a *Free Induction Decay (FID)*, and its Fourier Transform yields the frequency domain NMR spectrum.

An alternative to the simple FID experiment is based on the Hahn Echo (HE), where the pulse sequence (illustrated in Figure 4.1) begins with a 90°_{x} pulse, bringing the magnetization

vector into the xy-plane. This is followed by a time delay t, during which the spins start to dephase and precess at different rates, e. g., due to local magnetic field inhomogeneities. Subsequently, the spins are refocused using a $180^{\circ}_{\pm x}$ pulse, and an echo maximum is detected after a second t delay. The HE experiment is well-suited for refocusing interactions linear in I_z, such as the chemical shift, heteronuclear dipole-dipole interaction, and inhomogeneities in the external magnetic field.[138]

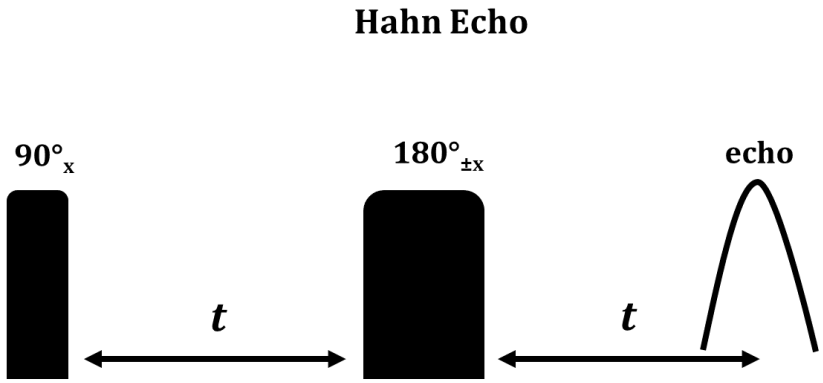

Figure 4.1: Hahn echo pulse sequence.

Additionally, the Solid Echo (HE) experiment, depicted in Figure 4.2, is another fundamental NMR sequence similar to the HE experiment. It begins with a 90°_{x} pulse and a delay t, but instead of a $180^{\circ}_{\pm x}$ refocusing pulse, a second $90^{\circ}_{\pm y}$ pulse is applied. The SE is useful for refocusing interactions bilinear in homonuclear spin operators, including the secular part of the dipole interaction and the quadratic spin part of the first order quadrupole interaction.[138]

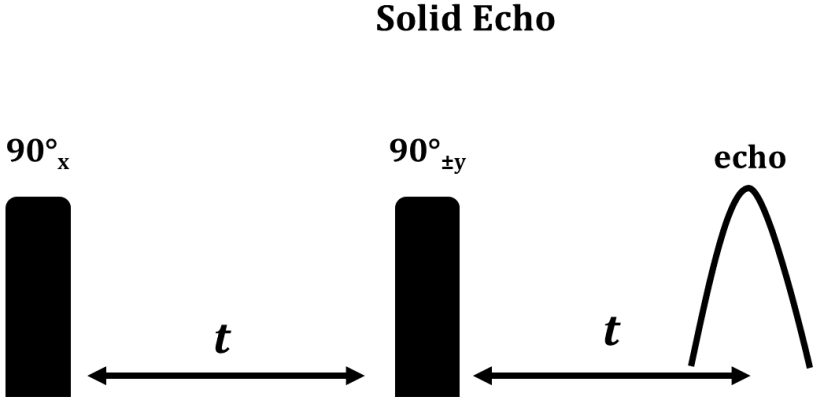

Figure 4.2: Solid echo pulse sequence.

4.4.2 Relaxometry

Longitudinal relaxation

To determine the longitudinal relaxation constant T_1, one can employ either Inversion Recovery (IR) or Saturation Recovery (SR) experiments, as illustrated in Figures 4.3 and 4.4, respectively. The IR experiment startes with a 180°_x pulse that flips the magnetization vector, followed by a delay t during which the spins undergo relaxation. After this delay, a fraction of the magnetization returns to equilibrium and is detectable through a refocusing sequence, which can either be a simple 90°_x pulse for detection, a HE or a SE sequence. The experiment is iterated by incrementing the t duration until full recovery is achieved.

The echo maxima acquired after each iteration can be fitted as a function of the duration t to determine the T_1 relaxation constant. In the present work, this fitting process involves utilizing a stretched exponential, as outlined below:

$$M(t) = (M_1 - M_{eq}) \cdot \exp\left(-\left(\frac{t}{T_1}\right)^{\beta}\right) + M_{eq}, \tag{4.37}$$

where M_1 is the start magnetization and M_{eq} the magnetization at equilibirum. The exponent β reflects a possible distribution of spin relaxation times. For a homogenous relaxation, the magnetization decay is monoexponential and $\beta = 1$. However, in cases where the relaxation processes are not homogeneous or involve multiple relaxation mechanisms, β can deviate from 1. An example of such deviation is observed in ^{7}Li, where satellite transitions ($\pm 1/2 \longleftrightarrow \pm 3/2$) and central transitions ($\pm 1/2 \longleftrightarrow \pm 1/2$) result in bi-exponential spin-lattice relaxation.

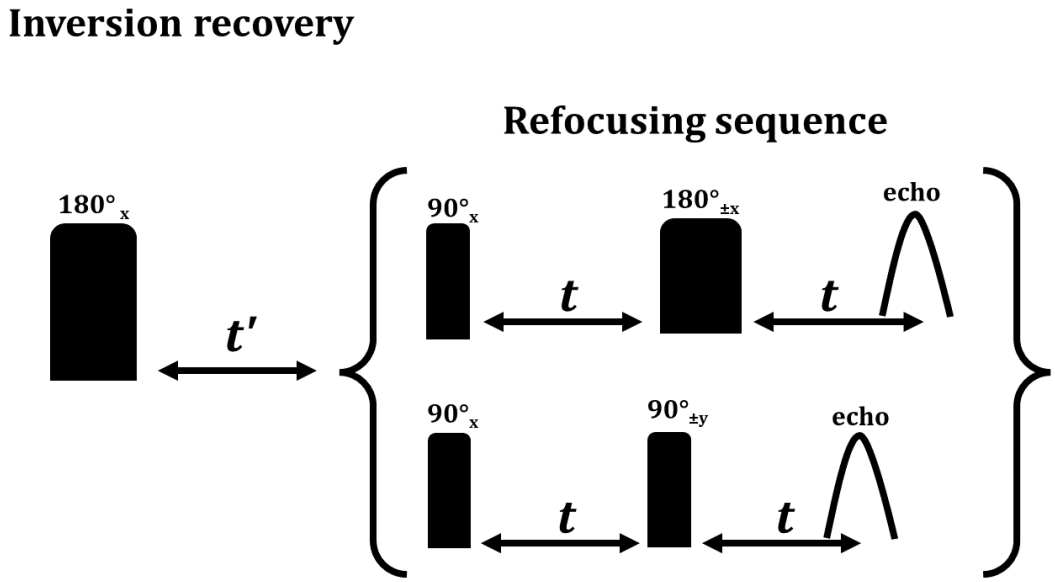

Figure 4.3: Inversion recovery pulse sequence. The refocusing sequence can either be a HE or a SE.

The IR experiment necessitates starting from an equilibrium state, meaning that a sufficient time interval, typically $5\times T_1$, must elapse between each iteration where t is increased. In NMR this interval is commonly referred to as the *recycle delay*. For substances with very slow longitudinal relaxation, the duration of the IR experiment can become quite prolonged. Furthermore, the IR experiment demands a precise inversion of the magnetization vector, requiring accurate calibration of the RF pulse duration t_{90°.

These experimental considerations when utilizing the IR experiment sometimes make the SR experiment more suitable. This latter one commences with a saturation sequence comprising n 90°_x pulses. This sequence nullifies all magnetization along the z-axis, ensuring that the starting conditions are at a well-defined non-equilibrium without the need for a perfectly calibrated 90° pulse or consideration of the recycle delay. The SR experiment requires the fulfillment of the condition $T_2 \ll t \ll T_1$, which is not the case at all temperatures.

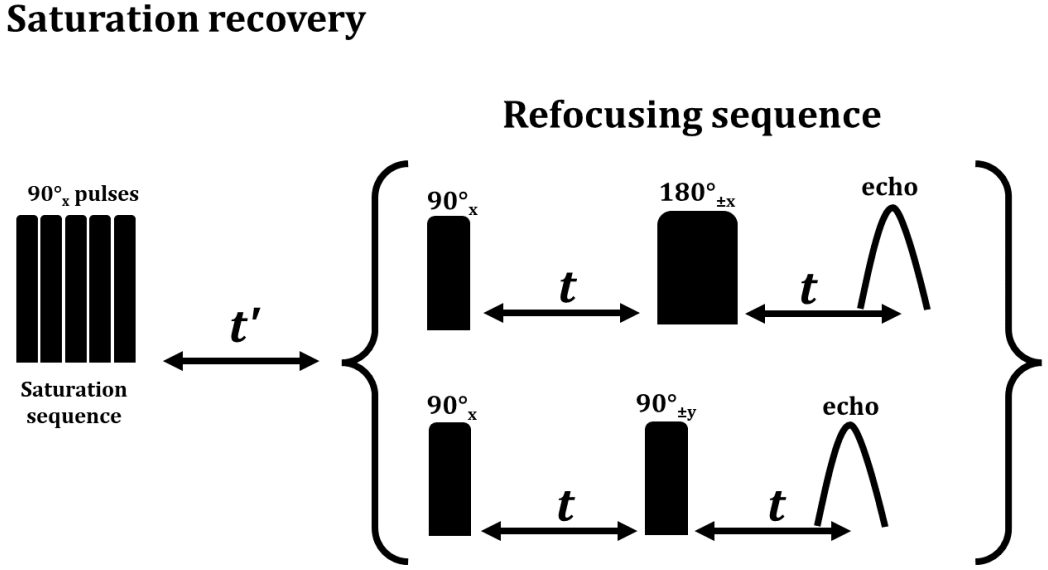

Figure 4.4: Saturation recovery pulse sequence. The refocusing sequence can either be a HE or a SE. In this work five 90° pulses with a seperation of 1 *ms* were used for saturation.

Transverse relaxation

To measure the transverse relaxation constant, one can employ either HE or SE experiments as outlined in Section 4.4.1. Since each experiment refocuses distinct interactions, the resulting transverse relaxation constant may vary. Similarly to the IR experiment, the sequence is repeated for a specified number of times, with each iteration increasing the duration t between the 90° and 180° pulses. Furthermore, the echo maxima obtained after each iteration can be analyzed by fitting them as a function of the duration t to ascertain the

T_2 relaxation constant, as follows:

$$M(t) = (M_1 - M_{eq}) \cdot \exp\left(-\left(\frac{t}{T_2}\right)^{\beta}\right) + M_{eq}. \tag{4.38}$$

If the substance under investigation displays rapid diffusion behavior, common in the liquid state, field inhomogeneity introduces a factor affecting spin-spin relaxation. In this context, T_2^* represents the transverse relaxation constant, accounting for the impact of field inhomogeneity. The Carr-Purcell-Meiboom-Gill (CPMG) pulse sequence, illustrated in Figure 4.5, serves to counteract the effects of field inhomogeneity.

The CPMG experiment is conducted in a single iteration, initiating with a 90°_x pulse followed by a relaxation delay t. Subsequently, a 180°_y pulse is applied for refocusing, and an echo maximum is recorded after a second t duration. The spin then undergoes dephasing for a third t duration. This refocusing sequence is repeated to generate n echoes with consistent spacing t until the entire decay describing the spin-spin relaxation is systematically scanned.

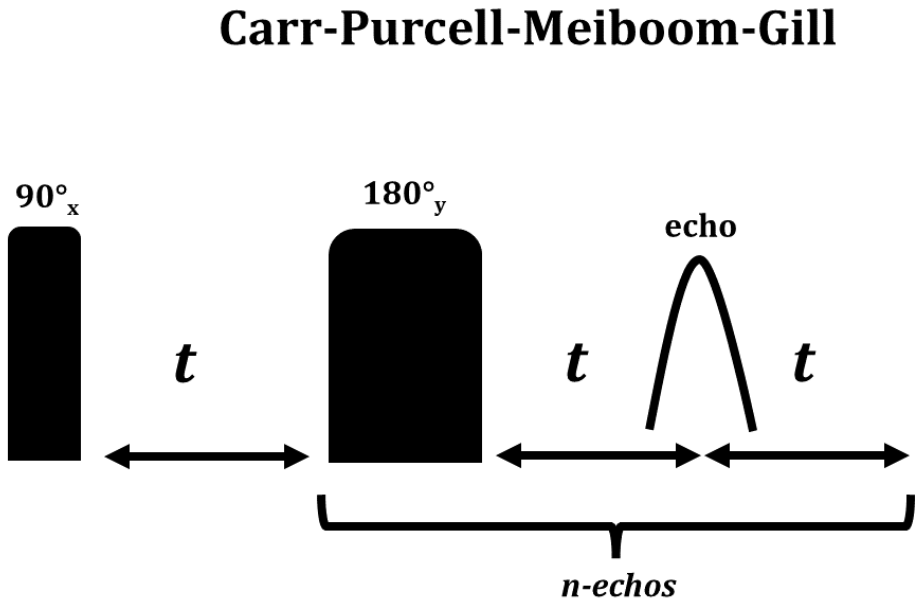

Figure 4.5: Carr-Purcell-Meiboom-Gill (CPMG) pulse sequence. The refocusing sequence is repeated for n number of times.

4.4.3 Stimulated echo

The Stimulated Echo (STE) pulse sequence, depicted in Figure 4.6, is employed to investigate processes of considerably slower nature. Pictorially speaking, this sequence utilizes a HE pulse sequence but introduces a separation between the dephasing interval and the rephasing

interval. This separation is achieved by dividing the second pulse into two distinct parts. The resulting three-pulse sequence is commonly employed in two-dimensional exchange spectroscopy.

Upon application of the first 90° pulse, the magnetization vector initiates procession in the xy plane. The subsequent time delay, referred to as the evolution time t_p, allows the spins to commence dephasing before a 90° storing pulse is applied. Depending on the phase of this pulse, either the cosine or the sine component of the precessing magnetization is aligned along the z-axis, while the other component will dephase during a sufficiently long mixing time t_{mix}. Subsequently, the stored magnetization is recalled, and akin to the Hahn echo, not all components come into phase simultaneously. Consequently, the STE exhibits lower amplitude and broader temporal dispersion.

The stored magnetization along the z-axis decays in accordance with the T_1 relaxation constant during the mixing time. Meanwhile, magnetization dephasing in the xy plane during the evolution time follows the T_2 relaxation constant. The acquired echo maxima can be fitted by the following equation:

$$F_2(t_{mix}) = M_{eq} \cdot \left((1 - Z) \cdot \exp\left(-\left(\frac{t_{mix}}{\tau_c} \right)^{\beta_c} \right) + Z \right) \cdot \exp\left(-\left(\frac{t_{mix}}{T_1} \right)^{\beta_1} \right) + M_1. \tag{4.39}$$

The Z parameter reflects the final state correlation and τ_c the correlation time.

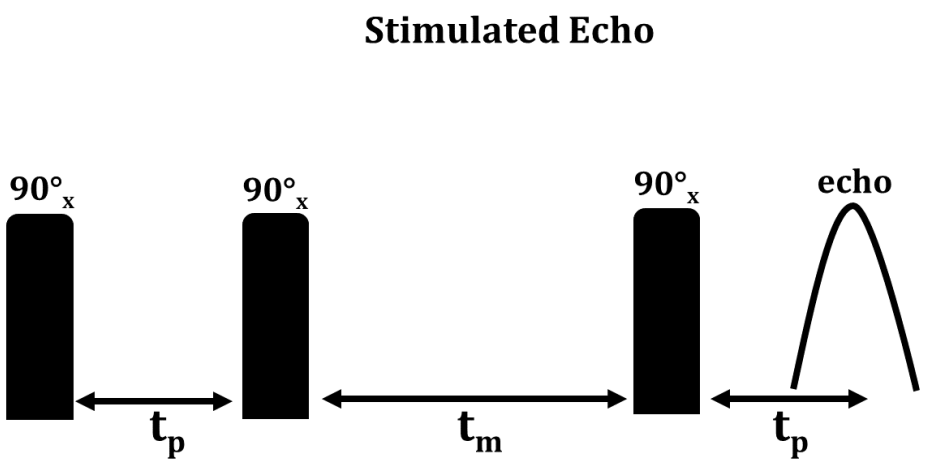

Figure 4.6: Stimulated echo pulse sequence.

4.4.4 Diffusometry

Diffusion NMR typically employs magnetic field gradients to encode spatial information. These gradients induce gradual variations, typically linear, in the static magnetic field ($\vec{B}$).

Consequently, the resonance frequency is altered according to the equation: $\omega_L(z(t)) = \omega_L + \gamma g z(t)$. In the volume of interest, the gradient strength g can be constant in time such that static field gradient (SFG) is achieved, or variable, utilizing pulse field gradient (PFG). In both experimental setups, gradient calibration is necessary. Detailed experimental information for both experiments is provided in Section 6.3.

Pulsed field gradient (PFG) NMR experiment

The most straightforward PFG experiment involves employing the HE pulse sequence and incorporates two pulse gradients during the separation t, where each gradient pulse is applied for a duration of δ. The time interval between the two gradient pulses is referred to as Δ. The initial field gradient serves as the dispersion pulse, while the second one functions as the refocusing pulse. Successful refocusing occurs only for nuclei that have not experienced significant movement along the gradient axis. Indeed, due to diffusion, certain nuclei displace from their original positions, hindering their signals from being effectively refocused and consequently diminishing the intensity of the resulting signal.

The PFG pule sequence is repeated several times by incrementing the strength of the gradient g. The self-diffusion coefficient D can by dermined by fitting the intensity I of the measured signal using the Stejskal-Tanner equation,[139] as follows:

$$\frac{I(t)}{I_0} = \exp\left(-D\gamma^2 g^2 \delta^2 (\Delta - \delta/3)\right). \tag{4.40}$$

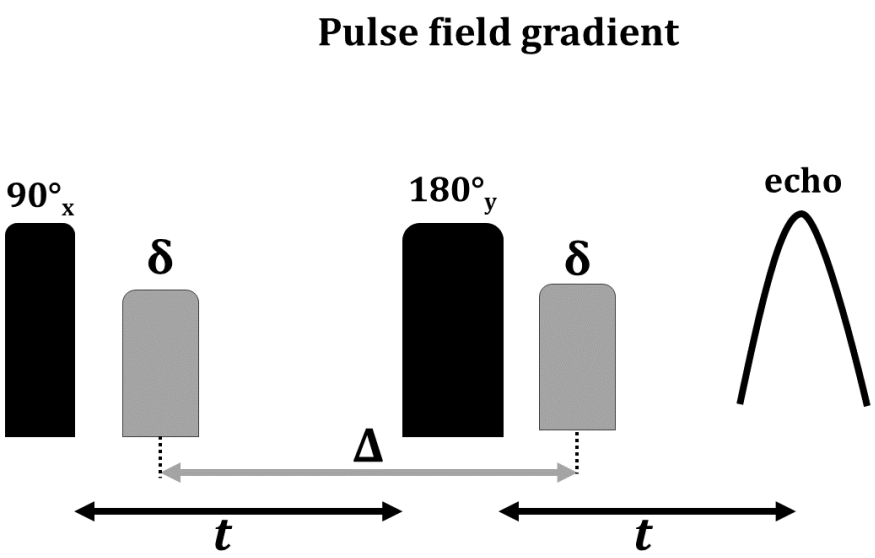

Figure 4.7: Pulse field gradient (PFG) sequence.

Static field gradient (SFG) NMR experiment

To enhance the detection of diffusion processes without altering the gradient strength, a static field gradient can be employed. This experimental approach involves utilizing a STE pulse sequence, as detailed in Section 4.4.3. In this experiment, the mixing time t_{mix} is systematically varied for several evolution times t_p, causing the nuclei to experience the static magnetic field for varying durations. The magnetization can be fitted using the following equation:[140]

$$M(t_{mix}, t_p) = M_{eq} \cdot exp\left(-q^2(t_{mix} + 2/3t_p)D\right) \cdot exp\left(-\frac{2t_p}{T_2}\right) \cdot \exp\left(-\frac{t_{mix}}{T_1}\right), \tag{4.41}$$

where $q = \gamma g t_p$ and can be understood as the modulus of an effective scattering vector.[141, 142]

When the evolution time t_p is significantly smaller than the mixing time t_{mix}, during which the transverse magnetization decays due to diffusion, the term $(2/3)t_p$ in Eq. (4.41) can be disregarded. The correlation time τ_c obtained for each experiment at constant t_p, is related to the diffusion coefficient according to:

$$\tau_c = \frac{1}{Dq^2} = \frac{1}{D} \cdot q^{-2}. \tag{4.42}$$

Finally, to determine the diffusion coefficient D, the correlation times obtained from each experiment is plotted against q^{-2}. The slope of the linear-curve, which should describe the experimental data points, is the inverse of the diffusion coefficient, as outlined in Eq. (4.42).

5 Relaxation spectroscopies

5.1 Dielectric spectroscopy

5.1.1 Polarization response

A dielectric medium can serve as an electrical insulator capable of polarization in response to an applied electric field. In contrast to electrical conductors, where electric charges can move freely, insulating dielectric materials lack loosely bound or free electrons or ions that can drift. When exposed to an electric field, the electric charges within the dielectric material experience minimal shifts from their average equilibrium positions, leading to dielectric polarization.

The Universal Dielectric Response offers insights into the behavior of dielectric mediums under alternating current (AC), elucidating how dielectric properties scale with frequency. Building upon the work of *Maxwell and Boltzmann*, the induced charge $\vec{Q_{in}}$ of a capacitor filled with a dielectric medium increases due to its polarization P, as described by the equation:[143]

$$\vec{Q} = \vec{Q_{in}} + \vec{P} = \epsilon_0(1 + \chi)\vec{E} = \epsilon\vec{E}, \tag{5.1}$$

where $\vec{E}$ is the electric field, ϵ_0 is the dielectric permittivity of vacuum, and ϵ and χ are the dielectric permittivity and susceptibility of the dielectric medium. The response of polarization to an arbitrarily time-varying signal $\vec{E}(t)$ is given by:[143]

$$\vec{P}(t) = \epsilon_0 \int_0^\infty \chi(\tau)\vec{E}(t - \tau)d\tau. \tag{5.2}$$

The half-sided Laplace transform of Eq. (5.2) is expressed as:[143]

$$\vec{P}(\omega) = \epsilon_0\chi(\omega)\vec{E}(\omega) = \epsilon_0(\epsilon^*(\omega) - 1)\vec{E}(\omega), \tag{5.3}$$

where $\epsilon^*(\omega) = \epsilon'(\omega) - i\epsilon''(\omega)$ represents the frequency-dependent complex permittivity.

5.1.2 Debye relaxation model and phenomenological generalization

The Debye relaxation mechanism elucidates the classical scenario of dielectric response, involving a collection of identical, non-interacting dipoles that are unrestricted in their

movement within a fluidic medium.[144] Following this model, the permittivity is expressed by:[145]

$$\epsilon^*(\omega) = \epsilon_\infty + \frac{\Delta\epsilon}{1 + i\omega\tau}, \tag{5.4}$$

where $\Delta\epsilon = \epsilon_s - \epsilon_\infty = \lim_{\omega\to 0}\epsilon'(\omega) - \lim_{\omega\to\infty}\epsilon'(\omega)$. In terms of real and imaginary parts:[145]

$$\epsilon'(\omega) = \epsilon_\infty + \frac{\Delta\epsilon}{1 + (\omega\tau)^2}, \tag{5.5}$$

and

$$\epsilon''(\omega) = \frac{\omega\tau\Delta\epsilon}{1 + (\omega\tau)^2}. \tag{5.6}$$

The Debye model assumes an absence of a distribution in reorientation times; however, this assumption frequently does not align with reality. In fact, the relaxation peaks observed in various substances often manifest as broad and asymmetrical. Such types of relaxation are more accurately characterized by a Havriliak-Negami description (see Section 4.3.1), whereafter terms of permittivity is expressed as follows:[145, 146]

$$\epsilon^*(\omega) = \epsilon_\infty + \frac{\Delta\epsilon}{(1 + (i\omega\tau_{HN})^\alpha)^\gamma}. \tag{5.7}$$

The loss peak maxima can be obtained according to:[145]

$$\tau_{\max} = \tau_{HN}\left[\sin\left(\frac{\alpha\gamma\pi}{2+2\gamma}\right) \Big/ \sin\left(\frac{\alpha\pi}{2+2\gamma}\right)\right]^{1/\alpha} \tag{5.8}$$

5.1.3 Suppressed visibility of conductivity effects

Highly conductive materials, such as electrolytes, introduce an extra component to the imaginary part of the permittivity through direct current conductivity. This contribution arises from the electrical mobility that the ions posses and can be quantified as follows:

$$\epsilon''_{cond}(\omega) = \frac{\sigma_{DC}}{\omega\epsilon_0}. \tag{5.9}$$

This contribution is often so strong that the relaxation peaks in the ϵ'' are hard to resolve. One method to overcome this effect, consists in deriving ϵ'' from the real part of the permittivity ϵ' where conductivity effects are absent. For sufficiently broad loss peaks, this can be achieved through the following expression:[147]

$$\epsilon''(\omega) \approx -\frac{\pi}{2}\frac{d\epsilon'(\omega)}{dln(\omega)} \equiv \epsilon''_{der}. \tag{5.10}$$

5.2 Rheology

5.2.1 Newtonian fluid

The viscosity of a fluid can be determined using for instance a rheometer, wherein the sample is positioned between two parallel plates and subjected to shear stress (see Figure 5.1). In the case where the fluid exhibits Newtonian behavior—meaning that its viscosity is independent of the applied shear rate at a given temperature—the viscosity is then linearly related to the applied shear rate $\dot{\gamma}$ and to the shear stress σ by the following equation:[148]

$$\eta = \frac{\sigma}{\dot{\gamma}} = \frac{F}{A\dot{\gamma}}, \tag{5.11}$$

where F represents the tangential force applied to the surface of the plates, and A denotes the surface area.

The shear stress in the planar configuration is induced by Couette flow, wherein one plate moves at a constant speed while the other remains stationary. The shear rate $\dot{\gamma}$ quantifies the rate at which the shearing deformation occurs and is determined by the ratio of the velocity of the moving plate v to the distance between the two parallel plates h:[148]

$$\dot{\gamma} = \frac{v}{h} = \frac{\omega R}{h}, \tag{5.12}$$

where ω is the angular velocity and R the plate radius.

5.2.2 Viscoelastic behavior

Certain fluids not only demonstrate viscous flow characteristics but also display elastic deformation properties. This phenomenon is known as viscoelastic behavior, falling somewhere between that of an ideal Hookean elastic solid and a Newtonian fluid.

In case of ideal elastic behavior with instantaneous and linear response, the shear stress (σ) and the shear strain (γ) are related according to *Hooke's law*:[149]

$$\sigma = G\gamma, \tag{5.13}$$

where G is the shear modulus.

5.2.3 Dynamic experiment

It is possible to determine the viscosity of viscoelastic materials through dynamic or oscillatory experiments, where the shear strain γ is not static but sinusoidal. The complex forms of the shear strain and shear rate are then given by:[149]

$$\gamma^*(t) = \gamma_0 e^{i\omega t}, \tag{5.14}$$

and

$$\dot{\gamma}^*(t) = i\gamma_0 \omega e^{i\omega t}. \tag{5.15}$$

In the linear viscoelastic domain, where the stress amplitude γ_0 is sufficiently low, the measured stress is also sinusoidal, given by:[149]

$$\sigma^*(t) = \gamma_0 e^{i(\omega t+\delta)}, \tag{5.16}$$

where δ is the phase shift between stress and strain. For $\delta = \pi/2$ the fluid is considered purely Newtonian and for $\delta = 0$ an ideal elastic behavior takes place. δ value between these two ideal limits reflect a viscoelastic behavior. Additionally one defines the complex shear modulus G^* and the complex viscosity η^* in the frequency domain, as follows:[149]

$$G^*(\omega) = G'(\omega) + iG''(\omega) = \frac{\sigma^*}{\gamma^*} = \frac{\sigma_0}{\gamma_0} e^{i\delta}, \tag{5.17}$$

and,

$$\eta^*(\omega) = \eta'(\omega) + i\eta''(\omega) = \frac{G^*(\omega)}{i\omega}. \tag{5.18}$$

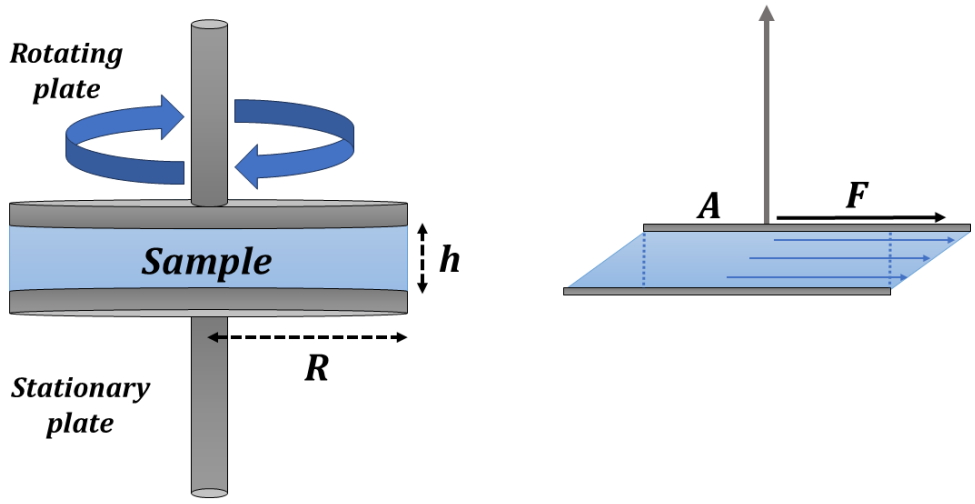

Figure 5.1: Planar configuration of a viscometer: (left) the sample is between two parallel plates, the upper plate is rotating and the lower one is stationary. (right) Shear stress induced by Couette flow.

6 Experimental aspects

6.1 Sample preparation

All samples were prepared within a rigorously controlled moisture environment, achieved using a glovebox. The NMR samples were flame sealed in glass tubes after several freeze-thaw-pump cycles. The dielectric spectroscopy cell was filled inside a glovebox. In the case of viscosimetry measurements, the lower plate was filled directly at the rheometer, where the possibility of moisture contamination could not be entirely ruled out.

6.1.1 Succinonitrile-glutaronitrile mixtures

The procedure outlined by Lunkenheimer *et al.*[31] served as the basis for our sample preparation. SN was cut into few pieces and then heated to 338 K until it transitioned into the liquid phase. Subsequently, GN was added under vigorous stirring. Deuterated Succinonitrile (SN-d_4, see Figure 6.1) had been synthesized in a previous investigation [150] and was kindly supplied by Herbert Zimmermann (MPI-MF, Heidelberg), while protonated SN (99%) and GN (99%) were procured from Sigma-Aldrich.

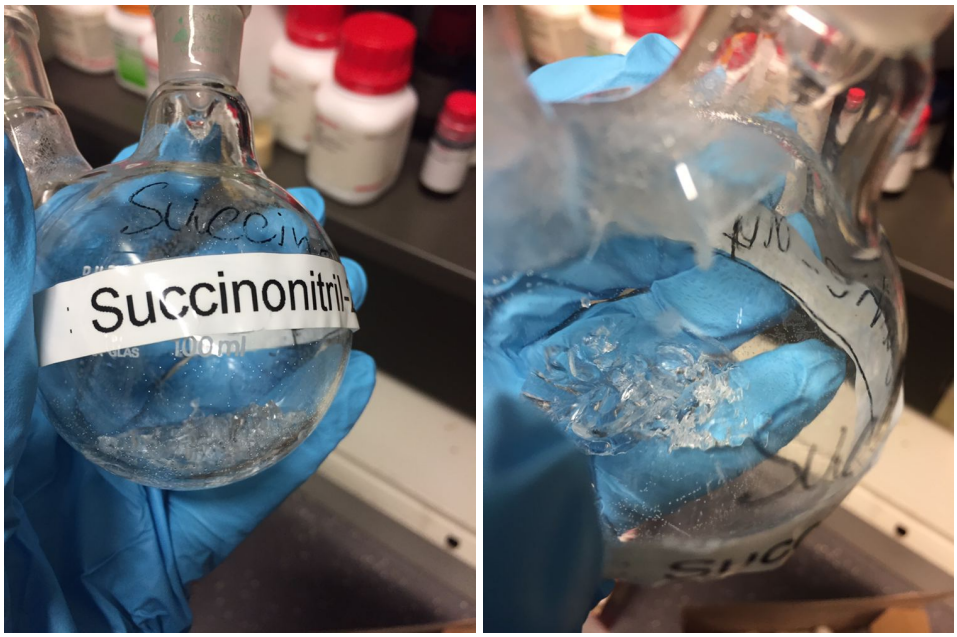

Figure 6.1: Deuterated Succinonitrile (SN-d_4).

Two mixtures of $SN_{0.6}GN_{0.4}$ and $SN_{0.2}GN_{0.8}$ were prepared. Due to the availability of relevant data for comparison,[31, 32, 35, 36, 39] the $SN_{0.6}GN_{0.4}$ sample was selected as the focal point of this study. This decision was influenced by previous research,[39] which identified the chosen ratio as ideal for achieving optimum ionic conductivity.

Dr. Wolf Hiller from the NMR department of the Faculty of Chemistry and Chemical Biology conducted ^{13}C experiments on SN-d_4 dissolved in deuterated dimethyl sulfoxide (DMSO-d_6) and *Dr. Michael Storek* conducted the analysis to determine the extent of deuteration. The determination of the degree of deuteration in the SN sample was derived from the intensity ratio of the CD_2 quintet to that of the CDH triplet, constituting approximately 16% of the integrated intensity in the natural abundance ^{13}C solution spectrum. Our findings revealed a deuteration level of 91%, and the chemical purity of the sample exceeded 97%.

6.1.2 Glutaronitrile-fumaronitrile mixtures

To investigate the impact of altered conformational rigidity, achieved by introducing a double bond in the center of the dinitrile molecule, the GN molecules were replaced with Fumaronitrile (FN, N=C-CH=CH-C=N). Due to the significant crystallization tendency observed in pure FN, it was found that the formulation of Li-doped ambient temperature liquids necessitated a substantial addition of GN to FN; only 20% FN could be feasibly incorporated. The preparation of the $FN_{0.2}GN_{0.8}$ samples involved thoroughly stirring the appropriate amount of FN (with a melting point near 370 K) with GN at room temperature.

6.1.3 Cyclohexanol-cyclooctanol mixtures

Samples of cycloalcohols containing $HEX_{0.6}OCT_{0.4}$ and $HEX_{0.4}OCT_{0.6}$ were mixed under heavy stirring. Protonated HEX and OCT as well as the deuterated cyclohexanol (HEX-d_{11}) were purchased from Sigma-Aldrich. The degree of deuteration of HEX-d_{11} was reported by the supplier to be 98%.

6.1.4 Lithium doping

Lithium doping was achieved through the addition of either lithium bis(trifluoromethanesulfonyl)imide (LiTFSI) or lithium hexafluorophosphate ($LiPF_6$) to the dinitrile or to the cycloalcohol matrix. LiTFSI (99%) was procured from Sigma-Aldrich, while $LiPF_6$ (98%) was obtained from ThermoFisher Scientific. The lithium salts underwent a preliminary drying process at T = 353 K for a minimum of 8 hours immediately prior to usage. Subsequently, they were finely ground to optimize dissolution and incorporated into the hosting mixture under intense stirring. Karl Fischer titration revealed water fractions of less than 0.05% for all doped samples. Doped samples were stored in sealed aluminum bags to prevent moisture contamination.

6.2 Setup and hardware

The ^{2}H and ^{7}Li NMR spectroscopy, as well as relaxometry measurements, were carried out using home-built spectrometers operating at Larmor frequencies of 46.5 MHz and 116.9 MHz, respectively. Typically, the 90° pulses had durations of 2.5 μs and 3 μs for ^{2}H and ^{7}Li, respectively.

For ^{1}H diffusion NMR, experiments were conducted at a Larmor frequency of 87.0 MHz in the fringe field of a superconducting magnet, with a gradient strength of g = (34.1 ± 0.2) T/m; refer to Section 6.3.2 for details regarding gradient calibration.

The ^{7}Li diffusion experiments were performed at the NMR department of the Faculty of Chemistry and Chemical Biology by *Dr. Bastian Grabe*. A Bruker Avance III HD Nanobay 400 MHz spectrometer with a 5 mm RT BBFO smart probe was used. Stimulated echoes, incorporating longitudinal eddy current delays with bipolar gradients and spoil pulses, were employed.[151]

Dielectric spectroscopy measurements were systematically performed employing a Novocontrol system, featuring an Alpha impedance analyzer and a Quatro temperature controller. The frequency spectrum, ranging from 10^{-2} to 10^{6} Hz, was scanned. The standard temperature stability achieved during these measurements was maintained within a narrow margin of ± 0.1 K.

The rotational zero-shear viscosities were measured using an Anton-Paar MCR 502 rheometer coupled with an EVU20 temperature module, ensuring temperature stability within ±0.2 K. The experimental configuration involved positioning the samples between two parallel plates spaced by h = 0.9 mm. The lower plate, with a fixed position, had a diameter of 2R = 50 mm. Simultaneously, the upper plate undergoes rotation with an angular frequency ω_{rot}, resulting in a shear rate $\dot{\gamma}$ as described in Section 5.2.3. All viscosity measurements were conducted within the liquid phase in the linear-response regime.

6.3 Calibration measurements

6.3.1 Pulse field gradient calibration

The calibration sample (P/N Z10906) utilized in the Pulsed Field Gradient (PFG) experiment is provided by Bruker and comprises 1% H_2O, 0.1% $GdCl_3$, and 0.1% $^{13}CH_3OH$. To determine the diffusion coefficients, the gradient strength was linearly varied in 16 steps, ranging from 10% to 80% of its maximum (approximately 0.5 T/m). The gradient was applied for pulse lengths (δ) ranging from 1.6 to 2.8 ms. In addition, diffusion delays (Δ) between 0.3 and 1 s, and a 90° pulse length for ^{7}Li of 9 ms, were employed.

Furthermore, the temperature sensor was calibrated using 80% Glycol in DMSO-d_6 based on the calibration procedure reported in ref.[152] for high temperature calibration.

6.3.2 Static field gradient calibration

The gradient calibration for the SFG measurements involved using an 8 mol/L lithium chloride solution (LiCl+H_2O), procured from Sigma-Aldrich. The proton diffusion coefficient (D_H) of the solution at room temperature (T = 291 K) was previously determined to be 6.61 × 10^{-10} m^2s^{-1} at the NMR department of the Faculty of Chemistry and Chemical Biology by *Dr. Bastian Grabe*.

Therefore, the SFG experiment detailed in Section 4.4.4, was carried out at T = 291 K on the LiCl+H_2O solution mentioned above. The evolution time t_p ranged from 20 to 400 μs, and the mixing time spanned from 10^{-5} to 10^{1} s. Additionally, the longitudinal relaxation time was determined through an IR experiment using a HE refocusing sequence, as explained in Section 4.4.2.

The normalized magnetization curves obtained from both the SFG and IR experiments are presented in Figure 6.2, along with fits using Eq. (4.41) and Eq. (4.37). The correlation times τ_c for each t_p value, obtained using Eq. (4.41), are plotted against the inverse square of the evolution time t_p^{-2} in Figure 6.3. By rearranging Eq. (4.42) and using the slope of the linear curve, the gradient strength g was determined to be 34.1 ± 0.2 T/m.

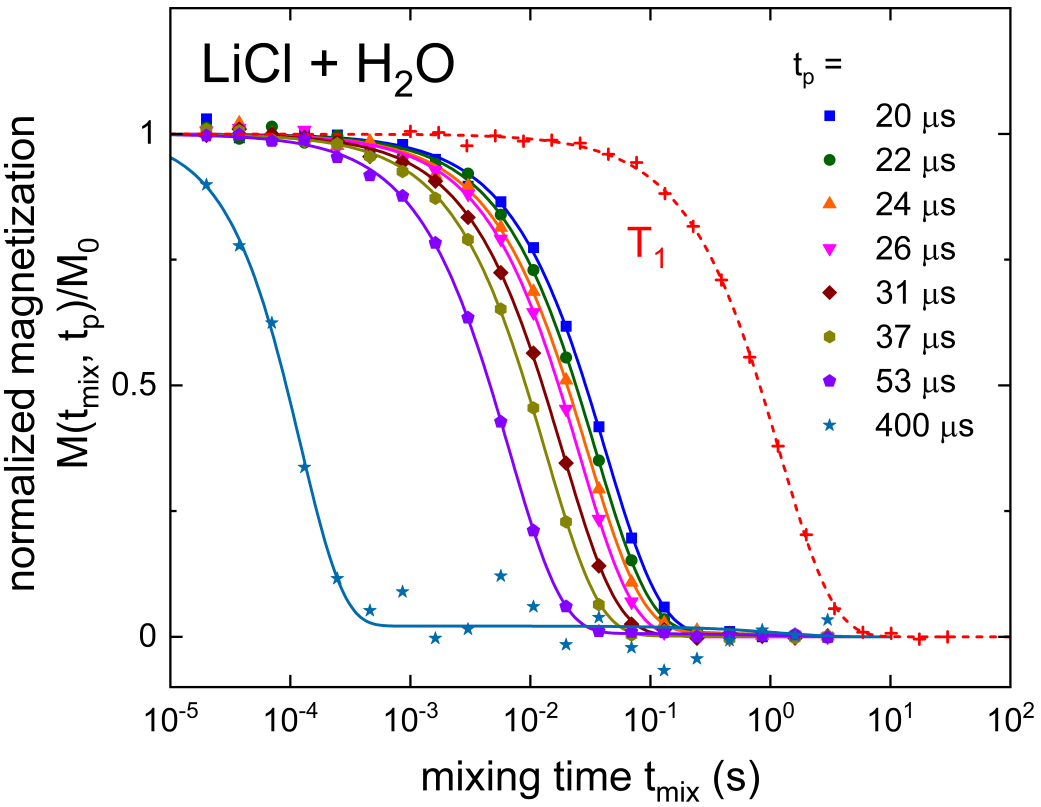

Figure 6.2: Static field gradient-stimulated proton-echo decays observed in lithium chloride solution at T = 291 K, with measurements taken at various evolution times t_p. The solid lines depict fits using Eq. (4.41). The red plusses and the dotted line represent an independent measurement of the longitudinal relaxation time and its respective fit.

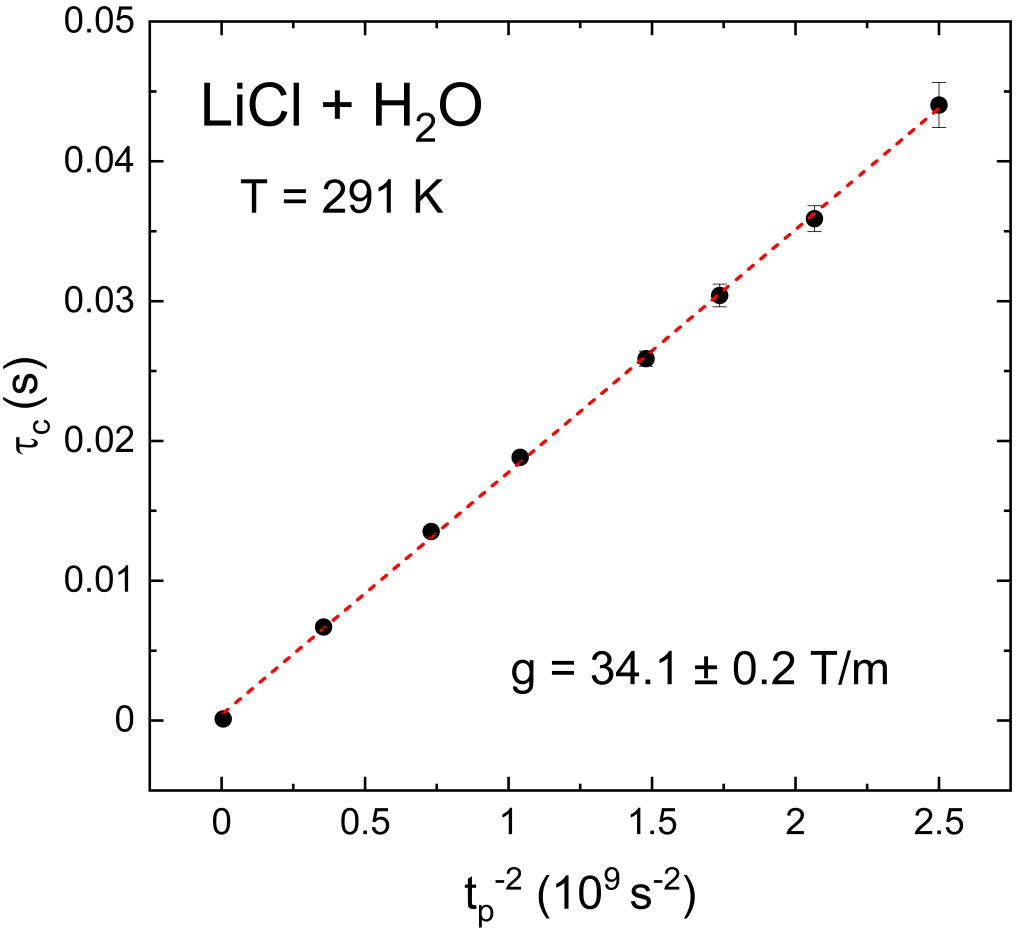

Figure 6.3: Correlation times τ_c deduced from the data in Figure 6.2 plotted against the inverse square of the evolution time t_p^{-2} for lithium chloride solution at T = 291 K. The proton diffusion coefficient of the calibration sample is known to be $D_H = 6.61 \times 10^{-10}$ $m^2 s^{-1}$. Utilizing Eq.(4.42), the strength of the gradient, g, is calculated to be 34.1 ± 0.2 T/m.

7 Results and Discussion

7.1 Neat and doped dinitriles

7.1.1 Undoped succinonitrile-glutaronitrile matrix

Dielectric spectroscopy measurements

The SN-GN mixture has been previously the subject of dielectric spectroscopy investigations aimed at elucidating the molecular dynamics before and after doping with Li salt. Bauer *et al.*[31] observed a characteristic α relaxation with non-Arrhenius temperature dependence in the undoped $SN_{0.6}GN_{0.4}$. They also reported that the plastic phase of the undoped mixture can undergo supercooling, exhibiting a glass transition temperature of approximately 144 K. Geirhos *et al.*[39], on the other hand, investigated the dielectric properties of $SN_{0.6}GN_{0.4}$ after doping with 1% $LiPF_6$, revealing a strong coupling between ionic and reorientational motions. In this work, we augment dielectric spectroscopy measurements with NMR spectroscopy to further investigate the reorientational motion of dinitrile molecules and Li ions within the SN-GN matrix. To enhance data comparability, we remeasure the dielectric properties of protonated $SN_{0.6}GN_{0.4}$ before after doping with $LiPF_6$. The effects of using another Li salt on the matrix dynamics are also investigated by introducing LiTFSI at various concentrations. Additionally, we examine potential isotopic effects by conducting dielectric spectroscopy on $(SN\text{-}d_4)_{0.6}(GN)_{0.4}$.

The frequency-dependent dielectric constants, ϵ', and dielectric losses, ϵ'', for deuterated $(SN\text{-}d_4)_{0.6}(GN)_{0.4}$ are presented in Figure 7.1(a) and (b), respectively.

Examining Figure 7.1(a) in greater detail, a noticeable step-like increase in the frequency-dependent dielectric constant ϵ' is observed, ranging from approximately 70 to 100 within 200 to 160 K. This phenomenon is accompanied by distinctive peaks in the dielectric loss ϵ'' as shown in Figure 7.1(b), indicative of the relaxation behavior associated with the reorientational motion of the dinitrile molecules. These peaks shift towards lower frequencies with decreasing temperature, ultimately experiencing a significant reduction in strength below 160 K.

Earlier studies demonstrated a comparable decrease in relaxation strength for both $SN_{0.87}GN_{0.13}$ and other nitrile mixtures, as reported in references [34] and [153]. This reduction, however, does not significantly impact the relaxation time, as illustrated by the rescaled dielectric loss data in in Figure 7.1(b), recorded for $(SN\text{-}d_4)_{0.6}(GN)_{0.4}$ at 165 K during the heating run.

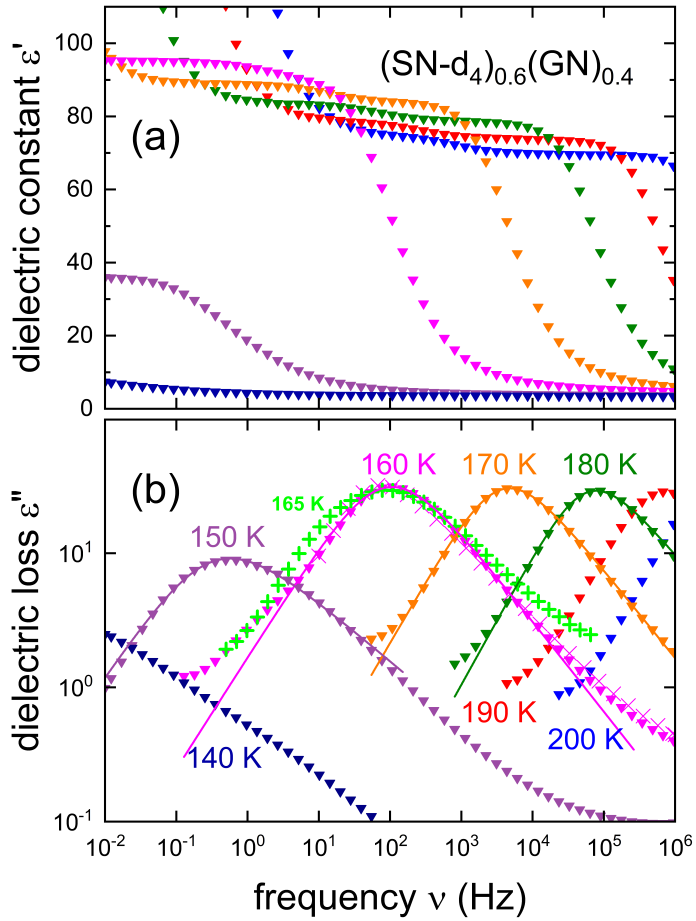

Figure 7.1: Frequency dependent measurements of (a) the real part and (b) the imaginary part of the complex dielectric permittivity of $(SN\text{-}d_4)_{0.6}(GN)_{0.4}$ in the plastic crystalline phase as published in ref.[111]. Solid symbols denote data collected during the cooling process, while crosses (×) depict dielectric loss spectra from [31] pertaining to protonated $SN_{0.6}GN_{0.4}$. Remarkably, without any rescaling, spectra from fully protonated and partially deuterated samples align, dismissing the existence of a significant H/D isotope effect. Plusses (+) represent dielectric loss data for $(SN\text{-}d_4)_{0.6}(GN)_{0.4}$ at 165 K during heating, with peak amplitude and frequency rescaled for comparative analysis. Solid lines correspond to fits using Eq. (5.7) with parameters $\alpha = 0.9 \pm 0.1$ and $\gamma = 0.7 \pm 0.1$.

A further comparison at T = 160 K between the dielectric loss data obtained for the deuterated mixture under investigation and the one reported in reference [31] for the corresponding protonated mixture, see crosses (×) in Figure 7.1(b), reveals no discernible isotopic effects. Additionally, Eq. (5.7) can be effectively employed to model the relaxation peaks while Eq. (5.8) can be utilized to extract the associated relaxation time constants. The reorientational relaxation times will be comprehensively discussed in Section 7.1.4 below.

Additionally, in Figure 7.2 we present the temperature-dependent dielectric loss recorded at three different frequencies while both cooling and heating the sample. An initial transi-

tion occurs around T = 235 K, along with the previously discussed reduction observed at temperatures below 160 K. This reduction persists throughout the heating measurements until reaching 265 K. Given the temperature-dependent nature of the isomeric distribution, a plausible explanation for this phenomenon could involve either a partial orientational alignment or a rapid increase in the centro-symmetric *trans* conformation (refer to Section 2.1) expected to display a weak dipole moment.

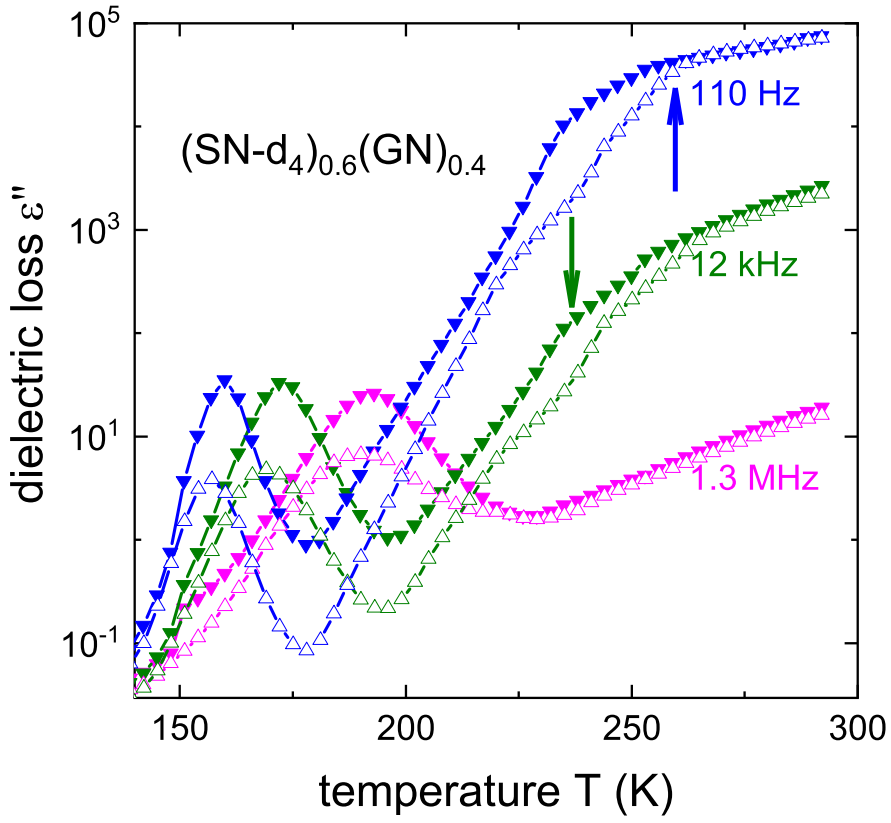

Figure 7.2: Temperature dependent dielectric loss of $(SN\text{-}d_4)_{0.6}(GN)_{0.4}$ across various frequencies measured during cooling (solid triangles pointing down) or heating (open triangles pointing up) as published in ref.[111]. The lines are drawn to guide the eye. The arrows emphasize key temperatures marking phase transitions.

Moreover, Figures 7.3(a) and (b) illustrate the real part of the conductivity, σ', and the imaginary part of the modulus, M'', respectively. The real part of the conductivity, where the contribution of electrode polarization was neglected, exhibits a distinctive σ_{DC} plateau below 10^{-5} S/cm for T = 247 K. This plateau shifts towards lower frequencies and manifests at lower conductivity values as the temperature decreases. Comparison with the relaxation data presented by Lunkenheimer *et al.*[31] for the protonated $SN_{0.6}GN_{0.4}$ mixture, reveals that these plateau values are in good agreement. An additional and more elaborate discussion of the conductivity is conducted in Section 7.1.4.

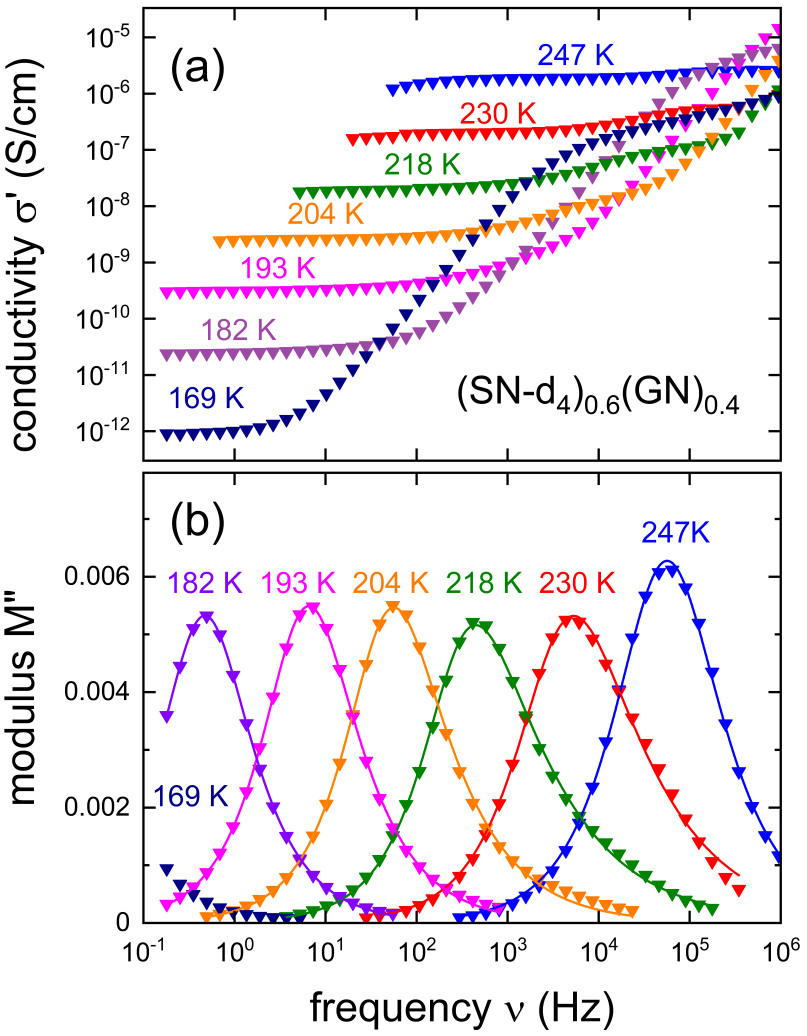

Figure 7.3: Frequency dependent measurements of (a) the real part of the conductivity σ' and (b) the imaginary part of the modulus M'' for $(SN\text{-}d_4)_{0.6}(GN)_{0.4}$ measured during cooling. Frame (a) was previously published in ref.[111]. The electrode polarization contribution for σ' was neglected. All the data were collected during the plastic crystalline phase, except for the data presented at T = 247 K, which was obtained during the liquid phase. Solid lines in frame (b) correspond to fits using Eq. (5.7) with parameters $\alpha = 0.9 \pm 0.1$ and $\gamma = 0.7 \pm 0.2$.

Furthermore, the σ_{DC} are accompanied with characteristic peaks in the imaginary part of the modulus M'' as illustrated in Figure 7.3(b). These peaks appears within the same temperature windows as the σ_{DC} values and similarly to the ϵ'', they shift towards lower frequencies with lower temperates. Additionnally, one can use Eq. (5.7) in analogy to the dielectric loss, to fit the peaks in the imaginary part of the modulus M''.

Dielectric spectroscopy measurements were additionally performed on the protonated $SN_{0.6}GN_{0.4}$ mixture to exclude furthermore potential isotopic effects and enhance data comparability. Figure 7.4(a) and (b) show the obtained frequency-dependent dielectric

constants, ϵ', and dielectric losses, ϵ'', respectively.

Upon scrutinizing Figure 7.4(a), one can discern similar dielectric characteristics between the deuterated and protonated $SN_{0.6}GN_{0.4}$. Specifically, the dielectric constant ϵ' exhibits a comparable step-like increase between 60 and 75. Likewise, in Figure 7.4(b), the dielectric loss ϵ'' manifests a similar shift in relaxation peaks within this temperature range. However, no discernible decrease in relaxation strength below 160 K was observed; Bauer *et al.*[31] have also reported only a marginal reduction for protonated $SN_{0.6}GN_{0.4}$.

Considering the phase diagram of the binary mixture SN-GN (refer to Section 2.1), we explored the reorientational motion of dinitrile molecules also at high GN concentrations. In particular, dielectric spectroscopy measurements were performed on the $SN_{0.2}GN_{0.8}$ mixture. The results are illustrated in Figure 7.5(a) for the dielectric constant ϵ' and (b) for the dielectric loss ϵ''.

A comparison between the protonated samples $SN_{0.6}GN_{0.4}$ and $SN_{0.2}GN_{0.8}$ reveals no significant alterations in the dielectric characteristics. The distinctive step-like increase and shift of the α relaxation peaks are also evident in this case. Götz *et al.*[32] reported a phase transition from liquid to plastic crystal at 180 K for this mixture when cooled at low rates ($\leq$ 2 K/min). This transition is entirely circumvented when using higher cooling rates ($\leq$ 5 K/min), leading to the observation of only a glass transition at T = 150 K.[32] In line with the dielectric spectroscopy investigation conducted by the same authors, we do not observe any significant changes in the dielectric features of the sample below 180 K. Finally, it is worth mentioning that the dielectric features observed in the SN-GN mixtures, specifically the reduction in DC conductivity and the observed changes in the dielectric constant, along with the shift of loss peaks towards lower frequencies, are familiar traits in liquid and plastic crystal dielectrics.[154]

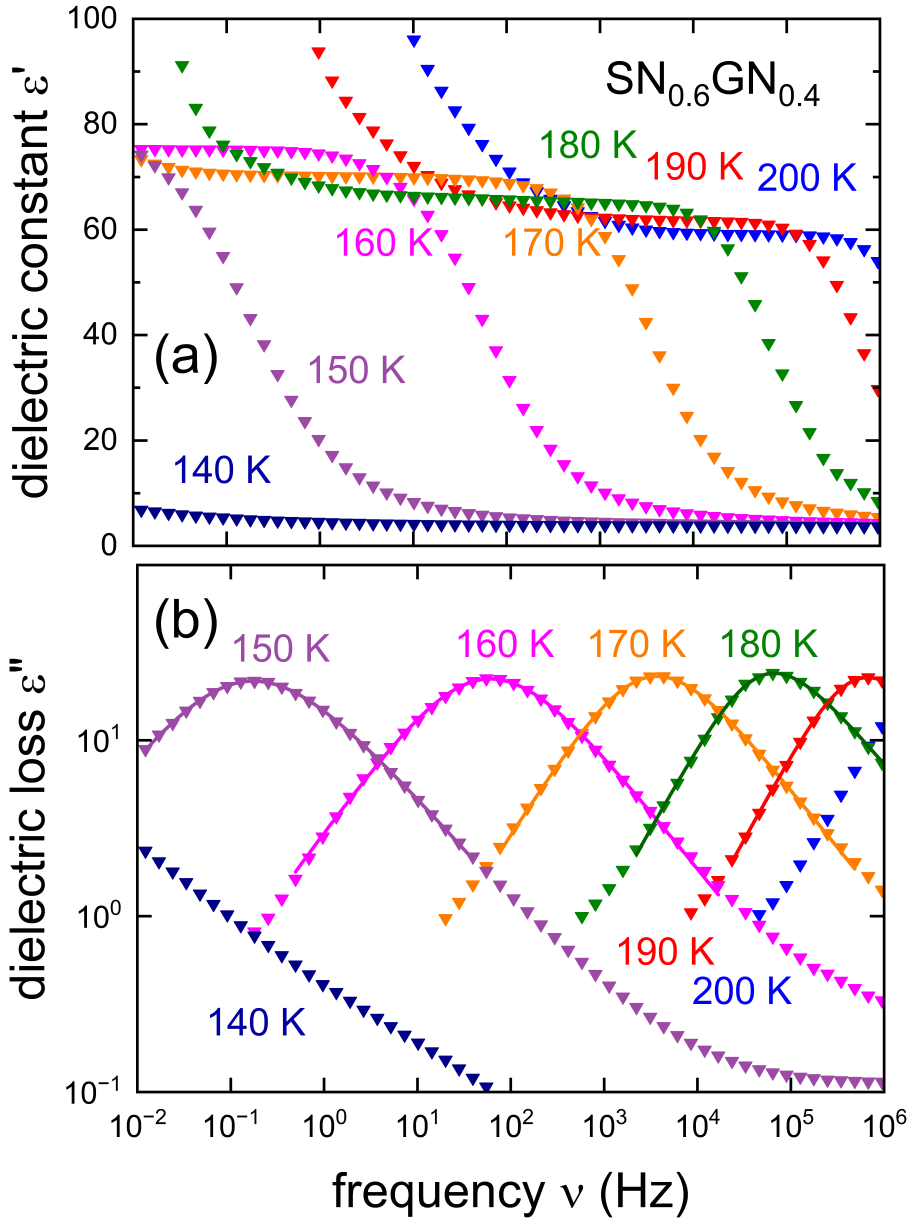

Figure 7.4: Frequency dependent measurements of (a) the real part and (b) the imaginary part of the complex dielectric permittivity of $SN_{0.6}GN_{0.4}$ in the plastic crystalline phase. Data was acquired during cooling. Solid lines correspond to fits using Eq. (5.7) with parameters $\alpha = 0.9 \pm 0.1$ and $\gamma = 0.8 \pm 0.1$.

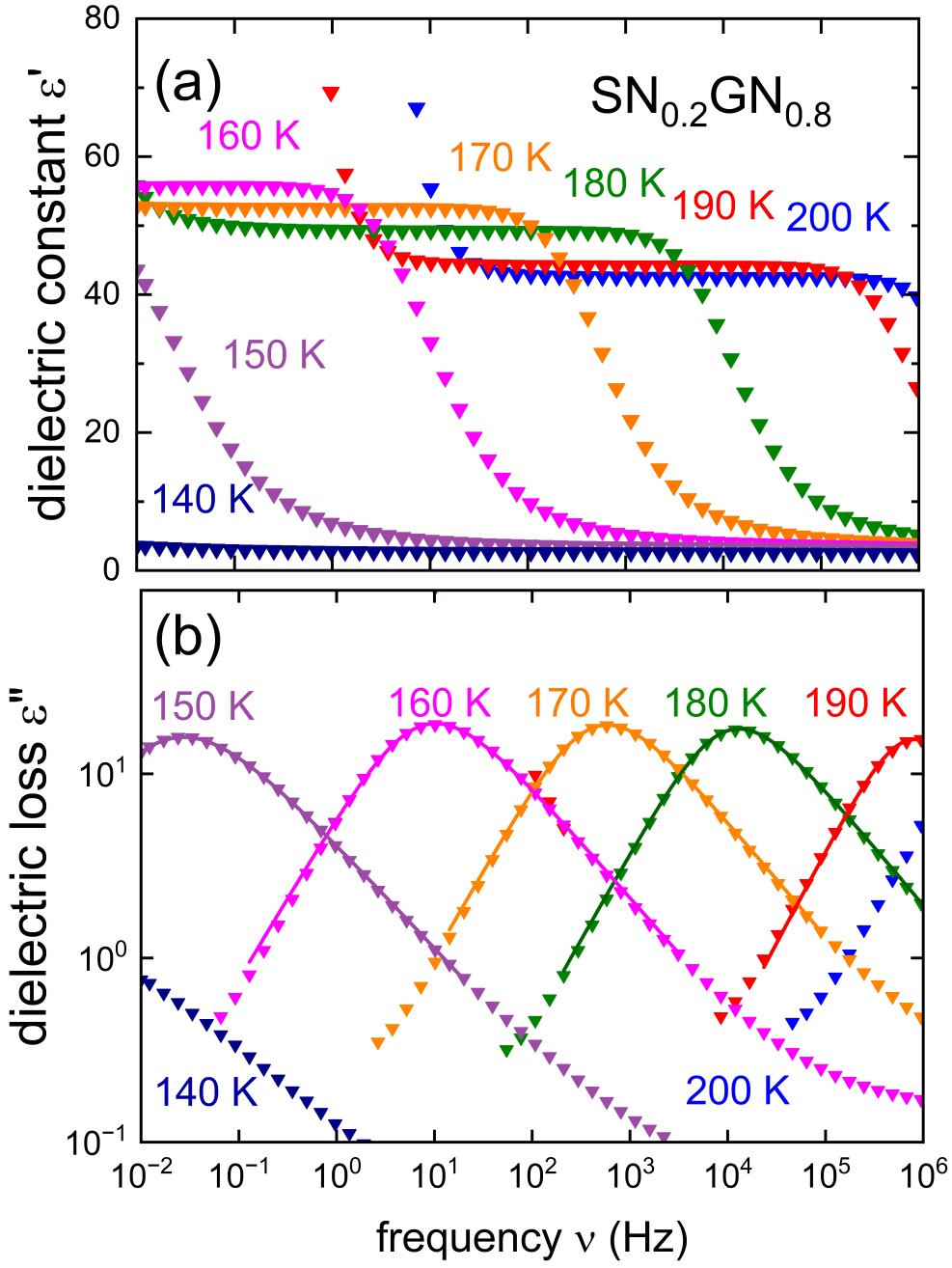

Figure 7.5: Frequency dependent measurements of (a) the real part and (b) the imaginary part of the complex dielectric permittivity of $SN_{0.2}GN_{0.8}$ in the plastic crystalline phase. Data was acquired during cooling. Solid lines correspond to fits using Eq. (5.7) with parameters $\alpha = 0.9 \pm 0.1$ and $\gamma = 0.8 \pm 0.1$.

Deuterium spectroscopy

Figure 7.6 illustrates the static ^{2}H FID spectra of $(SN\text{-}d_4)_{0.6}(GN)_{0.4}$ obtained during cooling for temperatures ranging from 235 to 192 K. The spectrum at 235 K displays a distinctive peak with a line width of few kilohertz. This width notably increases as the temperature decreases, an indication that the spin-spin relaxation decreases in accordance with $1/(\pi\Delta\nu_{1/2})$, where $\Delta\nu_{1/2}$ represents the inverse full width at half maximum.

Additionally, Figure 7.7 presents the static solid echo spectrum acquired at T = 150 K for $(SN\text{-}d_4)_{0.6}(GN)_{0.4}$. The spectrum displays the characteristic lineshape indicative of a Pake doublet, with a splitting of approximately 120 kHz, consistent with the typical value of the quadrupolar coupling constant for deuterium.[136] Notably, the intensities of the two horns are slightly unequal.

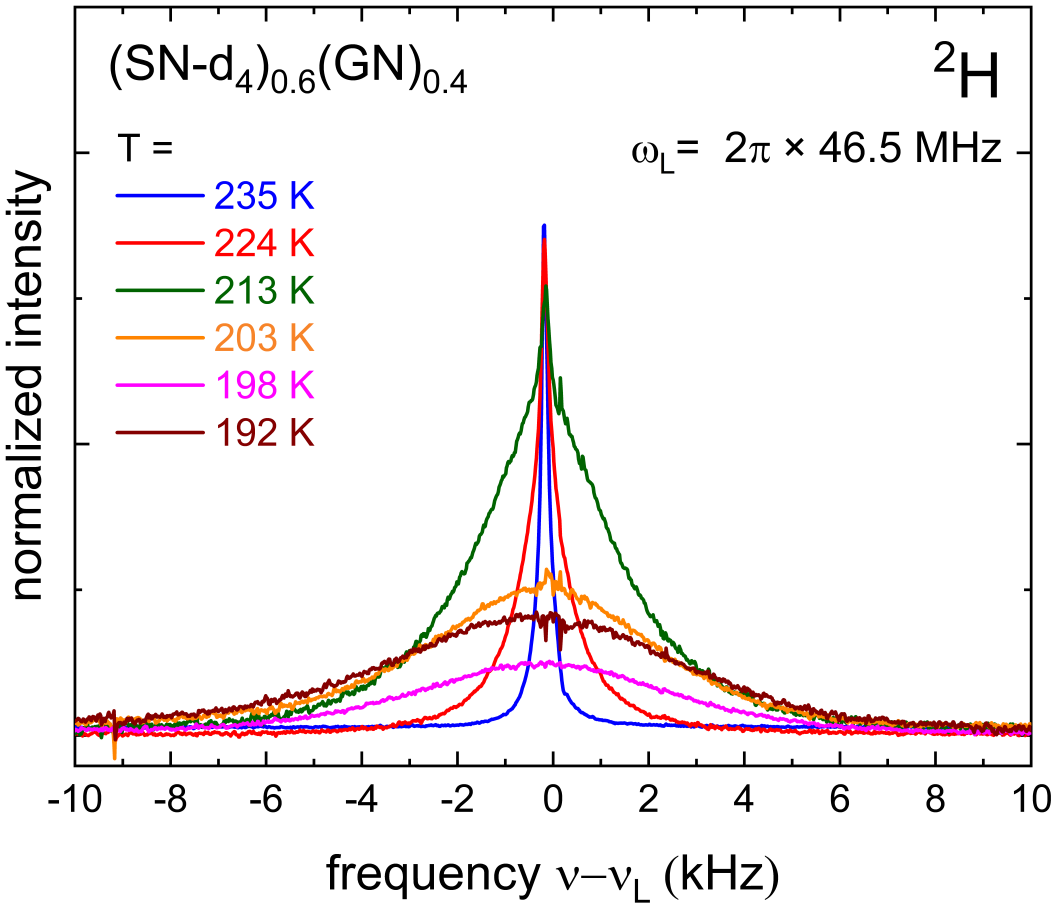

Figure 7.6: ^{2}H FID spectra recorded for $(SN\text{-}d_4)_{0.6}(GN)_{0.4}$ at $\omega_L = 2\pi \times 46.5$ MHz during cooling in a temperature range between 235 and 192 K.

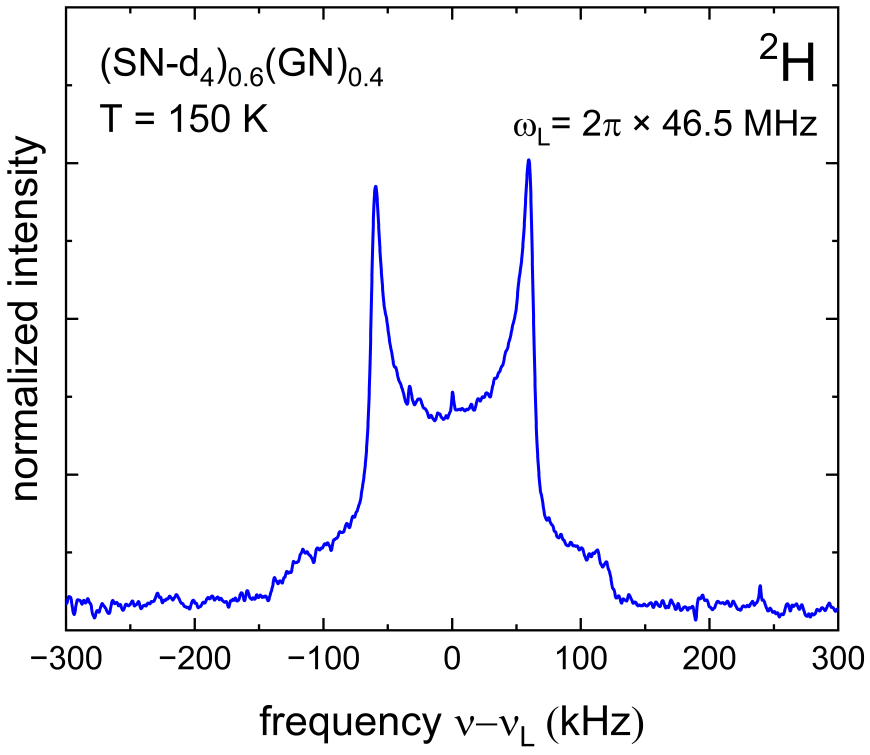

Figure 7.7: ^{2}H solid echo spectrum recorded for $(SN\text{-}d_4)_{0.6}(GN)_{0.4}$ at $\omega_L = 2\pi \times 46.5$ MHz and T = 150 K. The spectrum exhibits a horn splitting of approximately 120 kHz.

Deuterium relaxometry

In addition to conducting spectroscopy measurements, we performed extensive relaxometry assessments across a broad temperature range for $(SN\text{-}d_4)_{0.6}(GN)_{0.4}$. The temperature-dependent spin-lattice relaxation time, T_1, and spin-spin relaxation time, T_2, are illustrated in Figure 7.8, along with their corresponding Kohlrausch exponents. To fit these relaxation times, we utilized Eq. (4.33) and Eq. (4.34) with the HN spectral density from Eq. (4.28). The resulting fit lines are included in Figure 7.8, where γ was set to 0.24, and the timescales were computed using a VFT approach with Eq. (3.2) for the reorientational relaxation times obtained from dielectric spectroscopy measurements (refer to Section 7.1.4).

At elevated temperatures, there is good agreement between the T_1 and T_2 values as it is expected to be the case in the extreme narrowing regime. However, at temperatures below 240 K, the influence of self-diffusion due to magnetic inhomogeneities becomes significant, leading to a noticeable decline in $T_{2,HE}$. In contrast, T_1 exhibits only a slight discontinuity around the same temperature. Furthermore, the calculated fits for the relaxation times, based on the assumption of a predominant quadrupolar interaction, align well with the measured data with the exception of small deviations at high temperatures and below the T_1 minimum. A comparative analysis of the NMR relaxometry data before and after doping is extended in Section 7.1.2.

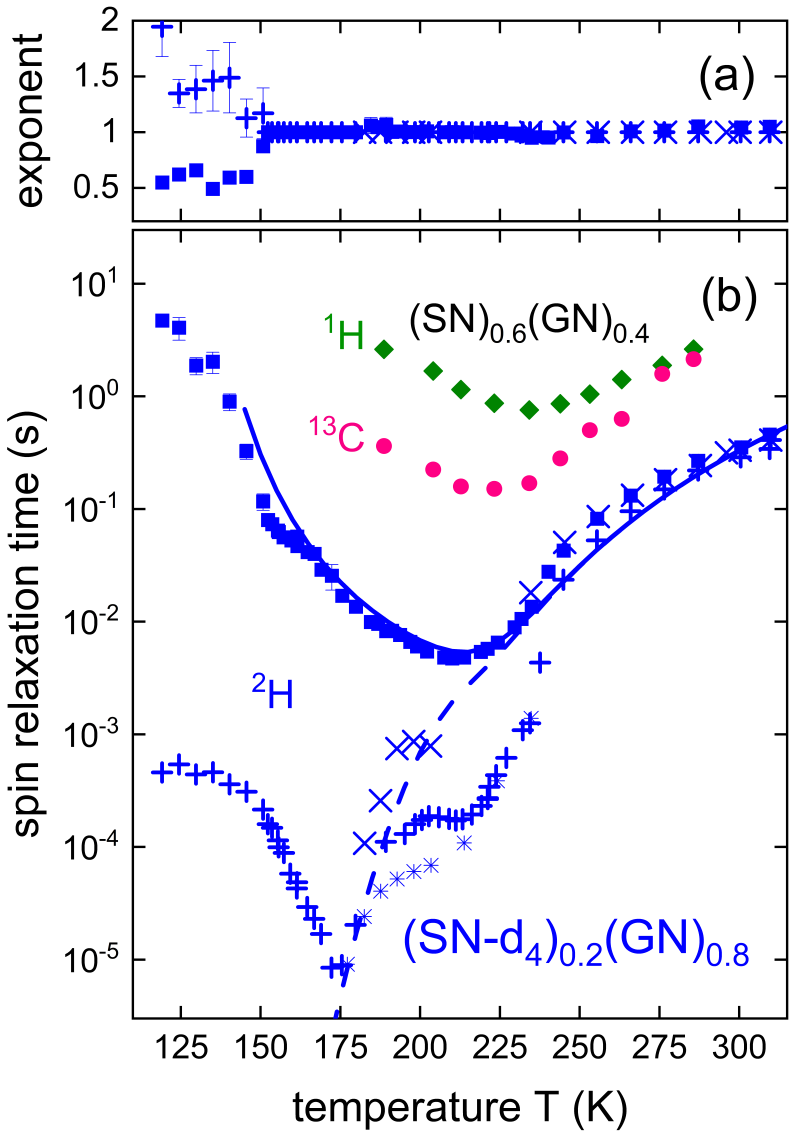

Figure 7.8: The temperature dependent spin-lattice relaxation times T_1 (full symbols) and spin-spin relaxation times T_2 of $(SN\text{-}d_4)_{0.6}(GN)_{0.4}$ as published in ref.[111]. Data obtained at a Larmor frequency of 46.5 MHz during cooling are shown in frame (b). The T_2 values were determined employing Hahn-echo (+, for T > 214 K), CPMG (×), or solid echo (+, for T <214 K) sequences, or calculated from the inverse full width at half maximum $1/(\pi\Delta\nu_{1/2})$ of the FID spectra (stars). Frame (a) provides the corresponding Kohlrausch exponents. The solid line, computed using Eq. (4.33), and the dashed line, using Eq. (4.34), both in conjunction with the spectral density from Eq. (4.28), are also depicted. The ^{1}H and ^{13}C spin-lattice relaxation times from [36] pertain to fully protonated $SN_{0.6}GN_{0.4}$ and were measured at Larmor frequencies of 400 and 100.5 MHz, respectively.

Deuterium stimulated echo measurements

In addition to relaxometry measurements, we conducted stimulated ^{2}H echo experiments on the $(SN\text{-}d_4)_{0.6}(GN)_{0.4}$ mixture to gain insights into slower dynamic processes. Figure 7.9 presents stimulated ^{2}H measurements at various temperatures acquired with a fixed evolution time, t_p = 15 μs. The measurements were conducted using a three-pulse (3P) cos-cos variant of the stimulated echo (STE) experiment, as detailed in Section 4.4.3. Additionally, we employ Eq. (4.39) to derive the correlation times, τ_c, and determine the final state correlation Z. The fits are shown as solid lines in Figure 7.9.

As the temperature decreases, the decay of the stimulated-echo amplitude undergoes a gradual extension over increasingly prolonged periods, resulting in a more elongated decay profile. Notably, the fits using Eq. (4.39) closely align with the measured data.

Furthermore, Figures 7.10(a) and (b) depict the stimulated echo amplitudes plotted against the mixing time, t_{mix}, obtained at T = 149 K for various evolution times, t_p. The data was acquired using a 3P (a) or a 4P (b) cos-cos variant of the STE experiment.

Moreover, to account for the relaxation occurring during t_{mix}, we normalized the data using the fit describing the longitudinal relaxation determined at the corresponding temperature. The spin-lattice relaxation constant at T = 149 K was found to be approximately 110 ms in accordance with the value plotted in Figure 7.8.

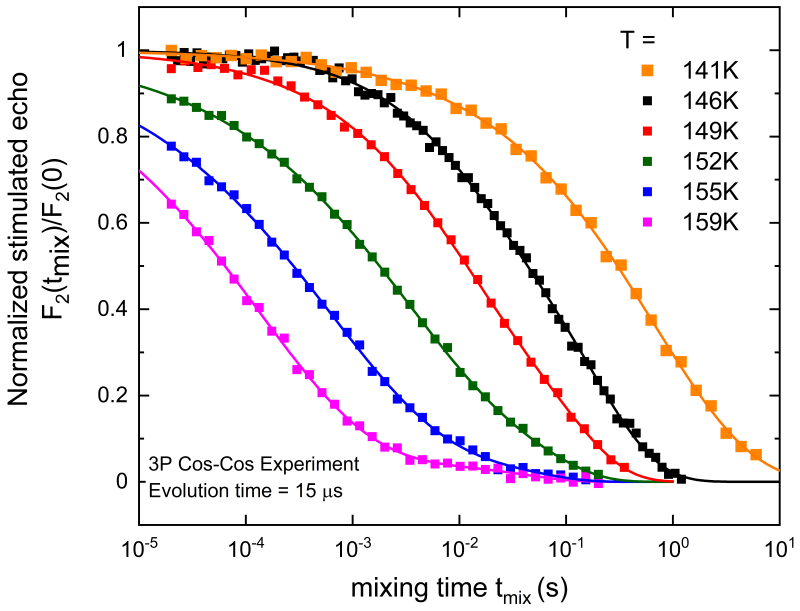

Figure 7.9: Stimulated ^{2}H echo amplitudes measured for $(SN\text{-}d_4)_{0.6}(GN)_{0.4}$ at fixed evolution time t_p = 15 μs as function of the mixing time t_{mix}. The data were obtained through a three-pulse (3P) STE experiment conducted at different temperatures. Solid lines represent fits with Eq. (4.39). The data was not normalized to take the effect of longitudinal relaxation into account.

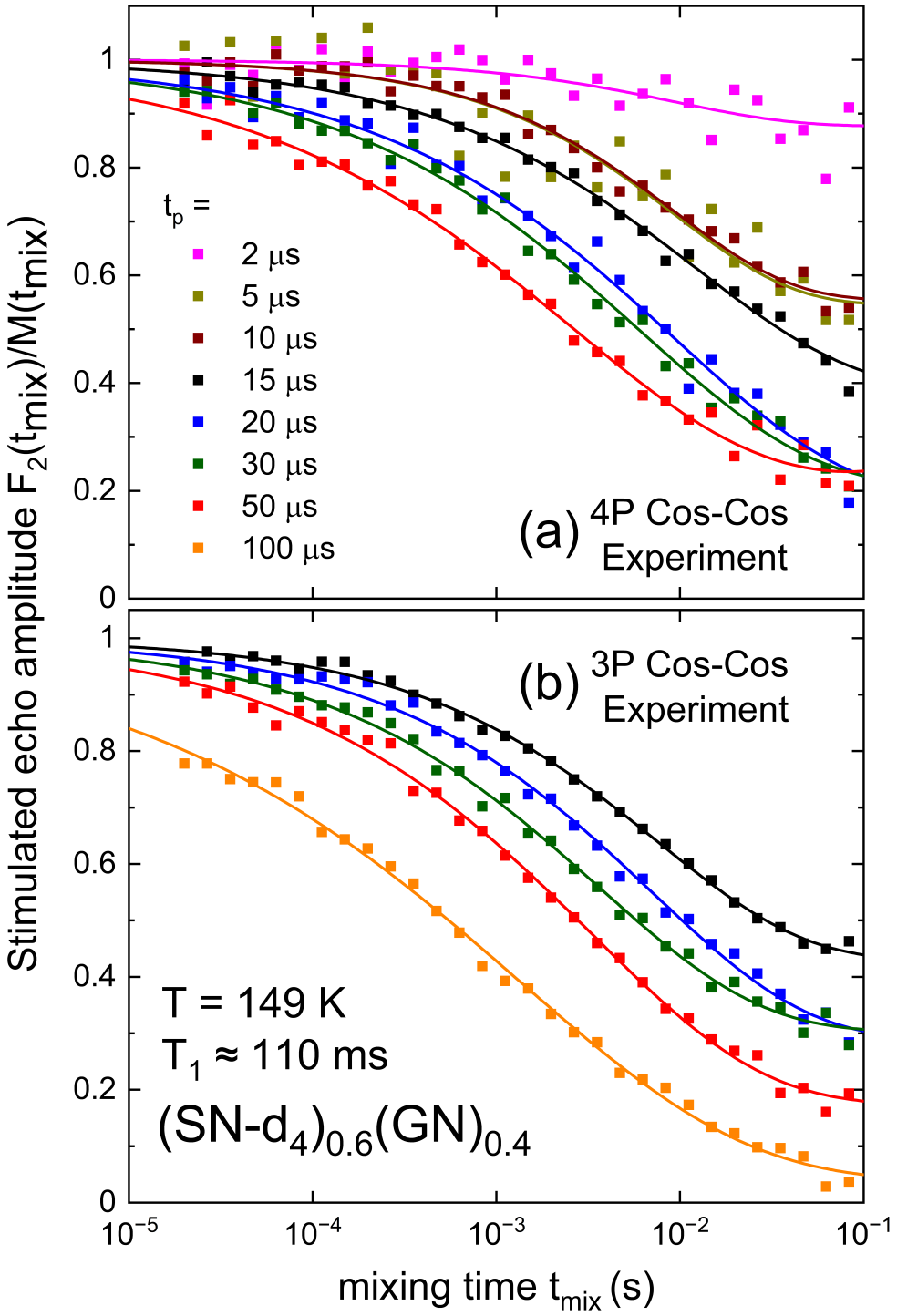

Figure 7.10: Stimulated ^{2}H echo amplitudes measured for $(SN\text{-}d_4)_{0.6}(GN)_{0.4}$ at T = 149 K as function of the mixing time t_{mix}. The measurements were conducted using (a) four-pulse (4P) or (b) three-pulse (3P) STE with varying evolution times, t_p. To take into account relaxation effects during the mixing time, the amplitudes were divided by the longitudinal relaxation fit determined at the same temperature. T_1 was found to be approximately 110 ms. Solid lines reflect fits using Eq. (4.39) without the contribution of the longitudinal relaxtion.

For the 4P and the 3P experiments, a clear correlation between the stimulated echo amplitude and t_p is evident. Additionally, it is noted that extended evolution times (t_p > 100 μs) are necessary to achieve a complete decay of the echo amplitude. Here as well, we use Eq. (4.39) to fit the STE amplitudes but without the contribution of the longitudinal relaxtion. The correlation times and final state correlations extracted via Eq. (4.39) are depicted in Figure 7.11 as functions of the evolution time.

To elucidate the experimental data obtained from STE experiments, we conducted Random Walk simulations, focusing on the isomeric behavior of the SN molecules. For further details, please refer to Appendix A. The correlation times and final state correlations derived from simulation with an angle $\alpha = 1^\circ, 3^\circ$ and 5° are illustrated in Figure 7.11(a) and (b) as dashed lines. Additionally, data corresponding to fully isotropic reorientational processes reported in ref.[155] are presented as solid blue lines.

The correlation time τ_c determined through experimental measurements, as shown in Figure 7.11(b), is approximately 10 ms for short evolution times, consistent with the behavior expected for a fully isotropic reorientational process. However, a significant deviation is observed between τ_c obtained from random walk simulations and experimental measurements. As the evolution time t_p increases, the experimental value of τ_c gradually decreases to around 1 ms. Notably, both the isotropic and simulated lines also converge, displaying a trend similar to that observed in the experimental data.

Furthermore, the final state correlation depicted in Figure 7.11(c) represents the proportion of C-D bonds that have not undergone reorientation during the mixing time. Since there are twelve NMR-relevant positions for the C-D bond inferred from the reorientational dynamics of the SN molecule, the parameter Z is expected to decay to approximately 1/12 for sufficiently long evolution times. This observation aligns with Figure 7.11(c) for t_p = 100 μs. The experimentally determined Z however, exhibits a slower decay compared to the predictions of the isotropic line and simulated data model.

The correlation times obtained through STE experiments will be discussed in Section 7.1.4 with the time constants obtained with dielectric spectroscopy, NMR spectroscopy and relaxometry.

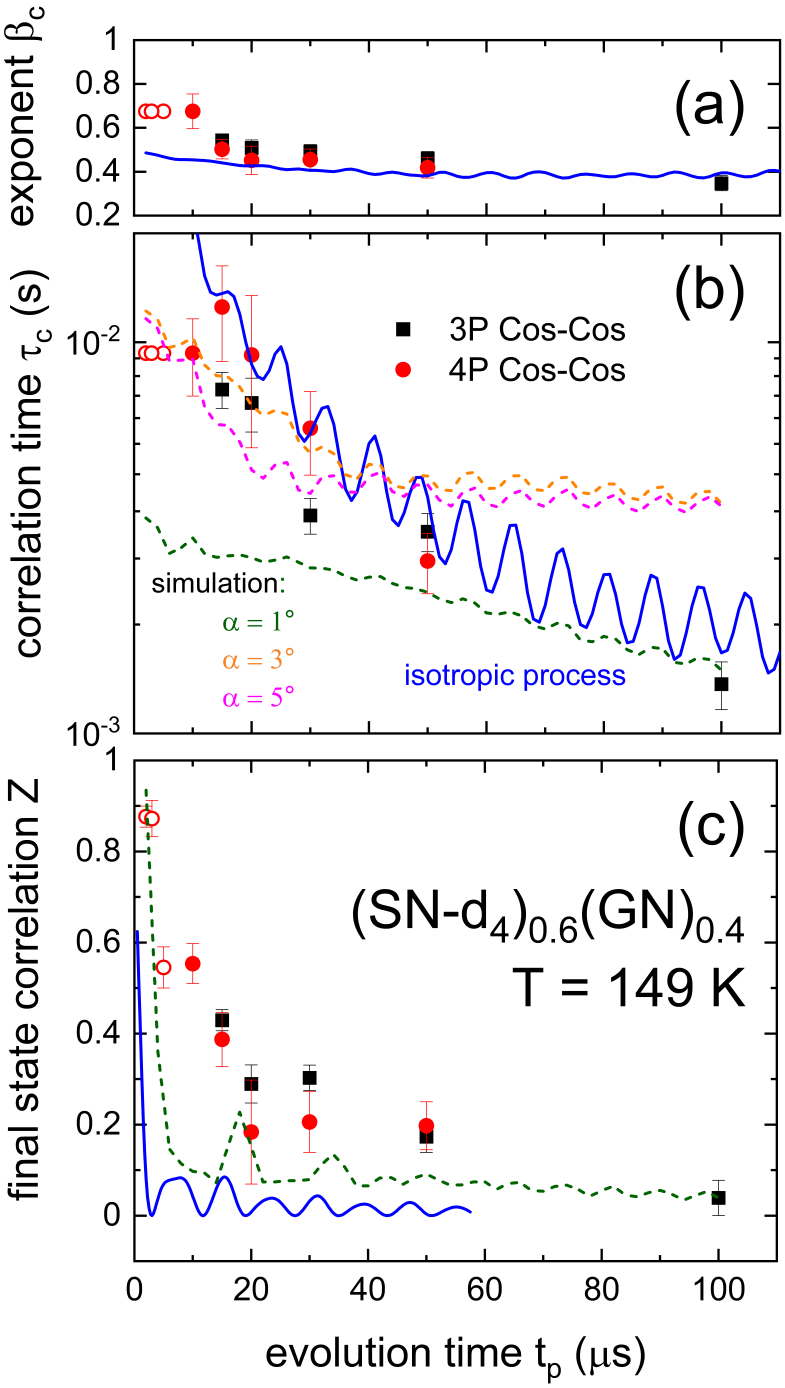

Figure 7.11: (b) Correlation times of $(SN\text{-}d_4)_{0.6}(GN)_{0.4}$ with (a) their respective Kohlrausch exponent and (c) The final correlation state as a function of evolution time t_p obtained by fitting the STE amplitudes with Eq. (4.39). The solid blue lines reflect a fully isotropic reorientation process as published in ref.[155]. The dashed lines reflect data obtained though simulation as detailed in Appendix A, where data for α = 3° and 5° were rescaled by a factor of 3.5. The black squares and red circles represent data obtained using three-pulse (3P) and four-pulse (4P) STE sequences, respectively. The unfilled red circles correspond to fits where the correlation time τ_c and the exponent β_c in Eq. (4.39) were set to 9.4 ms and 0.67, respectively.

7.1.2 Li-doped succinonitrile-glutaronitrile mixtures

Dielectric spectroscopy measurements

To investigate the impact of lithium doping on the reorientational motion of the dinitrile molecules, we conducted dielectric spectroscopy measurements on the $(SN\text{-}d_4)_{0.6}(GN)_{0.4}$ matrix doped with 1% $LiPF_6$, 5% $LiPF_6$, and 5% LiTFSI. The results for the 5% LiTFSI sample measured during the cooling run are presented in Figure 7.12. In frame (a), the frequency-dependent dielectric constants, ϵ', are shown while in frame (b), the dielectric losses, ϵ'', are displayed. Additionally, Figures 7.13(a) and (b) depict the real part of the conductivity, σ', and the imaginary part of the modulus, M'', respectively.

Examining the dielectric constant in Figure 7.12(a), it exhibits a steplike decrease from about 50 to 5 with decreasing temperature. The dielectric loss in frame (b), on the other hand, reveals the characteristic α relaxation peaks, previously discussed for the undoped sample. These peaks shift to lower frequencies with decreasing temperature in a similar manner to the undoped sample. Furthermore, no apparent decrease in the relaxation strength below 160 K was observed when compared to the pure $(SN\text{-}d_4)_{0.6}(GN)_{0.4}$ mixture.

Additionally, we employed the Cole-Davidson function to analyze the relaxation peaks of the dielectric loss. This was achieved using Eq. (5.7), where the α parameter was set to 1, and γ at 0.5 ± 0.1. The computed fits are included in Figure 7.12(b) and appear to fit only the right shoulders of the relaxation peaks. Indeed, the left shoulders exhibit an additional contribution that is not taken into account by the fits.

Moreover, Figure 7.13(a) illustrates the real part of the conductivity, σ'. Notably, distinct DC plateaus emerge, commencing at 10^{-4} S/cm for T = 231 K and progressively decreasing to 10^{-10} S/cm for T = 177 K. This reflects a substantial enhancement in the sample's conductivity, extending below conventional application temperatures. Concurrently, Figure 7.13(b) displays relaxation peaks in the imaginary part of the modulus, M''. These peaks shift towards lower frequencies as the temperature decreases. In contrast to the undoped sample, they exhibit a gradual reduction in their maxima. To fit these peaks, we use Eq. (5.7) with parameter α set to 1 and γ = 0.5 ± 0.1. The resulting fit lines are included in Figure 7.13(b).

To monitor the temperature-dependent evolution of the dielectric features in the doped sample, we present in Figure 7.14 the dielectric loss measured at 110 Hz, 12 kHz, and 1.3 MHz. Examining the data obtained at the lowest frequency (depicted by green triangles), a distinct transition occurs at T = 210 K, characterized by a significant discontinuity in $d\epsilon''/dT$. Notably, this transition is observed approximately 25 K below compared to the undoped mixture, which indicates a reduction in the phase transition temperature due to lithium doping.

Interestingly, the reduction in relaxation strength, not readily apparent in Figure 7.12(b), becomes evident in Figure 7.14. However, this reduction is relatively minor and heals around 180 K, in contrast to the undoped sample where it persists until 265 K when heating the

sample. At higher frequencies (depicted by blue and red triangles), the reduction becomes even less discernible.

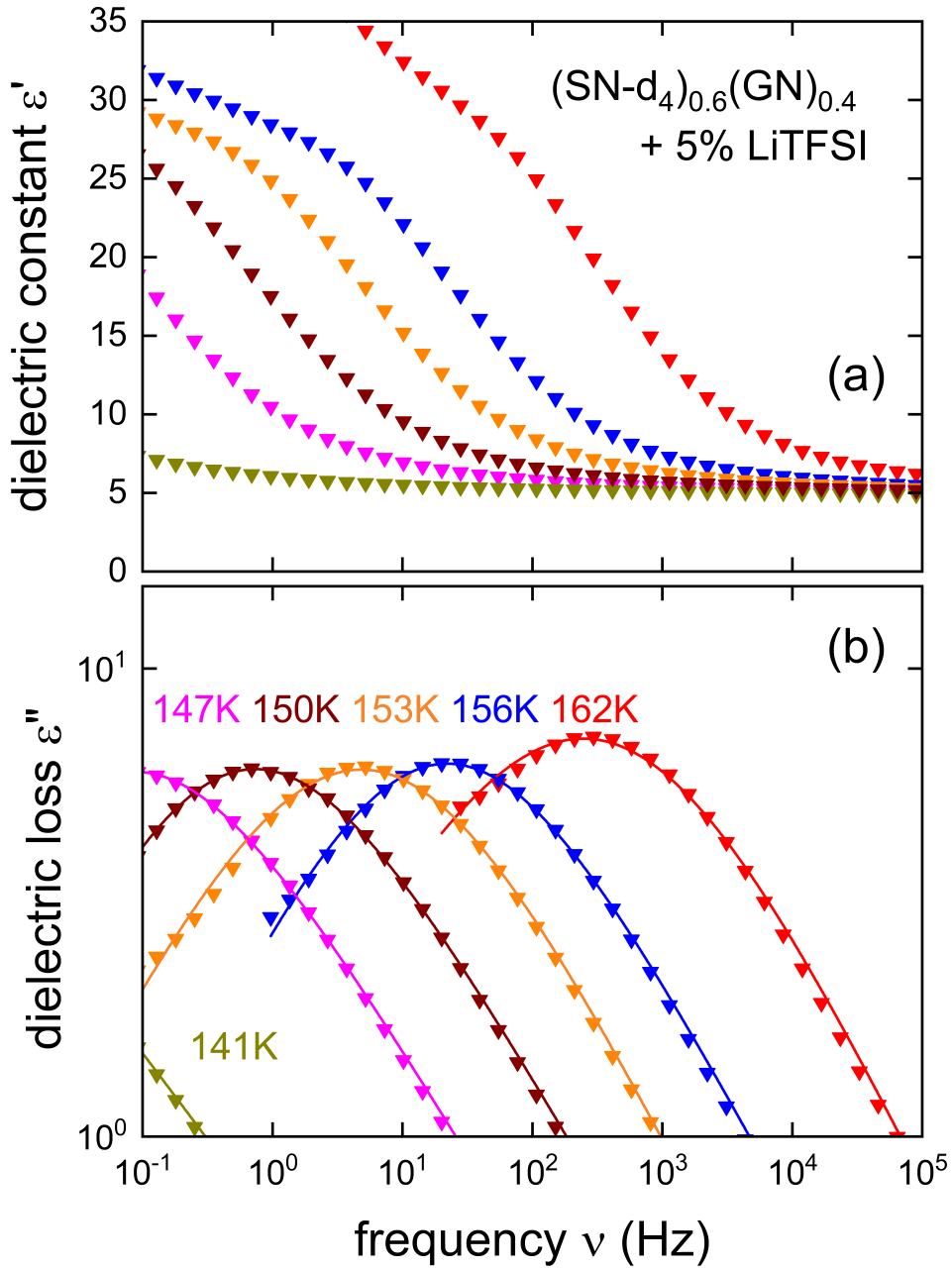

Figure 7.12: Frequency dependent measurements of (a) the real part and (b) the imaginary part of the complex dielectric permittivity of $(SN\text{-}d_4)_{0.6}(GN)_{0.4}$ doped with 5% LiTFSI. The graph was previously published in ref.[156]. Data was collected during cooling. Solid lines in frame (b) correspond to fits using a Cole-Davidson function, where the α parameter in Eq. (5.7) was set to 1 and $\gamma = 0.5 \pm 0.1$.

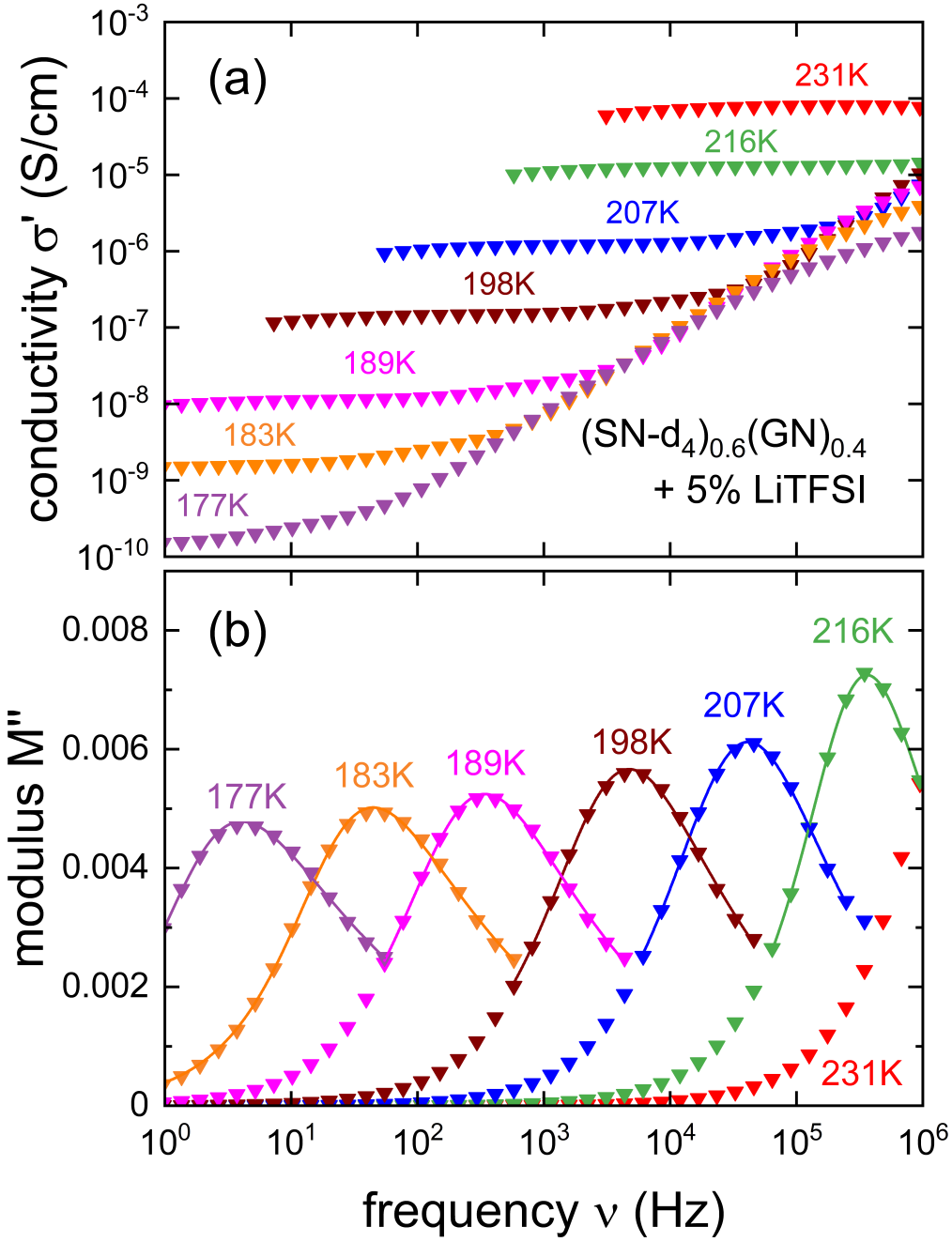

Figure 7.13: Frequency dependent measurements of (a) the real part and (b) the imaginary part of the complex dielectric permittivity of $SN_{0.6}GN_{0.4}$ doped with 5% LiTFSI. Frame (a) was previously published in ref.[156]. The electrode polarization contribution for σ' was neglected. Data was collected during cooling. Solid lines in frame (b) correspond to fits using Eq. (5.7) with parameter α set to 1 and $\gamma = 0.5 \pm 0.1$.

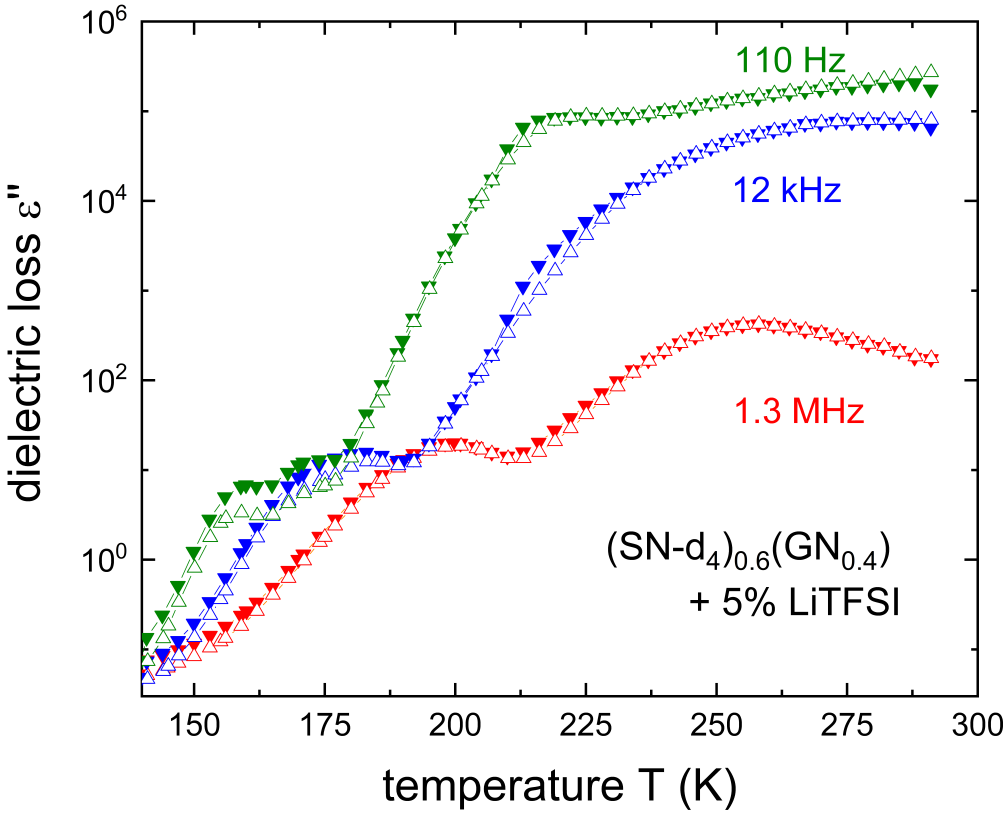

Figure 7.14: Temperature dependent dielectric loss of $(SN\text{-}d_4)_{0.6}(GN)_{0.4}$ doped with 5% LiTFSI measured at three different frequencies. Data was collected during cooling (solid triangles pointing down) or heating (open triangles pointing up). The lines are drawn to guide the eye.

To investigate the impact of doping with different lithium salts, we conducted dielectric spectroscopy measurements on two samples of $(SN\text{-}d_4)_{0.6}(GN)_{0.4}$ doped with 1% and 5% $LiPF_6$. The obtained values for the dielectric constant ϵ' and the dielectric loss ϵ'' for both the 1% and 5% $LiPF_6$ samples are depicted in Figures 7.15 and 7.16, respectively. Additionally, Figures 7.17 and 7.18 present the real part of the conductivity, σ', and the imaginary part of the modulus, M'' for both investigated samples.

A straightforward analysis of the data reveals several key findings: (i) Doping with $LiPF_6$ results in conductivity values comparable to those achieved with LiTFSI, despite LiTFSI's limited solubility in non-protonic solvents. (ii) At 1% $LiPF_6$ concentration, the dielectric characteristics of the SN-GN mixture remain nearly unchanged, with both ϵ' and ϵ'' exhibiting similar behaviors compared to the undoped mixture. (iii) At elevated lithium concentrations, $LiPF_6$ leads to a significant additional contribution to the low-frequency side of the dielectric loss peaks.

Moreover, our measurements on $SN_{0.6}GN_{0.4}$ doped with 1% $LiPF_6$ are in good agreement with the dielectric data reported for the same sample.[39] Specifically, we measured

comparable conductivity values and observed relaxation peaks within a similar temperature window. The data obtained from $SN_{0.6}GN_{0.4}$ doped with 1% and 5% $LiPF_6$ is subsequently analyzed and compared with all the investigated dinitrile samples in Section 7.1.4, focusing on conductivity and reorientational relaxation.

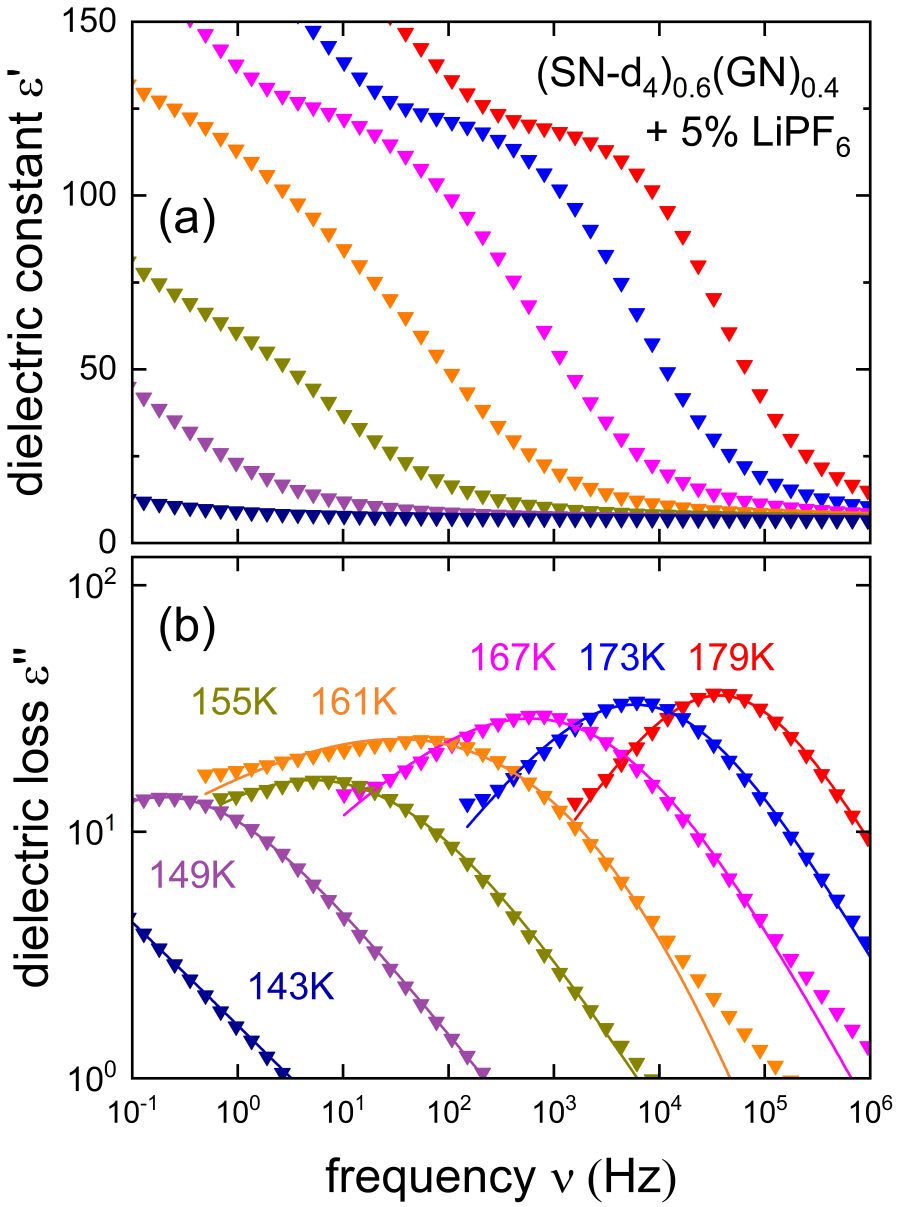

Figure 7.15: Frequency dependent measurements of (a) the real part and (b) the imaginary part of the complex dielectric permittivity of $(SN\text{-}d_4)_{0.6}(GN)_{0.4}$ doped with 5% $LiPF_6$. Solid lines in frame (b) correspond to fits using Eq. (5.7) with parameters $\alpha = 0.5 \pm 0.2$ and $\gamma = 0.9 \pm 0.1$. In contrast to the sample doped with 5% LiTFSI (see Figure 7.12), the dielectric loss peaks in frame (b) are not well fitted by a Cole-Davidson spectral distribution.

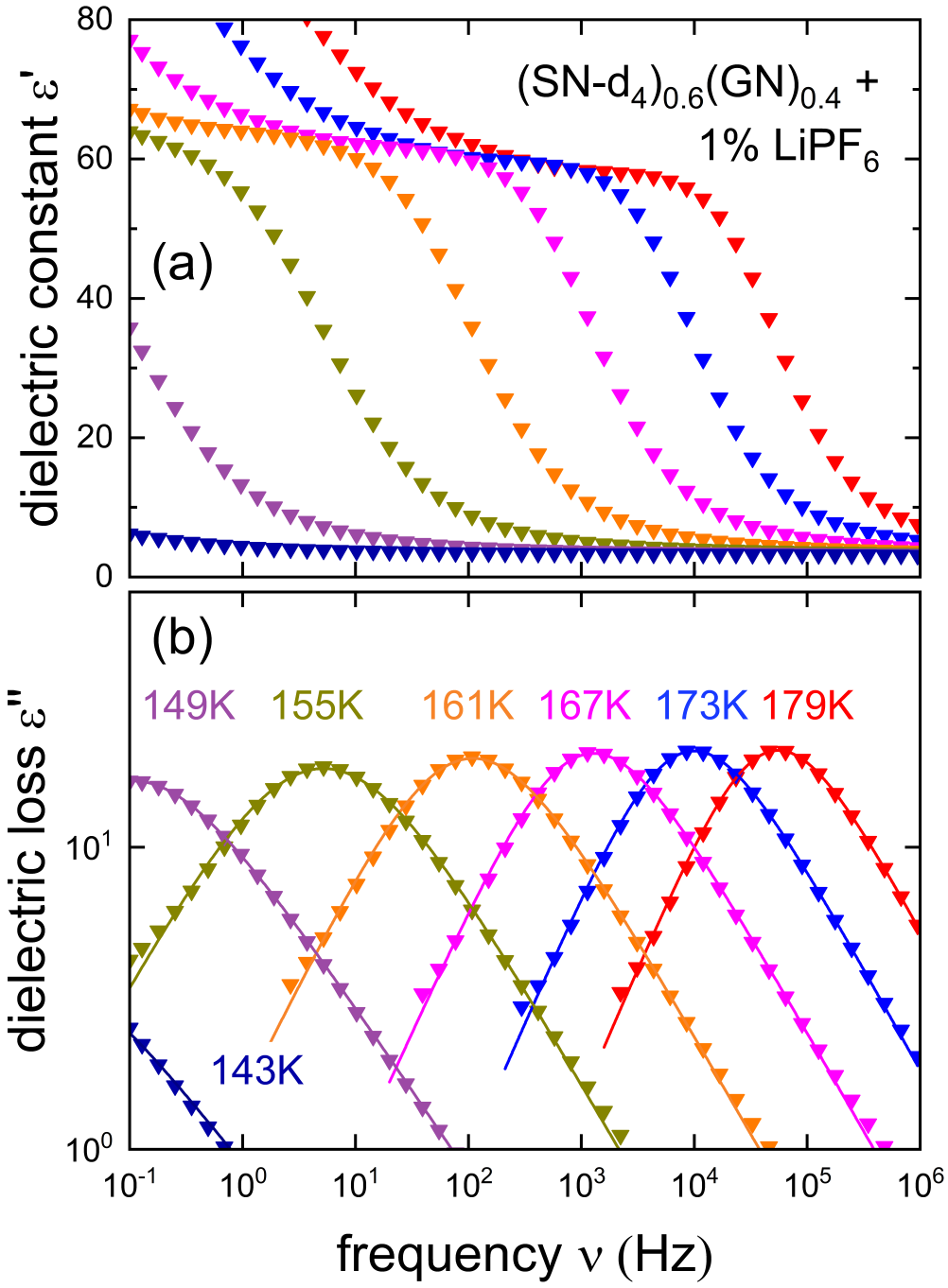

Figure 7.16: Frequency dependent measurements of (a) the real part and (b) the imaginary part of the complex dielectric permittivity of $(SN\text{-}d_4)_{0.6}(GN)_{0.4}$ doped with 1% $LiPF_6$. Solid lines in frame (b) correspond to fits using Eq. (5.7) with parameters $\alpha = 0.8 \pm 0.1$ and $\gamma = 0.7 \pm 0.1$. The dielectric data for the protonated mixture was previously reported by Geirhos *et al.*[39]. We conducted new measurements on the deuterated sample to enhance data comparability. Our measurements reveal similar dielectric properties.

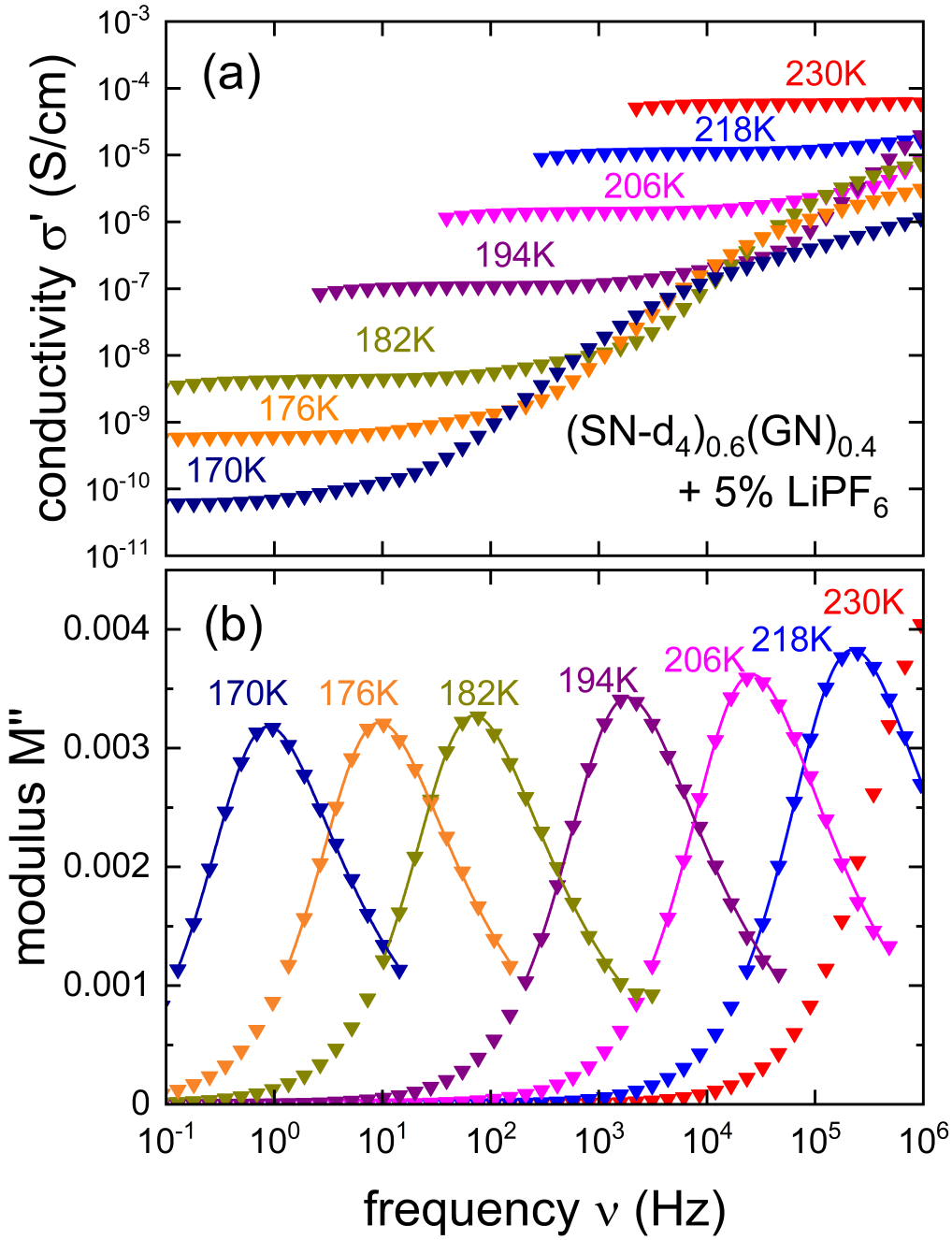

Figure 7.17: Frequency dependent measurements of (a) the real part of the conductivity σ' and (b) the imaginary part of the modulus M'' of $SN_{0.6}GN_{0.4}$ doped with 5% $LiPF_6$. Solid lines in frame (b) correspond to fits using Eq. (5.7) with parameters $\alpha = 0.9 \pm 0.1$ and $\gamma = 0.5 \pm 0.1$.

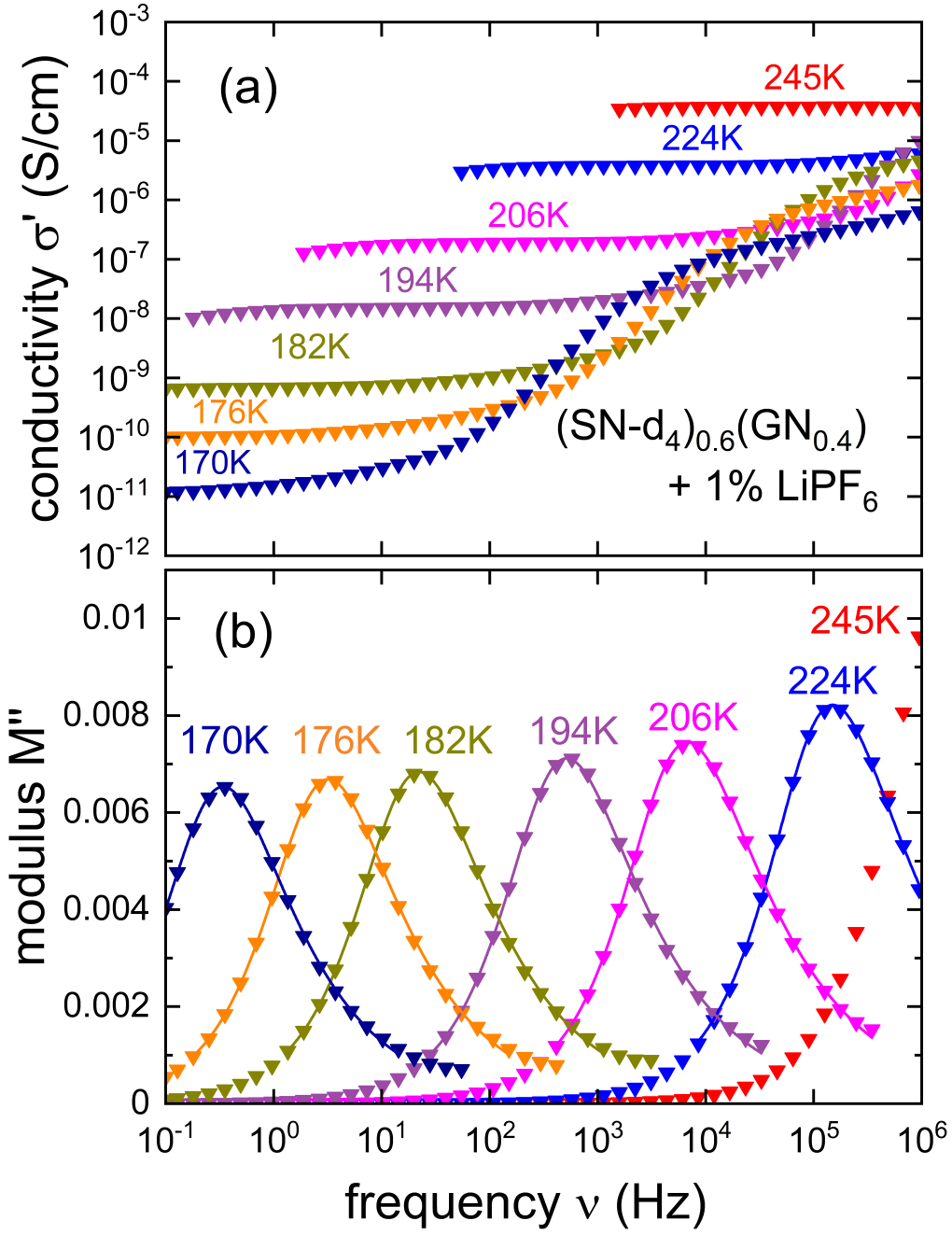

Figure 7.18: Frequency dependent measurements of (a) the real part of the conductivity σ' and (b) the imaginary part of the modulus M'' of $SN_{0.6}GN_{0.4}$ doped with 1% $LiPF_6$. The electrode polarization contribution for σ' was neglected. Solid lines in frame (b) correspond to fits using Eq. (5.7) with parameters $\alpha = 0.9 \pm 0.1$ and $\gamma = 0.5 \pm 0.1$.

Lithium spectroscopy

We utilized static ^{7}Li NMR spectroscopy to gain insights into the local environment of Li ions within the SN-GN matrix. Temperature-dependent ^{7}Li spectra for $(SN\text{-}d4)_{0.6}(GN)_{0.4}$ doped with 5% LiTFSI are illustrated in Figure 7.19.

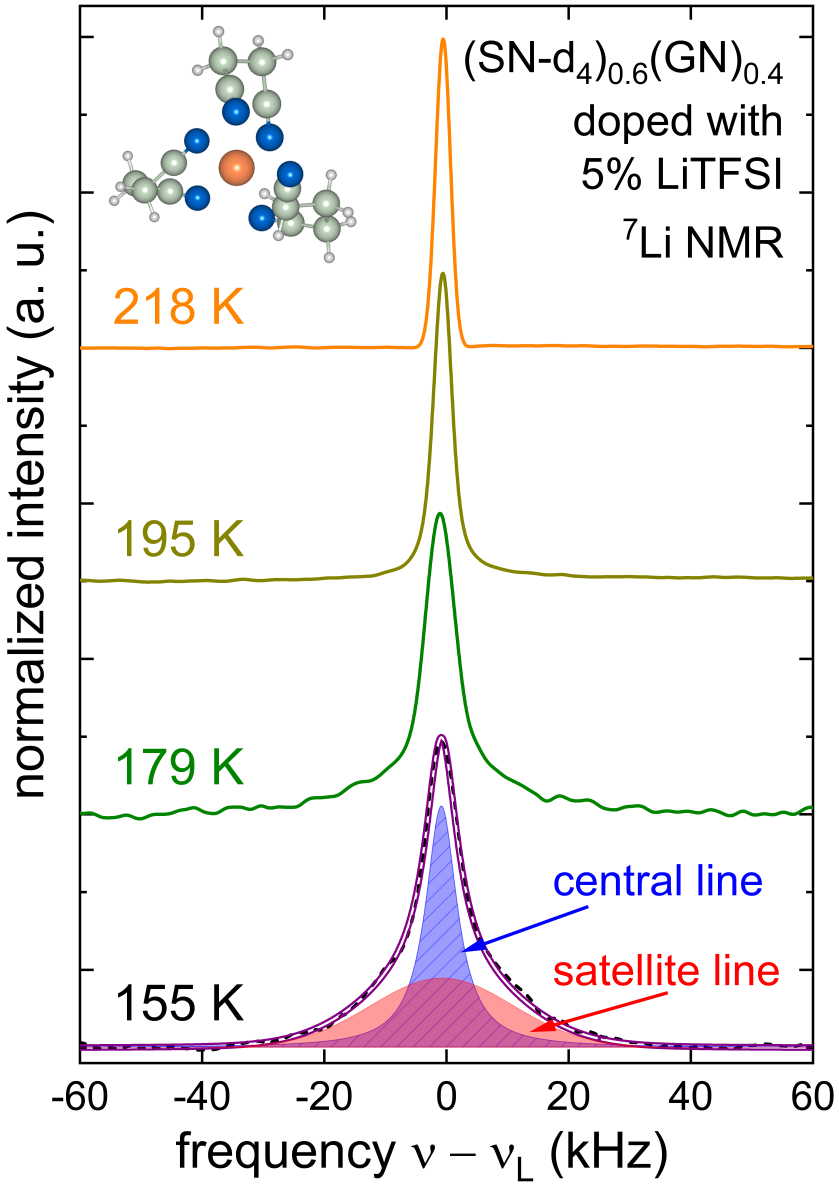

Figure 7.19: ^{7}Li solid echo spectra acquired at $\omega_L = 2\pi \times 116.9$ MHz (T < 195 K) and at $\omega_L = 2\pi \times 155.5$ MHz (T ≥ 195 K) for $SN_{0.6}GN_{0.4}$ doped with 5% LiTFSI. The spectrum recorded at T = 155 K (shown as dashed line) was fitted with a superposition of a Lorentzian central-transition contribution (filled dashed area) and a Gaussian satellite-transition contribution (filled area without dashes). The sum of the two is represented by the solid purple double line. This figure was previously published in ref.[156].

Upon closer examination of the spectra, a gradual broadening of the spectral lines is evident as the temperature decreases. Indeed, at higher temperatures, motional tumbling leads to averaging of anisotropic interactions and thus line narrowing. Conversely, at lower temperatures, these interactions are not averaged out, leading to broadening of the spectral line. In ^{7}Li NMR, the primary interactions responsible for line broadening are the electrical quadrupole interactions, with magnetic dipole-dipole interactions playing a lesser role.

Moreover, we conducted an analysis of the spectral components for the obtained spectrum at T = 155 K. This spectrum is characterized by a dominant Lorentzian line, accounting for 54% of the total intensity, and a Gaussian contribution, making up the remaining 46%. The full width at half maximum (FWHM) of the dipolarly broadened central-transition (-1/2 $\longleftrightarrow$ +1/2) line is $\Delta\nu_{1/2}$ = 6 kHz.

In contrast, the quadrupolarly broadened satellite spectrum exhibits a broader line shape with $\Delta\nu_{1/2}$ = 32 kHz. The broadening observed in the satellite spectrum implies a superposition of multiple NMR lines originating from distinct structural environments. In these environments, lithium ions experience quadrupolar interactions with varying strengths.

Furthermore, we plot in Figure 7.20 the line width of the measured solid echo spectra at different temperatures and use the following equation to extract the correlation time:[157, 158]

$$\tau_c(T) = \frac{1}{2\pi \cdot A \cdot \Delta\nu(T)} \tan\frac{\pi}{2}\frac{\Delta\nu^2(T)}{\Delta\nu_{RL}^2}. \tag{7.1}$$

Here, $\Delta\nu$(T) is the ^{7}Li central-transition line width, $\Delta\nu_{RL}$ its rigid-lattice limit (8 kHz), and A a fit parameter. The extracted correlation times are discussed in Section 7.1.4.

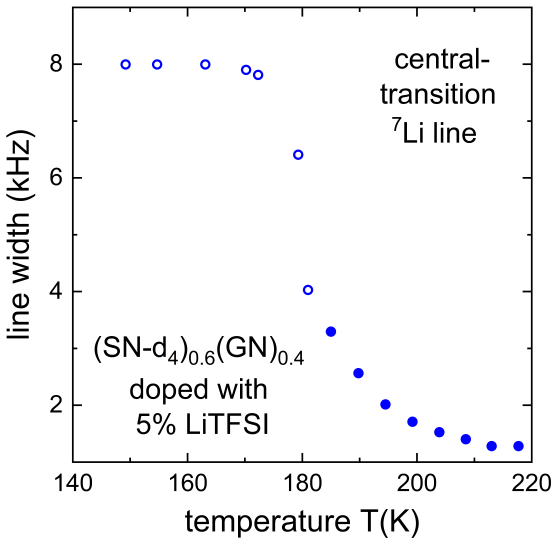

Figure 7.20: ^{7}Li central-transition line widths determined for $SN_{0.6}GN_{0.4}$ doped with 5% LiTFSI. This figure was previously published in ref.[156].

Deuterium and lithium relaxometry

Similar to the undoped sample, we utilized ^{2}H NMR relaxometry to examine the influence of lithium doping on the host matrix. Additionally, we employed ^{7}Li to investigate the dynamics of the mobile ions within the SN-GN matrix. The measured spin-lattice relaxation times, T_1, and spin-spin relaxation times, T_2, for ^{2}H and ^{7}Li in $(SN\text{-}d_4)_{0.6}(GN)_{0.4}$ doped with 5% LiTFSI are presented in Figure 7.21. For comparison, relaxation times obtained for the undoped matrix are also included.

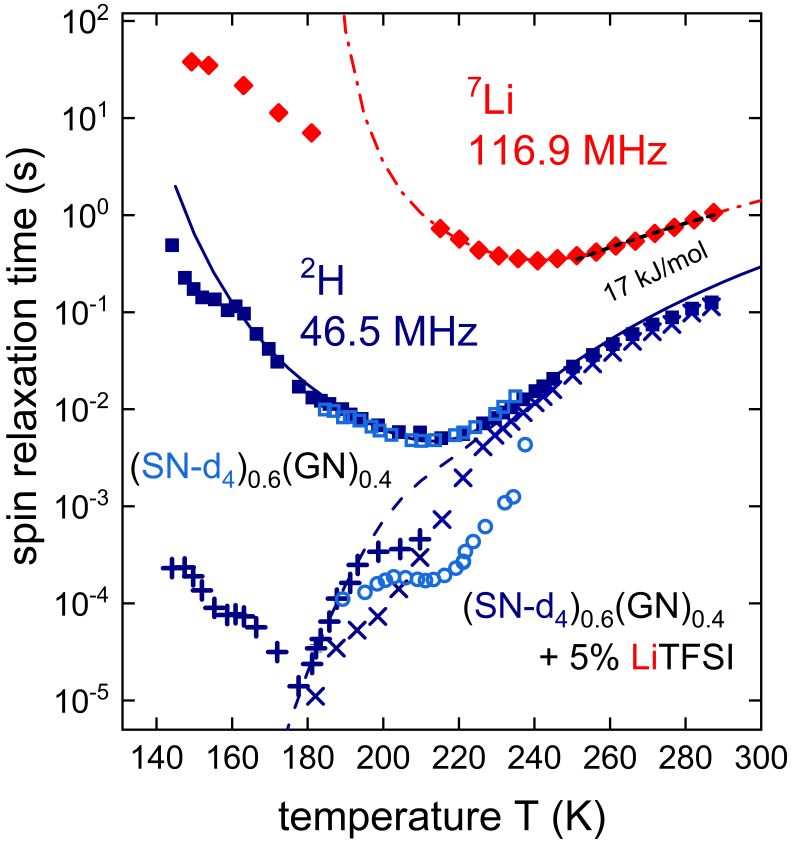

Figure 7.21: Temperature-dependent ^{2}H spin-lattice relaxation times (T_1, represented by full symbols) and spin-spin relaxation times (T_2) for $(SN\text{-}d_4)_{0.6}(GN)_{0.4}$ doped with 5% LiTFSI, as published in reference [156]. The T_2 measurements were conducted during cooling and using Hahn-echo (×, for temperatures below 180 K) and solid echo sequences (+, for temperatures up to 210 K). The solid blue and dashed blue lines depict fits based on Eq. (4.33) and Eq. (4.34), utilizing the spectral density provided by Eq. (4.28), and incorporating VFT fit parameters from the undoped sample. Deuterium T_1 and T_2 data for the undoped mixture are indicated by light blue squares and circles, respectively. The red diamonds represent ^{7}Li spin-lattice relaxation times for the doped mixture, with the dash-dotted red line calculated using Eq. (4.35) in a similar manner to the ^{2}H data. The black dashed line refers to an apparent energy barrier of 17 kJ/mol.

Furthermore, we computed the ^{2}H and ^{7}Li relaxation times using the same procedure and timescales calculated for the undoped sample shown in Figure 7.8: Eq. (4.33), Eq. (4.34) or Eq. (4.35) were employed in conjunction with the HN spectral density from Eq. (4.28). The resulting fit for ^{7}Li is included in Figure 7.21 as dashed red line, while those obtained for ^{2}H are shown as solid lines. The parameter γ of the HN spectral density was set to 0.24 for ^{7}Li and to 0.3 for ^{2}H.

Upon inspecting the deuterium data, similar features to those observed in the undoped matrix can be identified. A comparable discrepancy in T_1 and T_2 at high temperatures, as well as a significant drop in T_2 around 230 K are observed. Moreover, the quadrupolar anisotropy parameter is found to be equal to that obtained before doping, namely $2\pi\times$ 125 kHz. Additionally, a deviation of T_2 in the temperature range between 230 K and 195 K is observed. These observations imply a complete absence of change in the dynamics of the hosting matrix after the addition of 5% LiTFSI.

Turning to the ^{7}Li data and using the Arrhenius law, one can calculate the activation energy above the T_1 minimum to E_A = 17 kJ/mol. Moreover, the T_1 minimum provides a jump rate based on $\omega_L/k_{Li} = 0.62$,[159] resulting in $k_{Li} = 12\times10^{8}$ s^{-1} at 240 K. Additionally, by employing the Einstein-Smoluchowski equation:[117]

$$D_{Li} = \frac{a^2}{6\tau_{Li}}, \tag{7.2}$$

with a = 1.8 Å for the jump distance of the Li ions, one obtains a diffusion coefficient of $D_{Li} = 6\times10^{-12}$ m^{2}s^{-1}.

Diffusion and viscosimetry

In addition to conducting ^{2}H and ^{7}Li NMR spectroscopy and relaxometry investigations, we performed proton diffusion measurements using the experimental setup described in Section 4.4.4 on the $(SN\text{-}d_4)_{0.6}(GN)_{0.4}$ mixture, both before and after doping with 5% LiTFSI. Additionally, ^{7}Li diffusion measurements were carried out on the doped sample using the PFG experiment. These measurements allowed us to probe the dynamics of the hosting matrix from the perspective of the GN molecules and monitor the diffusion of the charge carrier in the liquid phase. To complement these diffusion studies, viscosimetry measurements were conducted to facilitate a comprehensive analysis of the diffusion results. Figure 7.22 illustrates the Arrhenius plot of the obtained ^{7}Li and ^{1}H diffusion coefficients, along with the temperature-dependent fluidity, i.e., the inverse zero-shear viscosity.

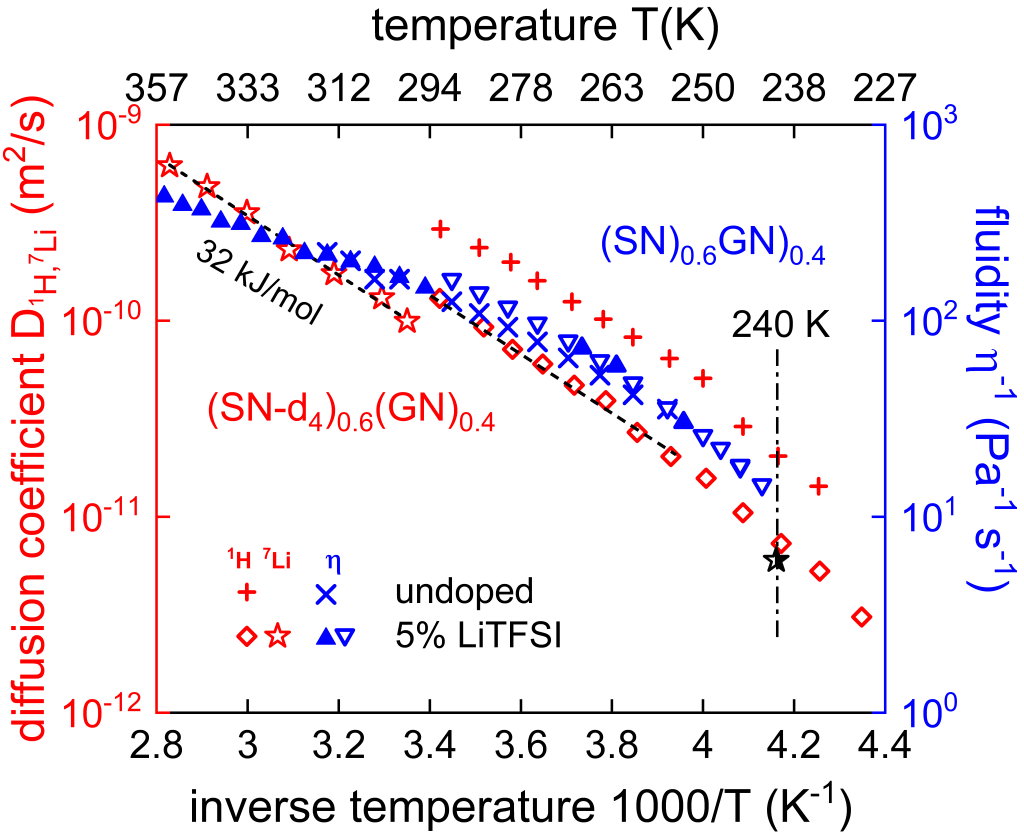

Figure 7.22: Temperature-dependent self-diffusion coefficients and fluidity (inverse zero-shear viscosity) of $(SN\text{-}d_4)_{0.6}(GN)_{0.4}$ before and after doping with 5% LiTFSI as published in ref.[156]. The unfilled red stars represent ^{7}Li PFG and the unfilled red diamonds ^{1}H SFG NMR measurements conducted during heating. The blue triangles indicate viscosity measurements during cooling (downward) and heating (upward). The half-filled black star represents the ^{7}Li diffusion coefficient derived from Eq. (7.2), with τ_{Li} obtained from the ^{7}Li T_1 minimum and a jump distance of 1.8 Å. ^{1}H self-diffusion coefficients and fluidities for the undoped mixture are represented by red (+) and blue (×) symbols, respectively. Dashed black lines signify apparent energy barriers of 32 kJ/mol, and the dash-dotted vertical line indicates the transition temperature from the undoped liquid to the plastically crystalline phase.

Upon initial examination of the proton diffusion coefficients within the undoped mixture, it becomes apparent that these values are considerably larger than those previously reported for pure SN based on NMR [150, 160, 161] or ^{14}C tracer diffusion experiments [162, 163]. Surprisingly, even below the melting temperature (T = 240 K), the GN molecules continue to undergo translational motion, and the diffusion remains unaffected. This observation was corroborated in a subsequent measurement run, performed after quenching the sample and

subsequent reheating. Additionally, upon comparison with the diffusion coefficients obtained for the doped mixtures, only a marginal change is evident upon Li-doping. Moreover, the fluidity data shows no significant deviation, as the data before and after doping exhibit the same trend.

In addition to our discussion of the diffusion data in Section 7.1.4, a more comprehensive analysis of the diffusion and viscometry data for the undoped sample has been detailed in reference [111], followed by a thorough comparison of the undoped and doped samples in reference [156].

7.1.3 Fumaronitrile addition to the glutaronitrile matrix

To assess the impact of increased conformational rigidity on the overall ionic conductivity of dinitrile electrolytes, we conducted dielectric spectroscopy investigations on the $FN_{0.2}GN_{0.8}$ matrix. This exploration involved both the undoped mixture and the mixture doped with 5% LiTFSI. The results obtained during cooling of the samples and represented by the real part of the electrical conductivity σ', the dielectric constant ϵ', and the dielectric loss ϵ'', are depicted in Figure 7.23 for the undoped sample and in Figure 7.24 for the doped sample. We also include in Figure 7.23 data obtained during heating of the undoped sample, shown as crosses.

At elevated temperatures, the DC plateau shown in Figure 7.23(a) emerges at approximately 10^{-5} S/cm, indicating significantly lower conductivities compared to the undoped SN-GN mixtures. Upon cooling and below 224 K, a phase transition occurs, leading to a sudden jump in the DC plateau. This characteristic is also noticeable in the dielectric constant and dielectric loss shown in Figures 7.23(b) and (c), respectively. Upon heating the sample and at temperatures above 242 K, the phase transition forementioned is healed.

Additionally, Figure 7.24(a) shows that the introduction of 5% LiTFSI results in a substantial increase in the overall conductivity, showcasing a DC plateau at 10^{-3} S/cm even at temperatures as low as 263 K. Furthermore, the phase transition observed in the undoped samples occurs at slightly lower temperatures, around 209 K.

To circumvent this phase transition, we conducted dielectric spectroscopy measurements on the doped sample after quenching (125 K/min) and subsequent heating. The results of this measurement run are illustrated in Figure 7.25. The DC plateau in Figure 7.25(a) appears at around 10^{-11} S/cm at T = 166 K and gradually increases with temperature, reaching 10^{-4} S/cm at T = 238 K. This latter value aligns well with the conductivity observed for the unquenched sample at similar temperatures, implying that the doped $GN_{0.8}FN_{0.2}$ can indeed be supercooled. Moreover, the dielectric constant ϵ', as depicted in Figure 7.25(b), is predominantly influenced by the conductivity contribution, with the previously mentioned step-like relaxation observed in dinitrile mixtures being scarcely discernible. This holds true for the dielectric loss ϵ'' illustrated in Figure 7.25(c) as well, where the relaxation peaks are not fully evident.

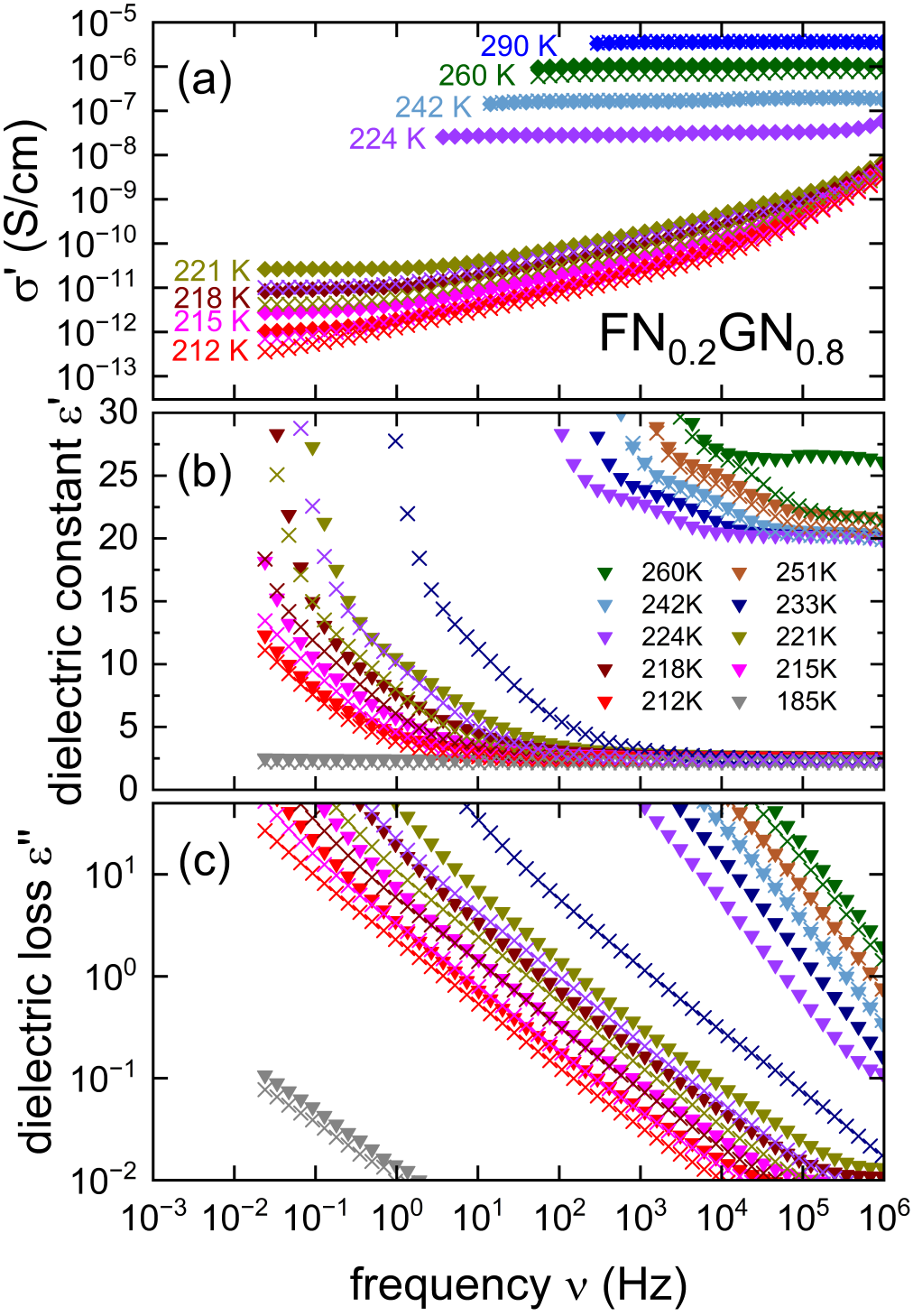

Figure 7.23: Frequency-dependent measurements of (a) the electrical conductivity, (b) the real part, and (c) the imaginary part of the complex permittivity of $FN_{0.2}GN_{0.8}$. Data in frame (a) affected by electrode polarization effects is not shown. Measurements were conducted during cooling (solid triangles) or heating (crosses).

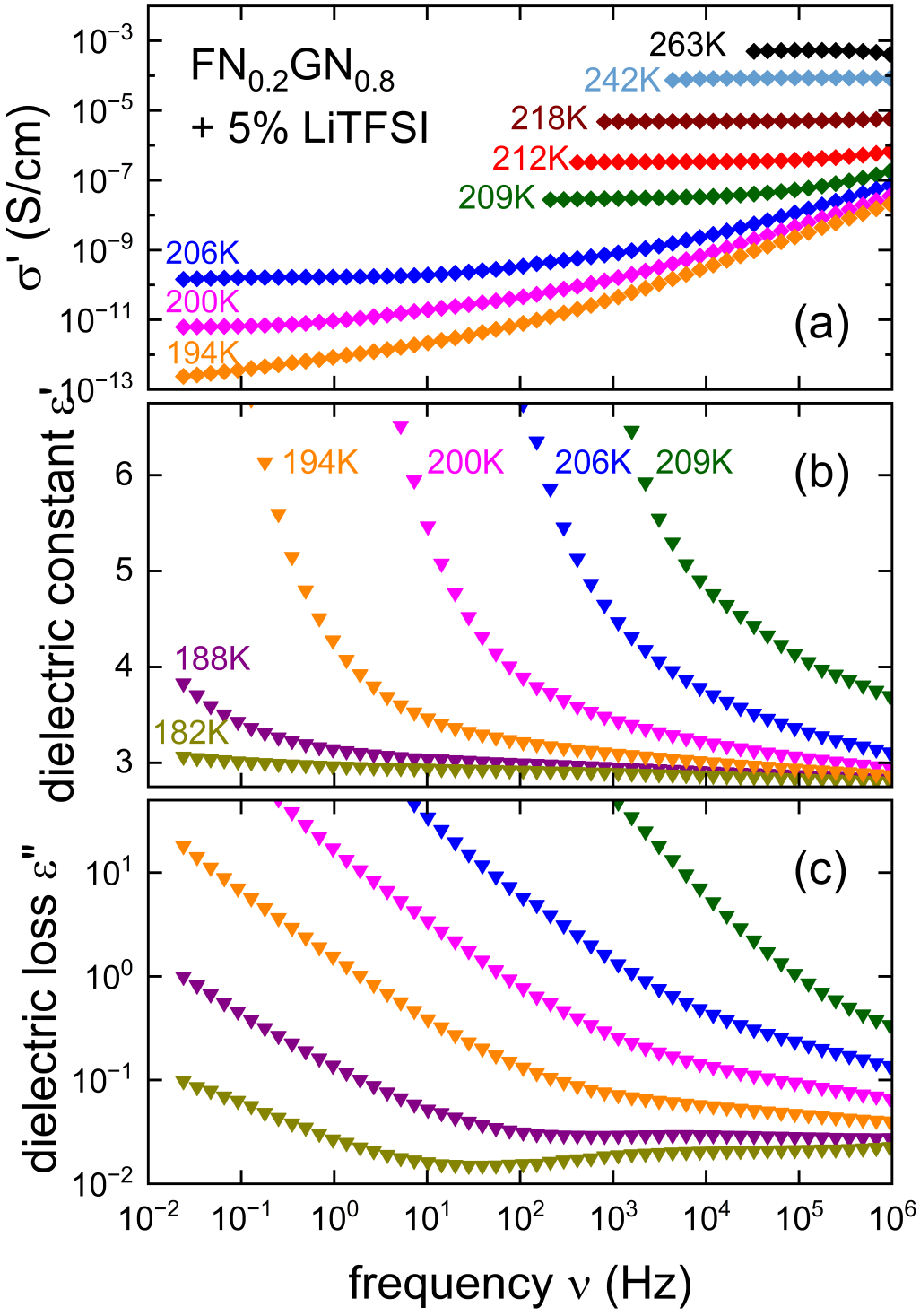

Figure 7.24: Frequency-dependent measurements of (a) the electrical conductivity, (b) the real part, and (c) the imaginary part of the complex permittivity of $FN_{0.2}GN_{0.8}$ doped with 5% LiTFSI. Data in frame (a) affected by electrode polarization effects is not shown. Measurements were conducted during cooling. Relaxation peaks in frame (c) are not discernible, even with the use of Eq. (5.10), hence ϵ''_{der} has been excluded.

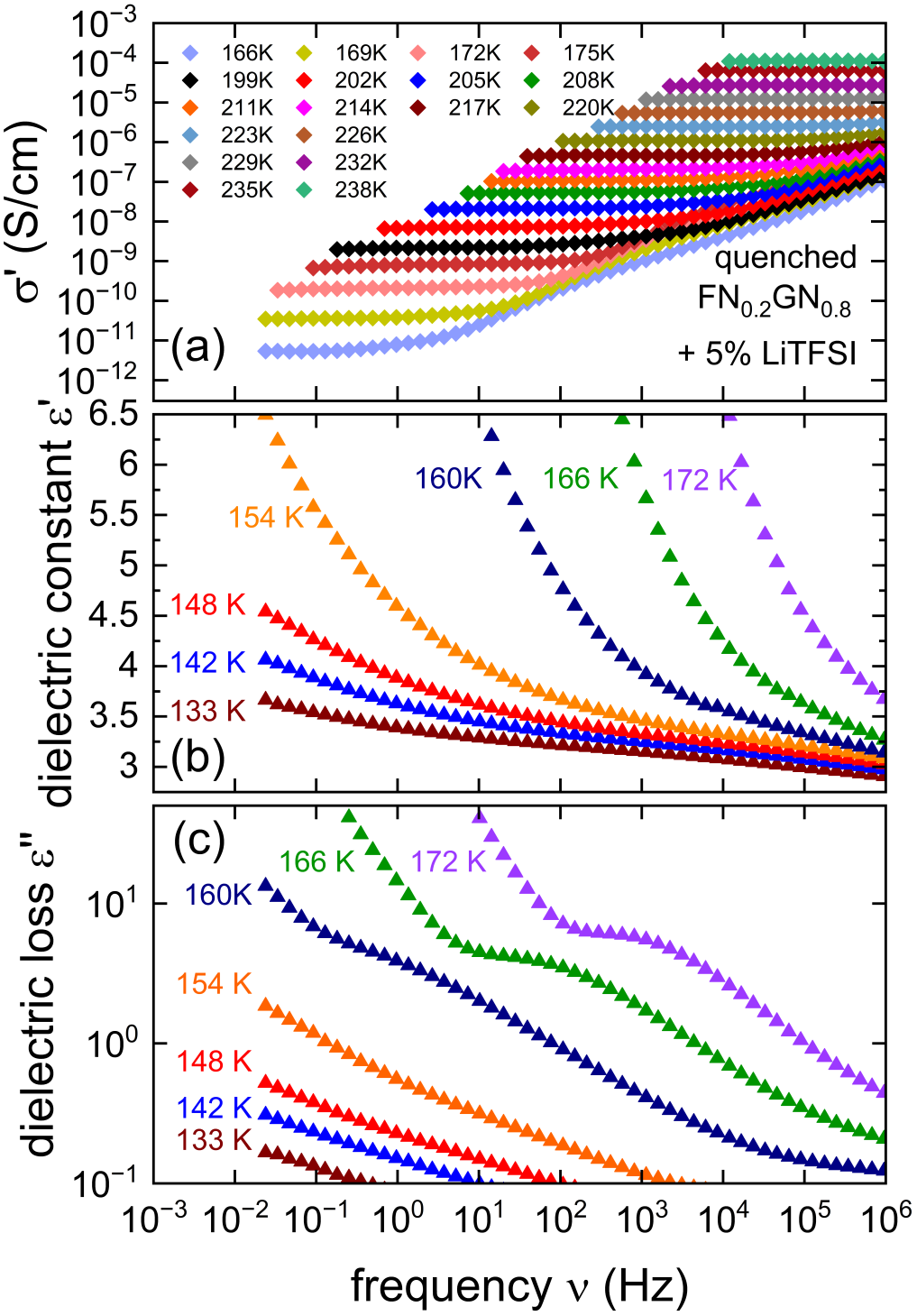

Figure 7.25: Frequency-dependent measurements of (a) the electrical conductivity, (b) the real part, and (c) the imaginary part of the complex permittivity of $FN_{0.2}GN_{0.8}$ doped with 5% LiTFSI. These measurements were conducted during heating after quenching the sample. Data in frame (a) affected by electrode polarization effects is not shown. Measurements were conducted during cooling.

7.1.4 Discussion of dynamics and conductivity

We focus in this section on elucidating potential correlations between ionic conductivity and reorientational dynamics of the hosting ratios. To begin our discussion, we examine the $SN_{0.6}GN_{0.4}$ mixture before considering other matrices. Thus, we compare the temperature-dependent ionic conductivities in $SN_{0.6}GN_{0.4}$ before and after doping with $LiPF_6$ and LiTFSI, as illustrated in Figure 7.26(a). These conductivity values are derived from the DC plateau observed in the real part of the conductivity σ'. Additionally, we include data for pure SN and SN doped with 1% $LiPF_6$ reported in ref. [18] and ref. [153], respectively.

Furthermore, in Figure 7.26(b), we show the reorientational relaxation times obtained by fitting the relaxation peaks in the dielectric loss using Eq. (5.8) in conjuction with Eq. (5.7). Correlation times from ^{2}H and ^{7}Li NMR are also presented (refer to the Figure 7.26's caption for more details).

Comparing the conductivity values of pure SN with the $(SN\text{-}d_4)_{0.6}(GN)_{0.4}$ mixture confirms a significant enhancement in ionic conductivity upon the addition of 40% GN molecules. This enhancement appears more pronounced than that achieved by simply introducing Li ions in pure SN. Additionally, Li-doping of the $(SN\text{-}d_4)_{0.6}(GN)_{0.4}$ mixture further increases the overall conductivity, with no apparent difference observed when doping with 5% $LiPF_6$ or 5% LiTFSI.

Utilizing Eq. (3.4), we can convert the Li NMR diffusion coefficients into conductivity terms. For simplicity, we assume the tracer diffusion coefficient and the charge diffusion coefficient as equal, i.e., $H_R = 1$ in Eq. (3.6). Additionally, we take 2.4×10^{24} m^{-3} as the charge carrier density for $(SN\text{-}d_4)_{0.6}(GN)_{0.4}$ doped with 5% LiTFSI and use the elementary charge of the Li^+ ion. Furthermore, we convert viscosity data into diffusion coefficients using Eq. (3.7) and derive conductivity values in a manner similar to the ^{7}Li NMR diffusion coefficients. Here, we use the effective hydrodynamic radius $r_H = 1.0$ Å and $n = 8 \times 10^{23}$ m^{-3} for the charge-carrier number density of the undoped $(SN\text{-}d_4)_{0.6}(GN)_{0.4}$ mixture.

The conductivity arising from both the translational movement of Li ions and the displacement of the nitrile molecules exhibits a notable alignment with the conductivity measured through dielectric spectroscopy. These consistent findings reflect a closely correlated motion between Li ions and dinitrile molecules in the liquid phase. Moreover, by examining Figure 7.26(b) one can establish that the introduction of a small percentage of Li ions does not exert a substantial impact on the matrix dynamics. Indeed, all of the investigated samples as well as pure and doped SN exhibit the same matrix dynamics. Additionally, the correlation observed in the liquid state is corroborated in the plastic crystalline phase by the correlation times extracted from the ^{7}Li NMR spectra, which corresponds to the dynamics described in Figure 7.26(b). The only deviation from these dynamics is observed in the correlation times τ_c obtained through deuterium stimulated echo experiments for the undoped sample $(SN\text{-}d_4)_{0.6}(GN)_{0.4}$, where a slight discrepancy is noted. This discrepancy could potentially be attributed to variations introduced during the fitting procedure.

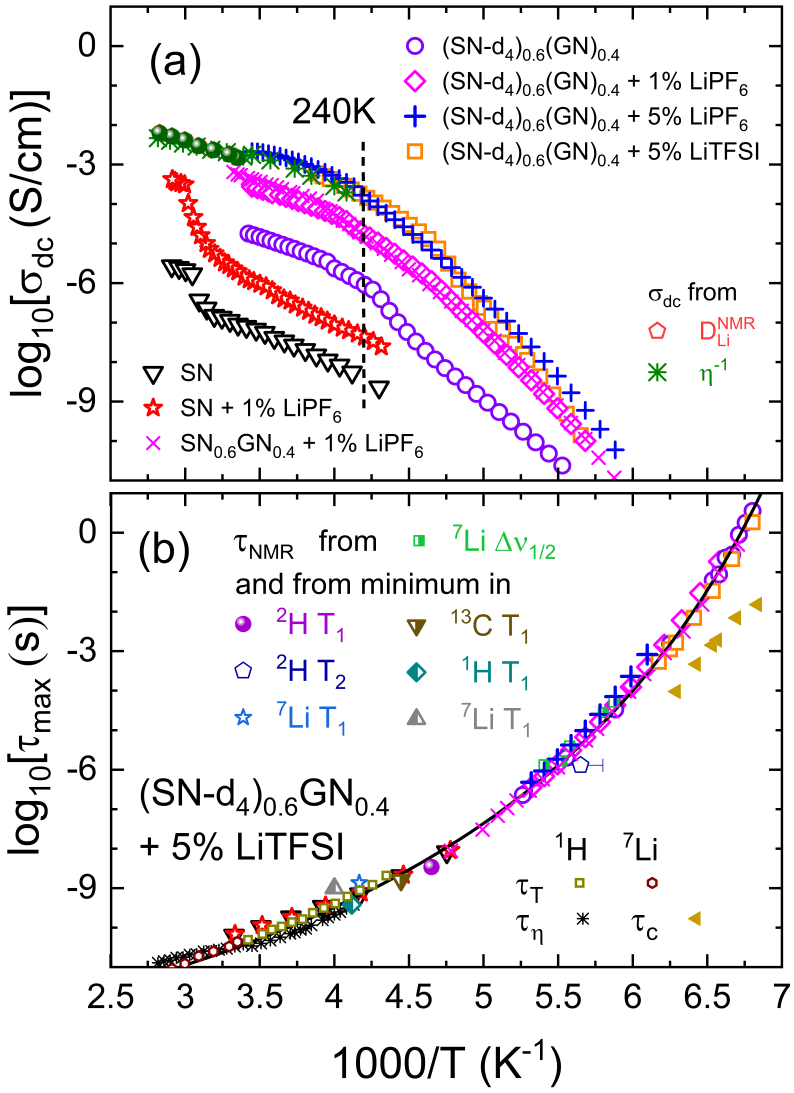

Figure 7.26: Arrhenius plot of (a) the temperature-dependent ionic conductivity and (b) correlation time τ of $(SN\text{-}d_4)_{0.6}(GN)_{0.4}$ mixtures doped with 1% $LiPF_6$, 5% $LiPF_6$, and 5% LiTFSI, as published in ref. [156]. Data in frames (a) and (b) for pure SN,[18] SN doped with 1% $LiPF_6$,[153] and another dataset of $SN_{0.6}GN_{0.4}$ doped with 1% $LiPF_6$ [39] are from existing literature. Frame (a) also incorporates the conductivities of $(SN\text{-}d_4)_{0.6}(GN)_{0.4}$ doped with 5% LiTFSI, obtained after conversion of Li diffusion coefficients and fluidity data. The vertical dotted line marks the transition temperature (T = 240 K) of undoped $SN_{0.6}GN_{0.4}$. Frame (b) includes correlation times from ^2H and ^7Li relaxometry of $(SN\text{-}d_4)_{0.6}(GN)_{0.4}$ doped with 5% LiTFSI, as well as from ^7Li line widths. NMR time scales from Davidowski *et al.*[35] for fully protonated samples are denoted as half-filled symbols. A VFT fit for undoped $(SN\text{-}d_4)_{0.6}(GN)_{0.4}$ is represented by the solid line. Shear relaxation times τ_η are determined from the Maxwell relation $\tau_\eta = \eta/G_\infty$, with G_∞ set to 0.18 GPa. Translational times τ_T are derived by converting the ^1H NMR diffusion coefficients, using $\tau_T = r_H^2/9D$. τ_c are correlation times determined using 3P cos-cos deuterium stimulated echo experiment with t_p = 15 μs.

The similarities in the time scales of the translational motion of the Li ion and the reorientational motion of the dinitrile molecules as indicated by Figure 7.26(b) favor a paddle-wheel mechanism over a revolving door mechanism. Specifically, the latter implies only a similar temperature dependence of the respective timescales but not necessarily identical values. Moreover, the paddle-wheel mechanism requires a prerequisite of sufficient free volume for the dinitrile molecules to rotate freely. Considering the unchanged matrix dynamics before and after doping, this condition appears to be consistently fulfilled at low concentrations of Li doping.

We now consider the conductivity of various SN-GN mixtures prior to doping and present a plot of σ_{DC} for $SN_{1-x}GN_x$ in Figure 7.27, where x ranges from 0 to 0.80. Data for $x = 0$, 0.07 and 0.11 were sourced from ref. [34], while that for $SN_{0.85}GN_{0.15}$ was obtained from ref. [33]. Additionally, we incorporate our data for $FN_{0.20}GN_{0.80}$. Furthermore, to facilitate comparison with the previously discussed doped samples, we include conductivity data for $(SN\text{-}d_4)_{0.6}(GN)_{0.4}$ and $FN_{0.20}GN_{0.80}$ (also postsample quenching) doped with 5% LiTFSI.

The positive impact of incorporating GN molecules on the overall conductivity is now evident. Indeed, the gradual addition of GN molecules results in a progressive increase in the conductivity of the SN-GN mixture. Although data for $SN_{0.20}GN_{0.80}$ is only available at low temperatures, the trend suggests a conductivity maximum for $x = 0.40$, as previously reported in the literature.[39]

Moreover, Figure 7.27 serves as a good indicator for tracking the evolution of phase transitions in SN upon the addition of GN. The transition temperature from the liquid to the plastic crystalline phase gradually decreases with increasing GN concentration. Additionally, for low GN concentrations, the transition temperature from the plastic crystalline phase to the fully ordered phase is significantly reduced. These observations align well with the reported phase diagram of the SN-GN mixture, see Section2.1.

Furthermore, the conductivity of the undoped $FN_{0.20}GN_{0.80}$ aligns well with the trend observed for the conductivity enhancement resulting from GN addition. Specifically, the conductivity values fall between those of $SN_{0.15}GN_{0.85}$ and $SN_{0.60}GN_{0.40}$, implying that the effect of GN addition may extend to FN as well. Upon Li doping and for temperatures greater than 235 K, the sample exhibits an ionic conductivity almost as high as that of the doped $SN_{0.60}GN_{0.40}$, although no plastically crystalline phase is known for this binary mixture. Additionally, the successful supercooling of the $FN_{0.20}GN_{0.80}$ doped with 5% LiTFSI is evident; conductivity data acquired after quenching and shown as blue crosses (×) in Figure 7.28 align well with the conductivities measured for the unquenched sample.

Finally, by taking into account the findings made apparent by Figure 7.28 in the paddle-wheel interpretation, the introduction of GN does not negatively impact the free volume; instead, it increases it. This increase enhances the efficiency of charge transport by providing more space for Li ion migration. Consequently, the charge transport efficiency is improved, thereby positively effecting the overall conductivity. A more in-depth exploration of the

observations and arguments supporting the paddle-wheel mechanism is provided in Paper [156].

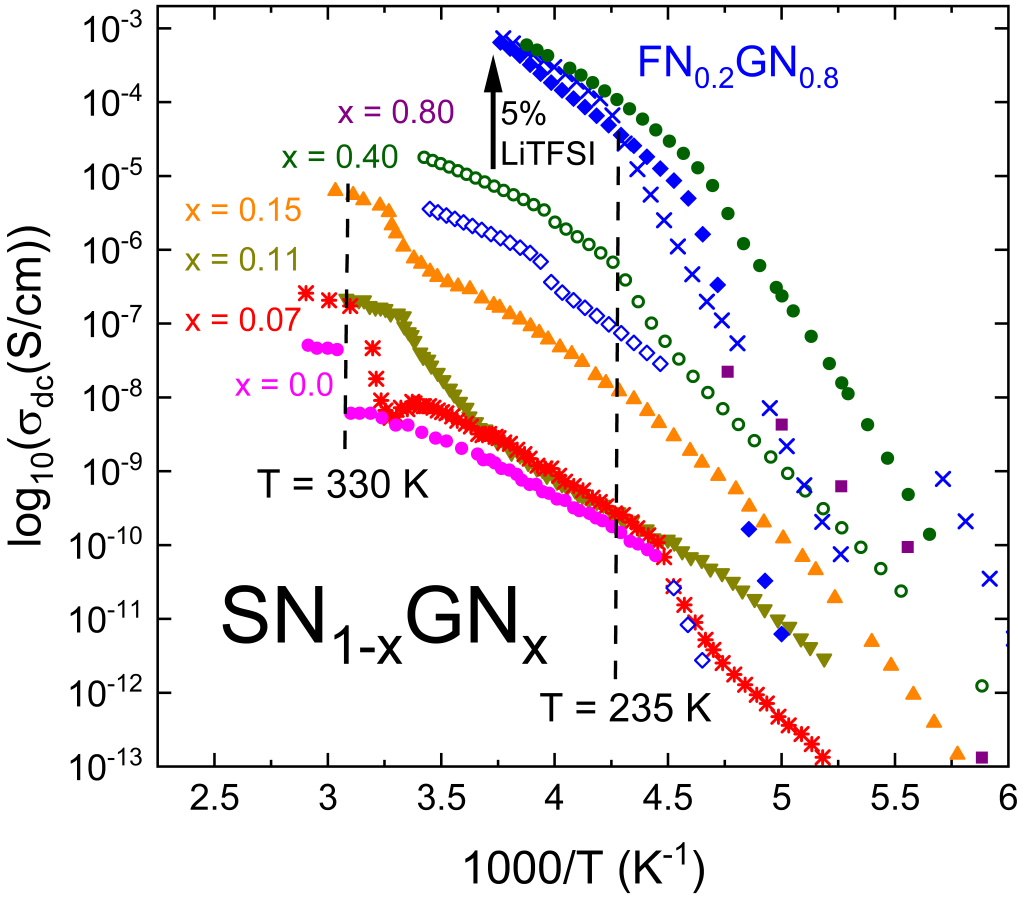

Figure 7.27: Arrhenius plot of the temperature-dependent conductivity of various SN-GN admixtures. Data for SN, $SN_{0.93}GN_{0.07}$ and $SN_{0.89}GN_{0.11}$ were sourced from ref. [34], while that for $SN_{0.85}GN_{0.15}$ was obtained from ref. [33]. The blue symbols denote $FN_{0.2}GN_{0.8}$ admixtures. Filled green circles (•) and filled blue diamonds (◊) represent samples doped with 5% LiTFSI. Crosses (×) indicate data acquired after quenching. The dashed lines highlight temperatures at which pure SN undergoes phase transitions (refer to Section2.1).

In addition to our investigation of the dinitrile samples from a matrix perspective, we look into the implications of varying the concentration of the charge carrier. To do so, we analyze the Walden plot, which represents the logarithmic relationship between viscosity and molar conductivity, for GN doped with LiTFSI concentrations ranging from 1% to 25%. Figure 7.28 illustrates the resulting graph. The data pertaining to the doped GN samples were collected within the framework of *Tobias Schwan*'s master thesis [164] and were previously published in ref.[165]. Additionally, we incorporate data for $SN_{0.6}GN_{0.4}$ doped with 5% LiTFSI into our analysis. The plot also includes supplementary data from various mono- and

dinitrile systems reported in the literature, as detailed in the figure's caption. Moreover, we utilize the fractional Walden law, $\Lambda\eta^{\lambda}$ = const, with $\lambda = -0.88$, to describe deviations from ideal behavior (depicted by the dashed line in Figure 7.28).

Although the Walden plot incorporates viscosity and molar conductivity, with the former reflecting the matrix's dynamics and the latter reflecting that of the charge carrier, the Walden representation appears to be relatively unaffected by the intricate interplay between hosting matrix and Li ions. Nonetheless, it indicates that all the analyzed samples fall under the category of "good" ionic liquids, regardless of their specific chemical composition. All data considered adhere to the fundamental principles of the Walden law, as demonstrated in Figure 7.28. For further details concerning this observation, the reader is invited to consult our publication on the subject matter.[165]

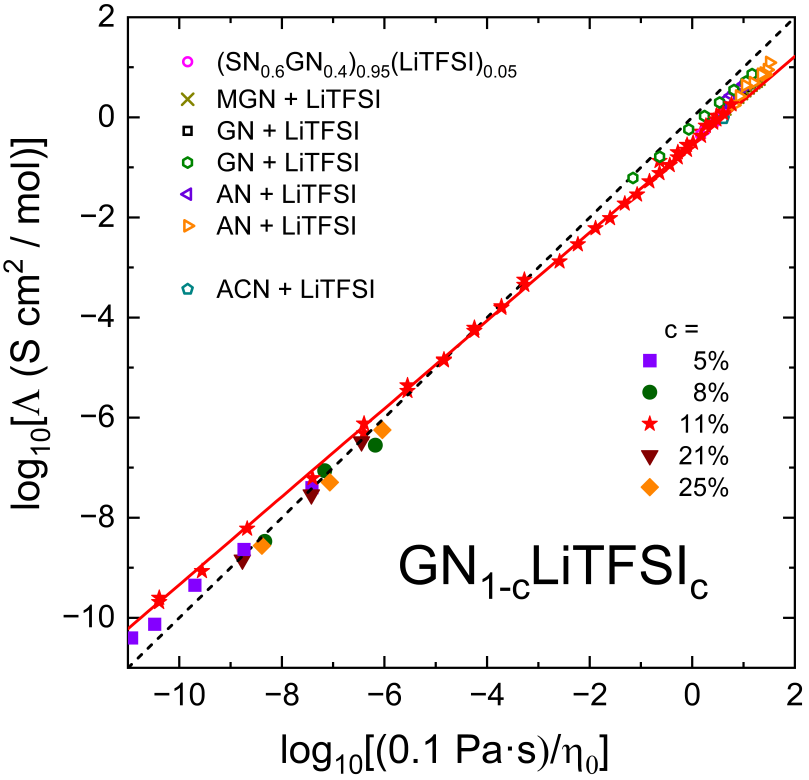

Figure 7.28: Walden plot illustrating the conductivity behavior of dinitriles doped with varying molar fractions of LiTFSI, as published in ref.[165]. The dashed black line with a slope of 1.0, represents the "ideal" conductive behavior of a 0.01 M KCl aqueous solution. The solid red line represents a fractional Walden law, $\Lambda \propto \eta_0^{-0.88}$. The plot includes data reported in the literature for GN (□) and 2-methylglutaronitrile (MGN, ×), both doped with 1 M LiTFSI,[28] for GN (⬡)[42] and adiponitrile (AN, ◁[25] and ▷[23]), both doped with several LiTFSI concentrations, and for acetonitrile (ACN) doped with LiTFSI at a molar ratio of 3:1 (⬠).[166]

7.2 Cycloalcohol mixtures

7.2.1 Neat and doped cycloalcohol binaries

Dielectric spectroscopy measurements

To investigate whether the correlation between ionic conductivity and reorientational dynamics, as previously discussed in Section 7.1.4 for $SN_{0.6}GN_{0.4}$, can also be observed in other plastic crystals such as $HEX_{0.6}OCT_{0.4}$, we conducted dielectric spectroscopy investigations on a serie of $HEX_{0.6}OCT_{0.4}$ samples, both before and after doping with LiTFSI concentrations ranging from 1% to 20%.

HEX-OCT mixtures were previously investigated by Reuter *et. al.*[80], who detected through differential scanning calorimetry (DSC) the existence of a plastic crystalline phase for all investigated samples. The authors also revealed the existence of a revolving-door mechanism in doped HEX-OCT mixtures. Interestingly, this dynamic coupling between the reorientational dynamics of the cycloalcohols and the charge carrier in doped HEX-OCT does not seem to be strongly dependent on the mixing ratio, as observed in SN-GN mixtures.[80]

Figures 7.29(a) and (b) show the frequency-dependent dielectric constants, ϵ', and dielectric losses, ϵ'', respectively, for the undoped $HEX_{0.6}OCT_{0.4}$ mixture measured during cooling. We opted for this particular ratio to maintain consistency with the SN-GN mixture, given the minor impact of mixing ratio variations on ionic conductivity and reorientational motion in the cycloalcohol mixture. Additionally, the selection of 60% HEX-d11 is supported by the availability of relevant dielectric spectroscopy data and its suitability for deuterium NMR investigations.

Similar to the dinitrile mixture, we observe a step-like increase in ϵ' with decreasing temperature accompanied by well-defined relaxation peaks in ϵ'' within the temperature range of 251 to 167 K. These relaxation peaks remain constant in strength and shift to lower frequencies with decreasing temperature, reflecting the reorientational behavior of the HEX and OCT molecules. Notably, the increase observed in the dielectric constant ϵ' upon cooling is much lower than that observed for $(SN\text{-}d_4)_{0.6}(GN)_{0.4}$. Furthermore, ϵ_∞ is approximately 1.5, which is lower than the reported values of 2.5 for pure HEX or pure OCT.[80, 83, 167] Such a discrepancy may be attributed to potential inaccuracies in the calibration process of the dielectric cell.

In analogy to our analysis of the SN-GN mixtures, we use Eq. (5.7) to fit the relaxation peaks and Eq. (5.8) to extract the associated relaxation time constants. The resulting fits are included as solid lines in Figure 7.29(b) and the extracted reorientational relaxation times are discussed in Section 7.2.3, below.

For convenience, we confine our description of the raw dielectric spectroscopy data pertaining to the doped samples to two mixtures: $HEX_{0.6}OCT_{0.4}$ doped with 1% LiTFSI and

5% LiTFSI. The latter will also undergo NMR investigation. Dielectric spectroscopy data for the remaining samples, i.e., $HEX_{0.6}OCT_{0.4}$ doped with 3%, 8%, 10%, 15%, and 20% LiTFSI, are presented in Appendix B. Their characteristic time constants are discussed in Section 7.2.3.

In Figure 7.30(a) and (b) we plot the frequency-dependent dielectric constants, ϵ', and dielectric losses, ϵ'', for $HEX_{0.6}OCT_{0.4}$ doped with 1% LiTFSI, respectively. Data reported in ref. [80] for $HEX_{0.4}OCT_{0.6}$ doped with 1% $LiPF_6$ are included in frame (b) without rescaling. Upon addition of the Li ions, the dielectric constant features a step-like increase as observed for the undoped sample. The relaxation peaks in ϵ'' depicted in Figure 7.30(b) are for this sample also well-defined and appear at a slightly higher temperature window. The observed disparities in data at temperatures T = 254 K and T = 239 K, particularly regarding the dielectric constant, may arise from an incomplete phase transition, resulting in partial rearrangement of the cycloalcohol molecules, see Section 7.2.3 for a detailed discussion of the phase diagram.

Furthermore, comparison with the dielectric data reported for doped $HEX_{0.4}OCT_{0.6}$ by Reuter *et al.* [80] reveals only a small shift in the relaxation maximum in ϵ'' with the relaxation strength being almost the same, suggesting that the time constants are not affected by the difference in HEX:OCT ratio or Li salt.

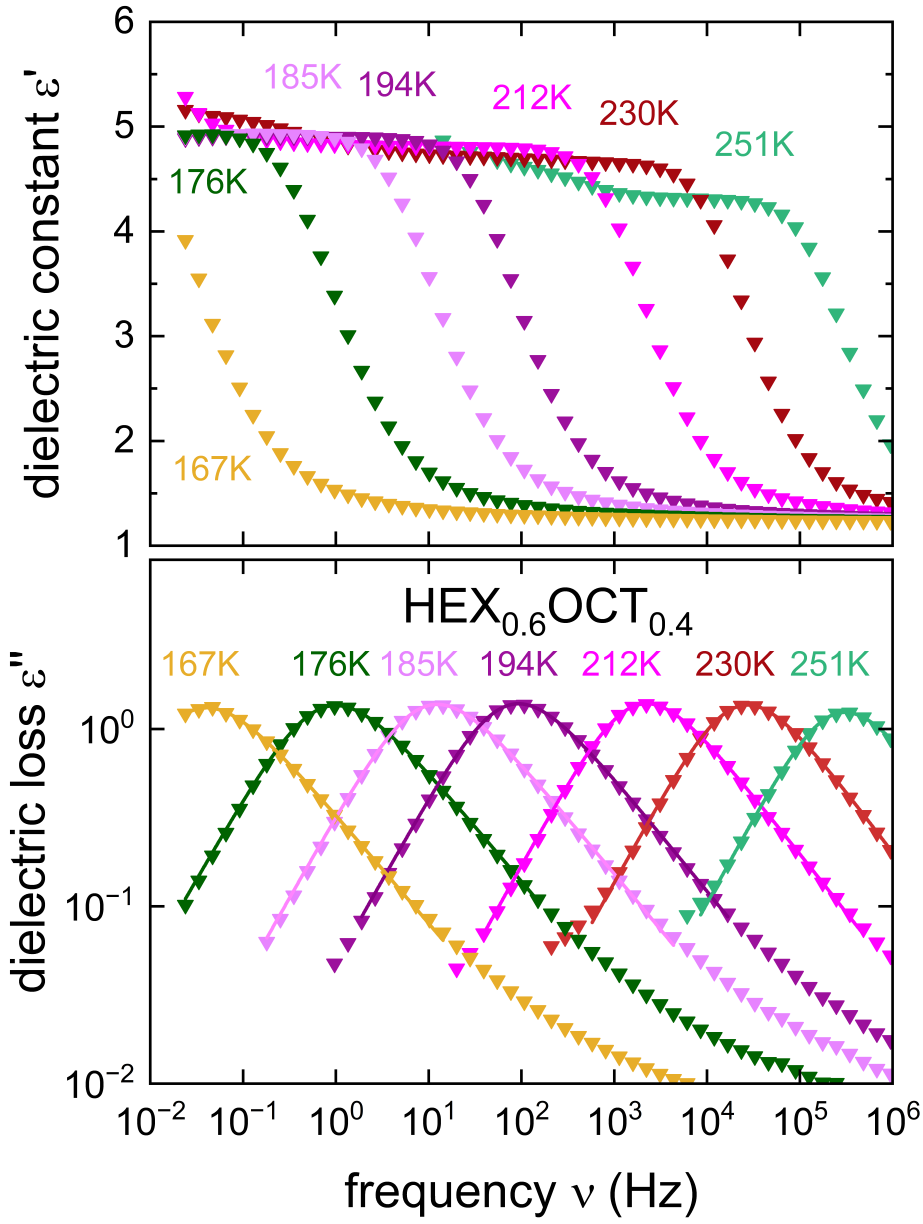

Figure 7.29: Frequency dependent measurements of (a) the real part and (b) the imaginary part of the complex dielectric permittivity of $HEX_{0.6}OCT_{0.4}$. Solid lines in frame (b) correspond to fits using Eq. (5.7) with parameters $\alpha = 0.9 \pm 0.1$ and $\gamma = 0.7 \pm 0.1$. All data were acquired during cooling.

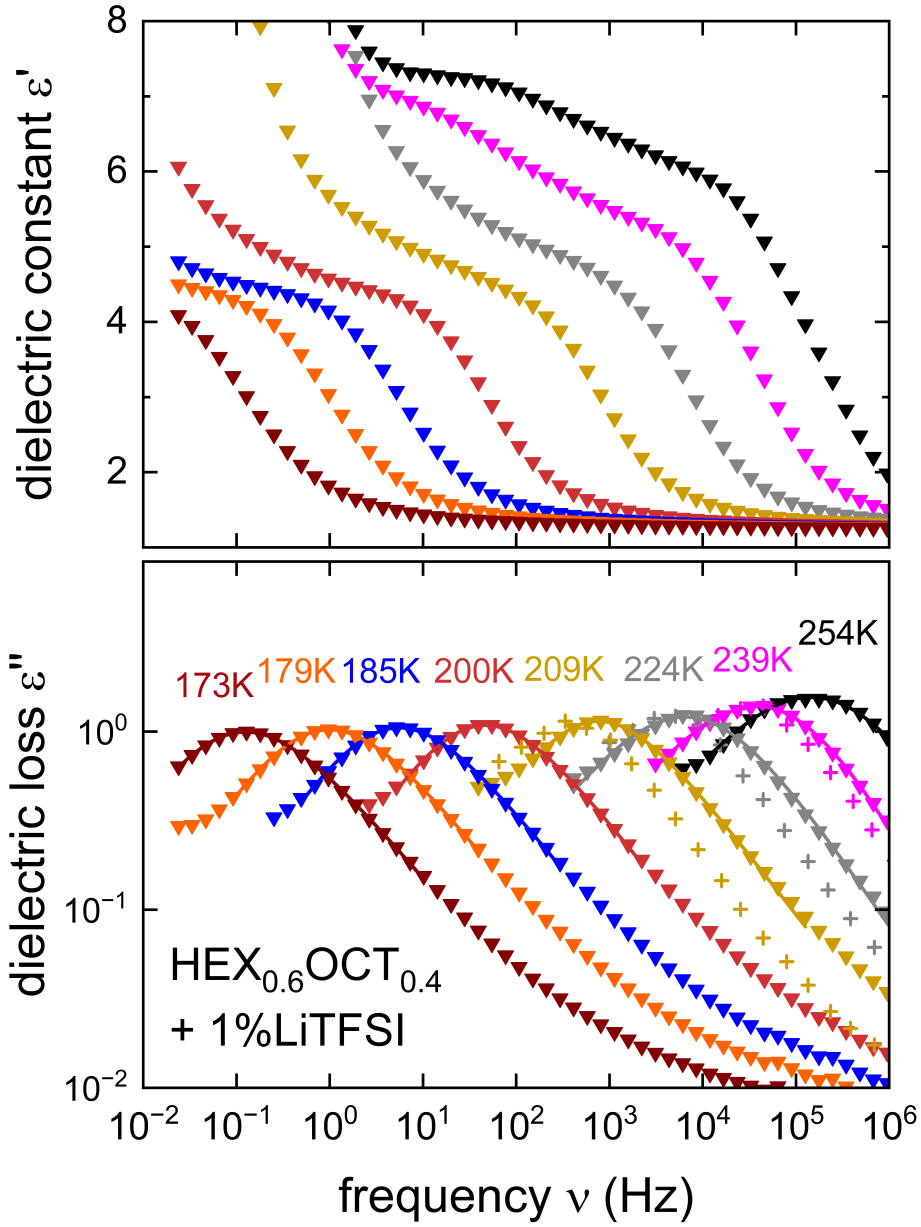

Figure 7.30: Frequency dependent measurements of (a) the real part and (b) the imaginary part of the complex dielectric permittivity of $HEX_{0.6}OCT_{0.4}$ doped with 1%LiTFSI. The plusses (+) in frame (b) are unscaled data reported in ref.[80] for $HEX_{0.4}OCT_{0.6}$ doped with 1%$LiPF_6$. Solid lines in frame (b) correspond to fits using Eq. (5.7) with parameters α = 0.7 ± 0.1 and γ = 0.8 ± 0.1. All data were acquired during cooling.

Figures 7.31(a) and (b) depict the frequency-dependent dielectric constants, ϵ', and dielectric losses, ϵ'', respectively, measured for $HEX_{0.6}OCT_{0.4}$ doped with 5% LiTFSI. In contrast to the mixture doped with 1% LiTFSI, the dielectric constant in frame (a) exhibits a step-like increase with increasing temperature, akin to the undoped mixture. However, the relaxation peaks in frame (b) are significantly affected by the high conductivity of this sample and are only discernable on the converted dielectric constant data, i.e. for ϵ''_{dev}, using Eq. (5.10) and depicted as crosses (×) in Figure 7.31(b).

Furthermore, we plot in Figure 7.32(a), (b) and (c) the real part of the conductivity, σ', measured during cooling for $HEX_{0.6}OCT_{0.4}$, for $HEX_{0.6}OCT_{0.4}$ doped with 1%LiTFSI and for $HEX_{0.6}OCT_{0.4}$ doped with 5%LiTFSI, respectively. Data affected by electrode polarization was neglected. For the undoped sample in frame (a), the DC plateaus appear slightly above 10^{-9} S/cm around room temperature before experiencing a sudden jump at T = 260 K, reflecting a phase transition. Reuter *et. al.*[80] have reported a melting temperature around T = 268 K from the liquid to the PC phase for the same mixture doped with 1% $LiPF_6$. This transition is indeed also evident in our sample doped with 1% LiTFSI but is not observable in the sample doped with 5% LiTFSI. Additionally, although the addition of Li ions to the $HEX_{0.6}OCT_{0.4}$ mixture improves the overall conductivity by approximately three orders of magnitude, the resulting conductivity remains well below 10^{-3} S/cm, the target conductivity for Li-electrolytes, even for the sample doped with 5% LiTFSI.

To better visualize the phase transition occurring around T = 260 K, we present in Figure 7.33(a), (b), and (c) the temperature-dependent dielectric loss at constant frequencies measured during cooling (triangles pointing downward) and heating (triangles pointing upward) for the three discussed samples. The phase transition becomes evident for all three samples with $HEX_{0.6}OCT_{0.4}$ and $HEX_{0.6}OCT_{0.4}$ doped with 1% LiTFSI, characterized by a significant discontinuity in $d\epsilon''/dT$ in comparison to $HEX_{0.6}OCT_{0.4}$ doped with 5% LiTFSI. The phase diagram of the $HEX_{0.6}OCT_{0.4}$ mixtures and all the doped samples investigated is further discussed in Section 7.2.3 below.

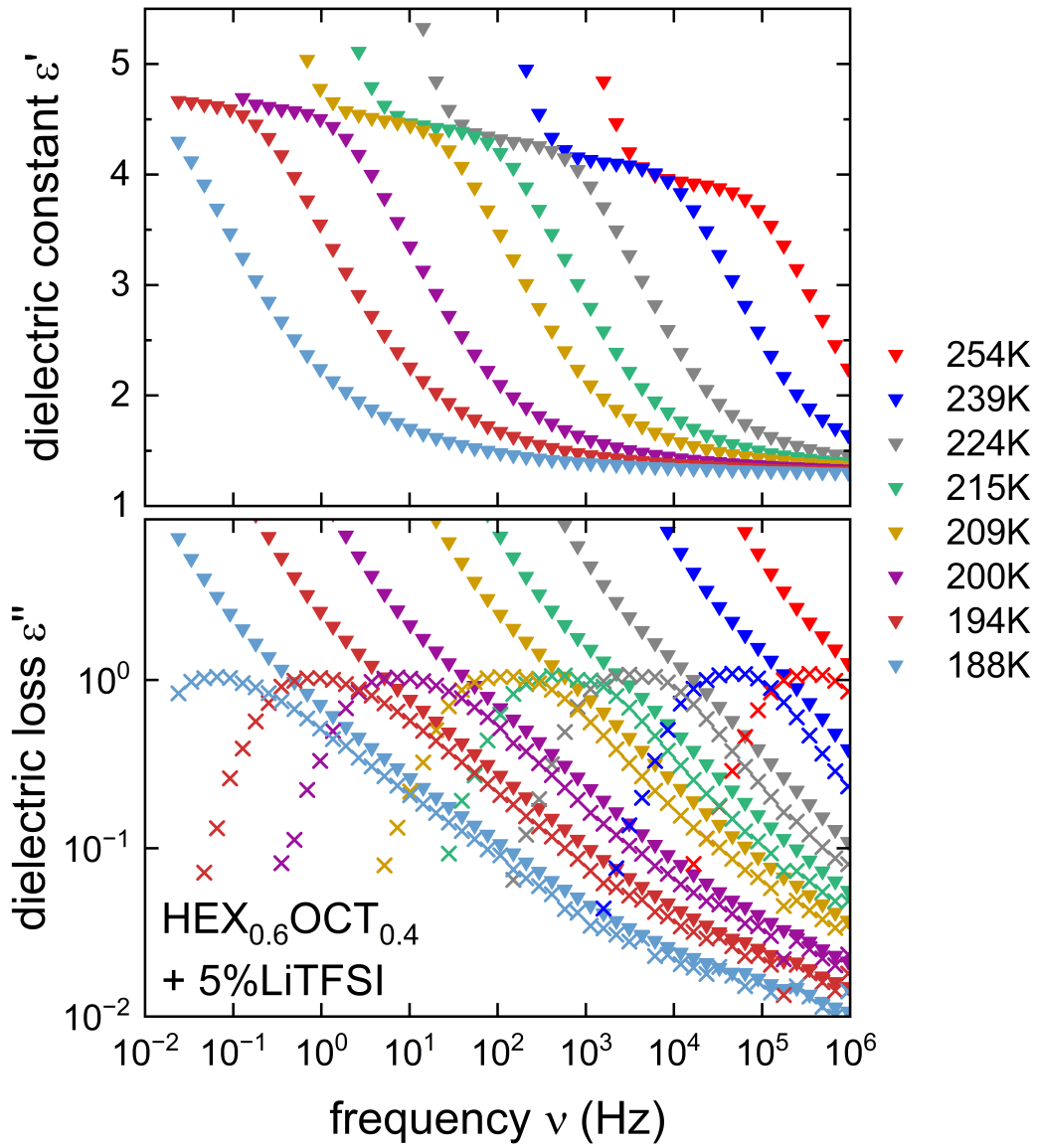

Figure 7.31: Frequency dependent measurements of (a) the real part and (b) the imaginary part of the complex dielectric permittivity of $HEX_{0.6}OCT_{0.4}$ doped with 5%LiTFSI. The crosses (×) in frame (b) are derived from the dielectric constant ϵ' according to Eq. (5.10). All data were acquired during cooling.

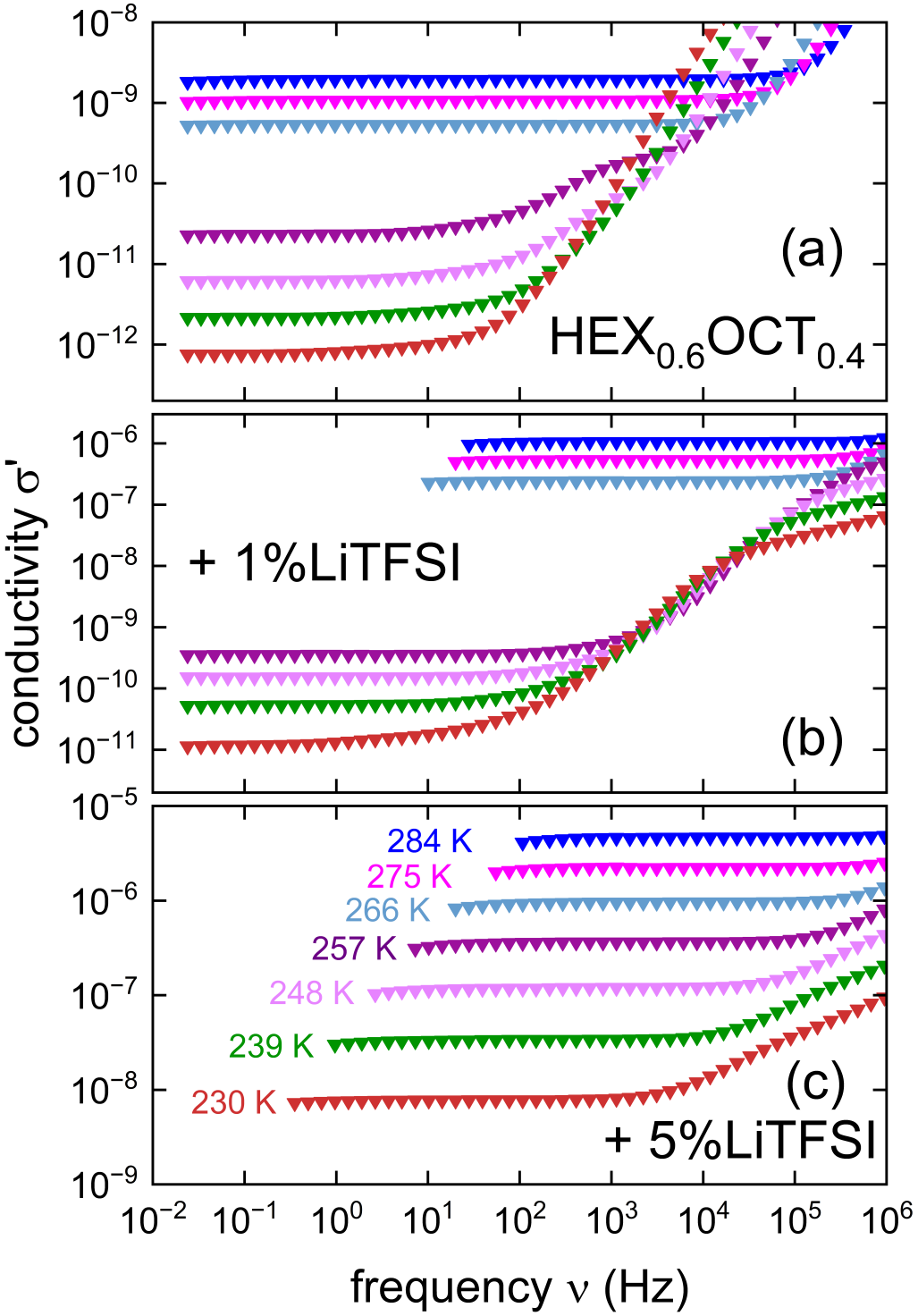

Figure 7.32: Frequency dependent measurements of the real part of the conductivity σ' for (a) $HEX_{0.6}OCT_{0.4}$ (b) $HEX_{0.6}OCT_{0.4}$ doped with 1%LiTFSI and (c) $HEX_{0.6}OCT_{0.4}$ doped with 5%LiTFSI. The measurements were conducted during cooling. Temperatures for all three samples are equal as indicated in frame (c) by identical colors.

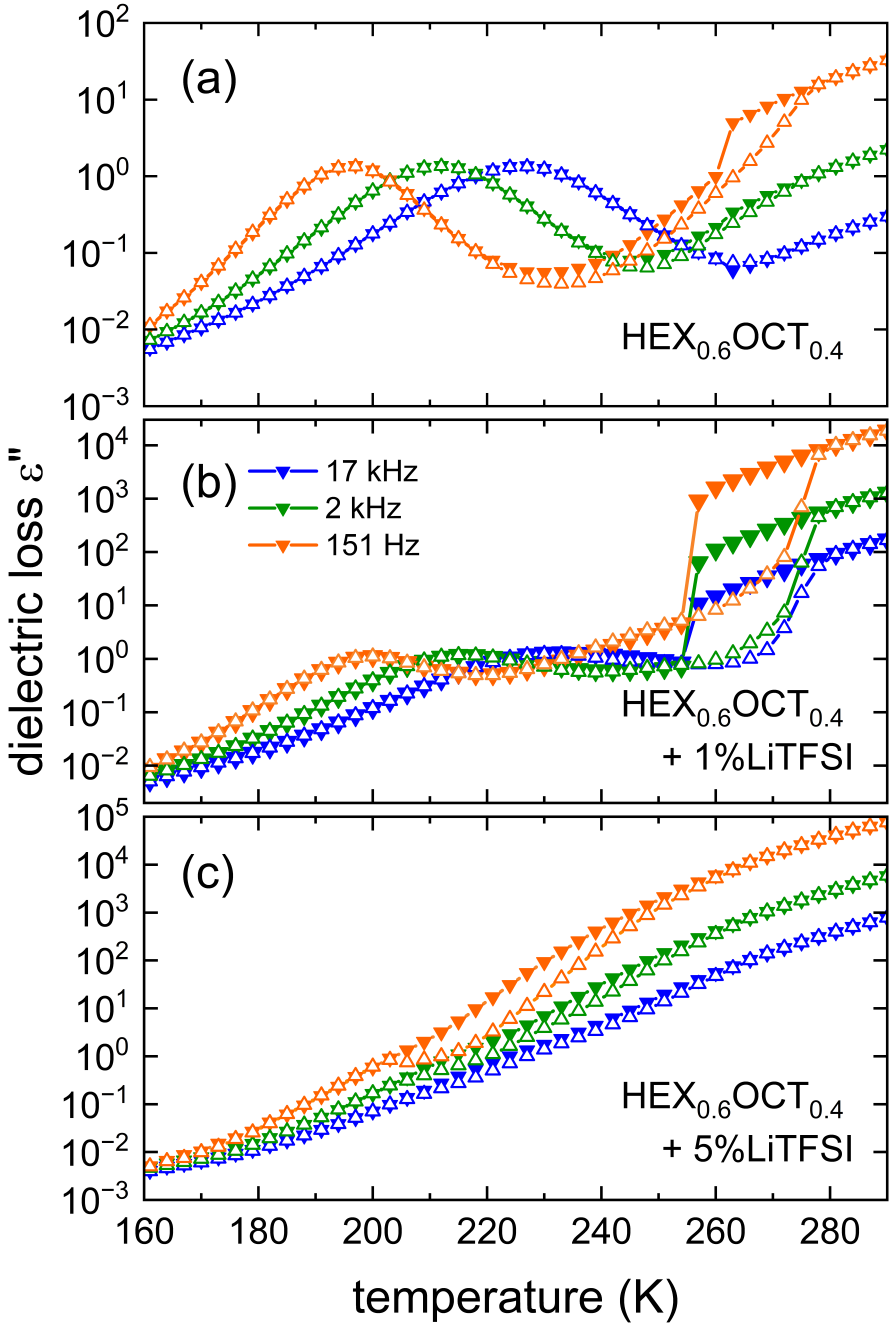

Figure 7.33: Temperature dependent dielectric loss across various frequencies of (a) $HEX_{0.6}OCT_{0.4}$ (b) $HEX_{0.6}OCT_{0.4}$ doped with 1%LiTFSI and (c) $HEX_{0.6}OCT_{0.4}$ doped with 5%LiTFSI. The measurements were conducted during cooling (solid triangles pointing down) or heating (open triangles pointing up). The lines are drawn to guide the eye.

Deuterium and lithium spectroscopy

Similar to the SN-GN mixture, we employed ^{2}H NMR spectroscopy to gain further insights into the dynamics of the cycloalcohol matrix. The static solid echo spectrum acquired at T = 145 K for (HEX-d_{11})$_{0.6}$(OCT)$_{0.4}$ is illustrated in Figure 7.34. One can recognize the characteristic Pake doublet with a splitting $\Delta\nu \approx 120$ kHz, which aligns with the value observed for the SN-GN mixture and the typical quadrupolar coupling constant for deuterium.[136] Moreover, the asymmetry parameter can be determined using $\eta_Q = 1 - (2 \times \Delta\nu)/b$, where b can be calculated from the spectral separation of the outer edge singularities. The asymmetry parameter is foud to be $\eta_Q \approx 0$. Additionally, the spectrum reflects an interference peak around 160 kHz, which is likely due to instrumental artifacts.

Furthermore, the ^{7}Li central-transition lines for (HEX-d_{11})$_{0.6}$(OCT)$_{0.4}$ and their respective full width at half maximum (FWHM), spanning temperatures from 263 to 219 K, are depicted in Figure 7.35 and Figure 7.36, respectively. These spectra exhibit a single peak characterized by a linewidth of a few kilohertz, akin to the SN-GN mixture. We employ Eq. (7.1) with $\Delta\nu_{RL} = 8$ kHz and $A = 1$ to extract correlation times from the FWHM and discuss the results in Section 7.2.3.

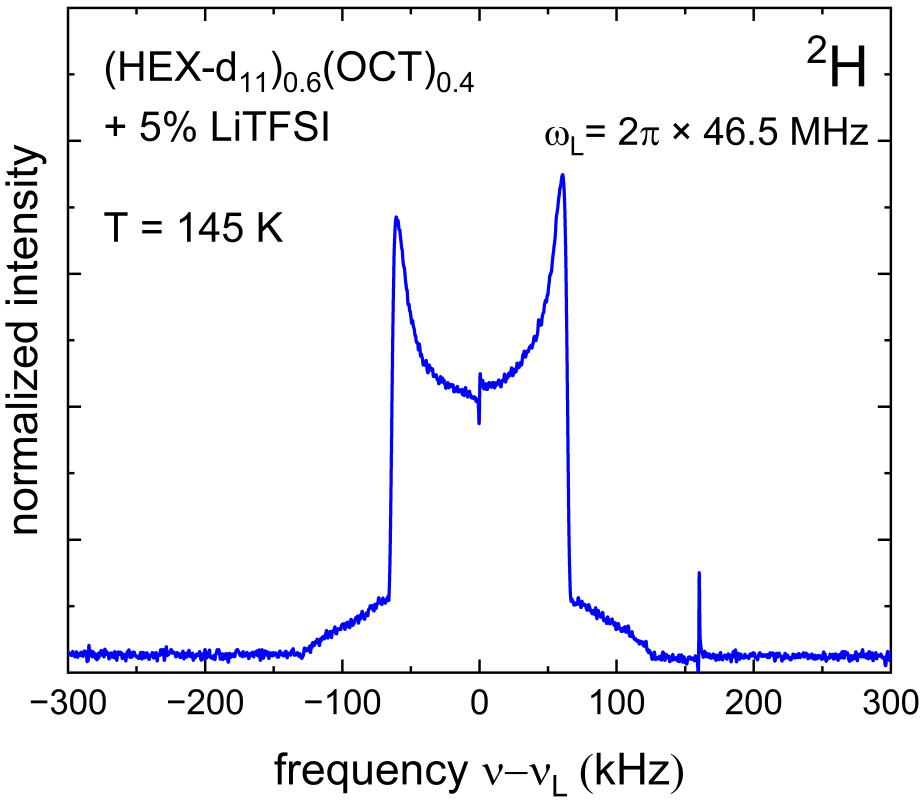

Figure 7.34: ^{2}H solid echo spectrum recorded for (HEX-d_{11})$_{0.6}$(OCT)$_{0.4}$ doped with 5% LiTFSI at $\omega_L = 2\pi \times 46.5$ MHz and T = 145 K. The spectrum exhibits a horn splitting of approximately 120 kHz.

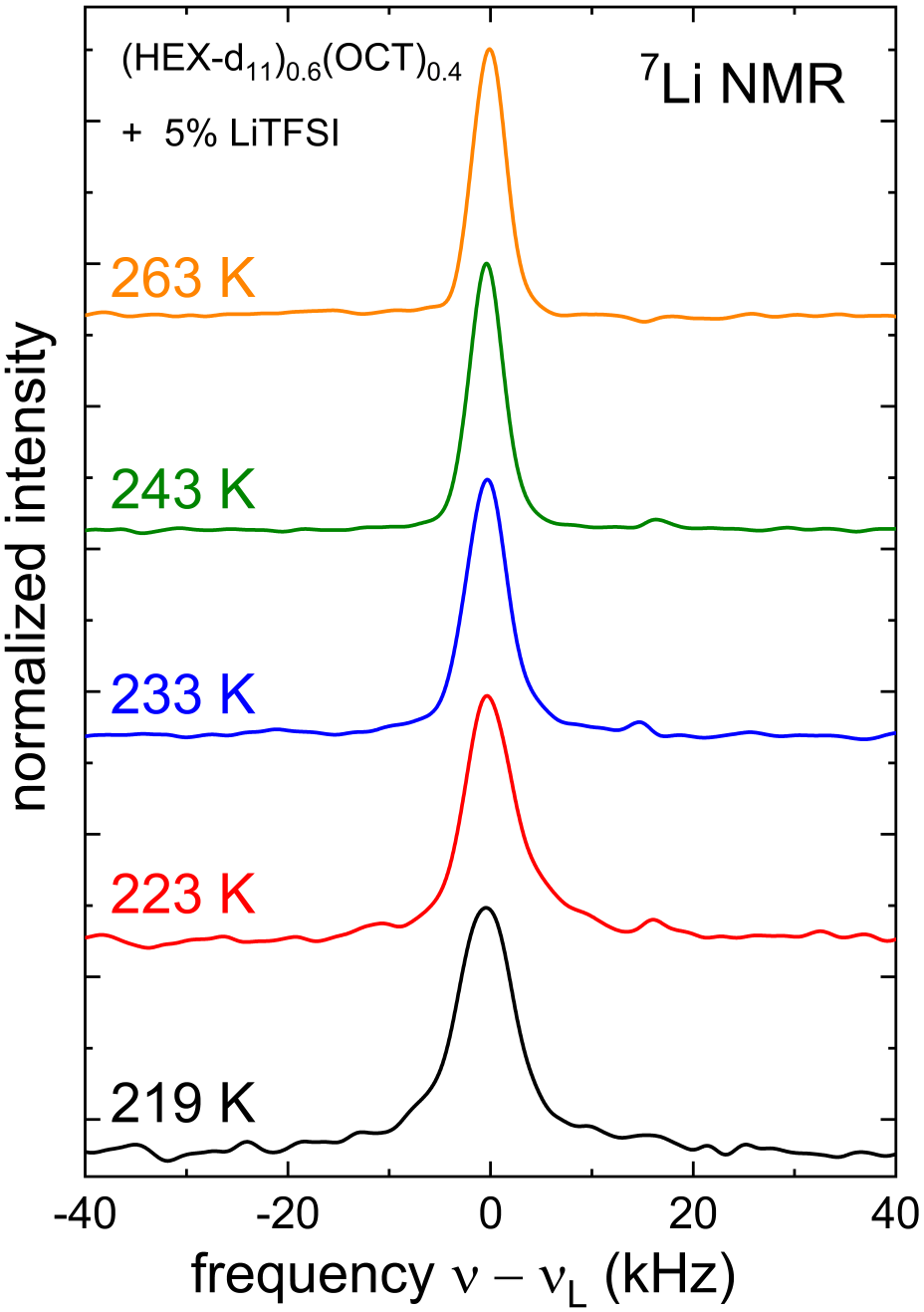

Figure 7.35: ^{7}Li solid echo spectra acquired at $\omega_L = 2\pi \times 116.9$ MHz for (HEX-d_{11})$_{0.6}$(OCT)$_{0.4}$ doped with 5% LiTFSI. Measurements were conducted while cooling.

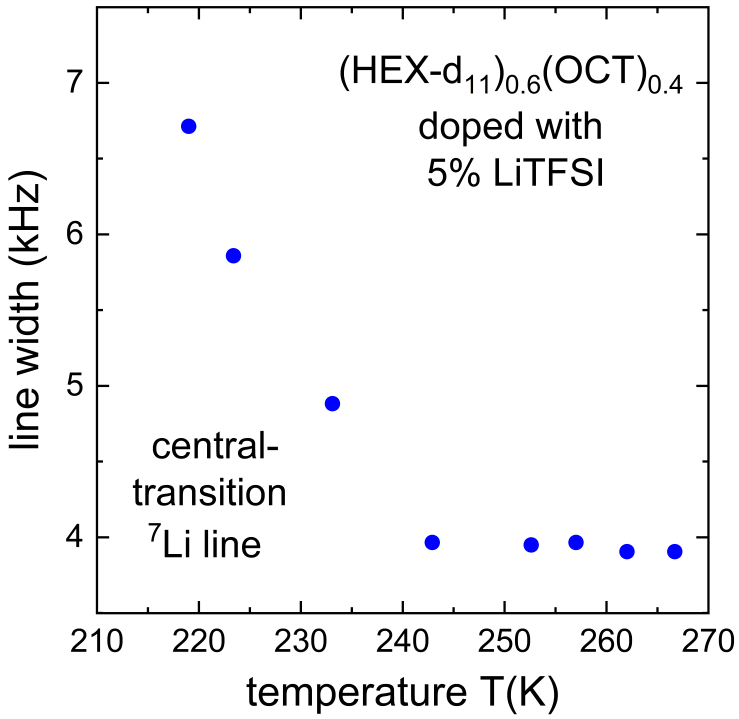

Figure 7.36: ^{7}Li central-transition line widths determined for (HEX-d_{11})$_{0.6}$(OCT)$_{0.4}$ doped with 5% LiTFSI. No satellite line were observed.

Deuterium and lithium relaxometry

In a similar approach to the SN-GN mixture, we employed ^{2}H and ^{7}Li NMR relaxometry to delve deeper into the reorientational motion of the cycloalcohol matrix as well as that of the Li ions. Figure 7.37 illustrates the temperature-dependent ^{2}H spin-lattice relaxation times T_1 and spin-spin relaxation times T_2 measured during cooling for (HEX-d_{11})$_{0.6}$(OCT)$_{0.4}$ doped with 5% LiTFSI. Also depicted are the ^{7}Li spin-lattice relaxation times T_1 measured for the same sample. Additionally, we present the T_1 and T_2 values acquired for (HEX-d_{11})$_{0.4}$(OCT)$_{0.6}$ doped with 5% LiTFSI.

The deuterium data shown in Figure 7.37 highlights some interesting aspects of the relaxational behavior of the (HEX-d_{11})$_{0.6}$(OCT)$_{0.4}$ matrix doped with 5% LiTFSI: The T_1 and T_2 values, acquired across the temperature range of 280 to 140 K are not equal and extend beyond the low-temperature side of the T_1 minimum. The precise location of the T_1 minimum within this temperature range remains somewhat elusive, suggesting the need for measurements at higher temperatures to achieve clarity. Unfortunately, within the timeframe of this study, further measurements for better definition of T_1 were not possible. Nonetheless, based on the available data, it can be speculated that the T_1 minimum likely occurs around 280 K or slightly higher. The T_2 data on the other hand, exhibit a clear minimum around 228 K.

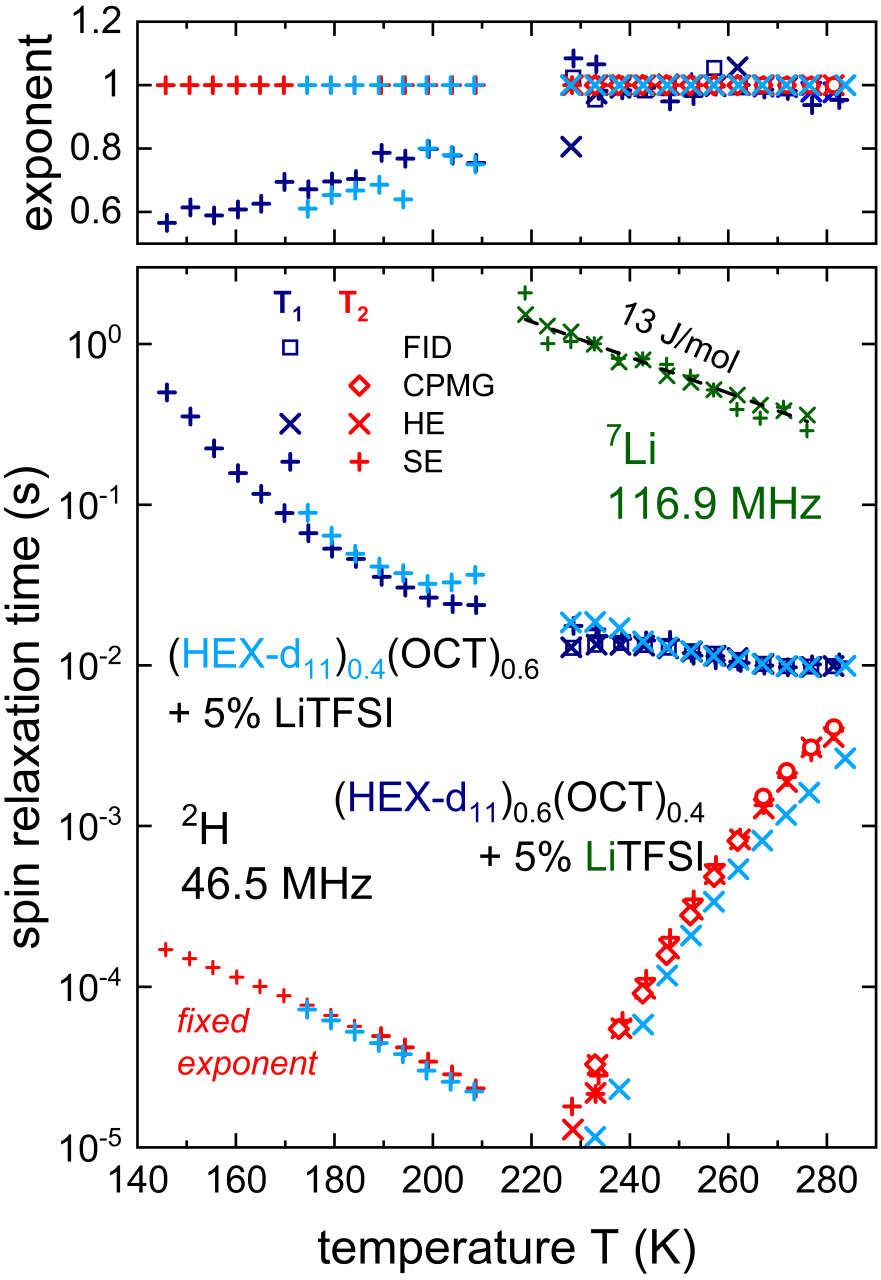

Figure 7.37: Temperature-dependent ^{2}H spin-lattice relaxation times (T_1, represented by dark blue symbols) and spin-spin relaxation times (T_2, represented by red symbols) are depicted for (HEX-d_{11})$_{0.6}$(OCT)$_{0.4}$ doped with 5% LiTFSI. The measurements utilized SE sequences (+). Data above 220 K includes measurements obtained using HE (×) and FID (□) or CPMG (◊) pulse sequences. Additionally, T_1 and T_2 values acquired for (HEX-d_{11})$_{0.4}$(OCT)$_{0.6}$ doped with 5% LiTFSI are depicted in light blue (×) or (+). Data for the latter compound were acquired using HE pulse sequences (for T > 220 K) or SE pulse sequences (for T < 220 K). Temperature-dependent ^{7}Li spin-lattice relaxation times for (HEX-d_{11})$_{0.6}$(OCT)$_{0.4}$ are included as well, represented in green (+ for SE pulse sequence) or (× for HE pulse sequence). The Kohlrausch exponent for all T_2 values was set to 1.0. All data were acquired during cooling.

Moreover, above 220 K, all T_1 and T_2 values become equivalent, irrespective of the pulse sequence employed for measurements. Altering the mixing ratio from $(HEX\text{-}d_{11})_{0.6}(OCT)_{0.4}$ to $(HEX\text{-}d_{11})_{0.4}(OCT)_{0.6}$ results in minimal impact on the relaxation behavior of the matrix. Indeed, the T_1 and T_2 values acquired for $(HEX\text{-}d_{11})_{0.4}(OCT)_{0.6}$ are only marginally different from those obtained for $(HEX\text{-}d_{11})_{0.6}(OCT)_{0.4}$.

In contrast to the behavior of deuterium, the ^{7}Li T_1 values exhibit a linear increase with temperature. Employing the Arrhenius law, the activation energy below the T_1 minimum is calculated to be E_A = 13 J/mol, significantly lower than that obtained for the SN-GN mixture above the T_1 minimum (17 kJ/mol).

7.2.2 Highly Li-doped cyclohexanol or cyclooctanol

To investigate the potential use of cycloalcohols as deep eutectic solvents, we conducted dielectric spectroscopy measurements on HEX and OCT doped with high concentrations of LiTFSI. Figures 7.38, 7.39, 7.40, and 7.40 display the frequency-dependent results obtained for $HEX_{0.85}LiTFSI_{0.15}$, $HEX_{0.80}LiTFSI_{0.20}$, $OCT_{0.85}LiTFSI_{0.15}$, and $OCT_{0.80}LiTFSI_{0.20}$, respectively. In these figures, frames (a) represent the dielectric constants, ϵ', and frames (b) represent the dielectric losses, ϵ''.

Similar to the $HEX_{0.6}OCT_{0.4}$ samples doped with 5% LiTFSI and higher concentrations, both the binary HEX-LiTFSI and OCT-LiTFSI systems exhibit a distinct step-like increase in their dielectric constant ϵ' with decreasing temperature. Additionally, the dielectric loss ϵ'' is notably effected by the conductivity effects resulting from the high lithium concentrations. Upon converting the dielectric constant data to dielectric loss using Eq. (5.10), the relaxation peaks become apparent, indicated by crosses (×) in frames (b).

Furthermore, Figures 7.42 and 7.43 present the real part of the conductivity, σ', for the investigated HEX-LiTFSI and OCT-LiTFSI mixtures, respectively. Frames (a) display data measured for samples doped with 15% LiTFSI, while frames (b) depict data measured for samples doped with 20% LiTFSI. Data affected by electrode polarization were neglected. For the HEX samples, the DC plateaus appear around 10^{-5} S/cm at room temperature, with no significant difference between the 15%LiTFSI and 20%LiTFSI samples.

Moreover, the OCT samples in Figure 7.43 show similar features, with the DC plateaus appearing around the same values and no significant difference between $OCT_{0.85}LiTFSI_{0.15}$ and $OCT_{0.80}LiTFSI_{0.20}$. The conductivity of the highly doped cycloalcohols is further discussed in Section 7.2.3.

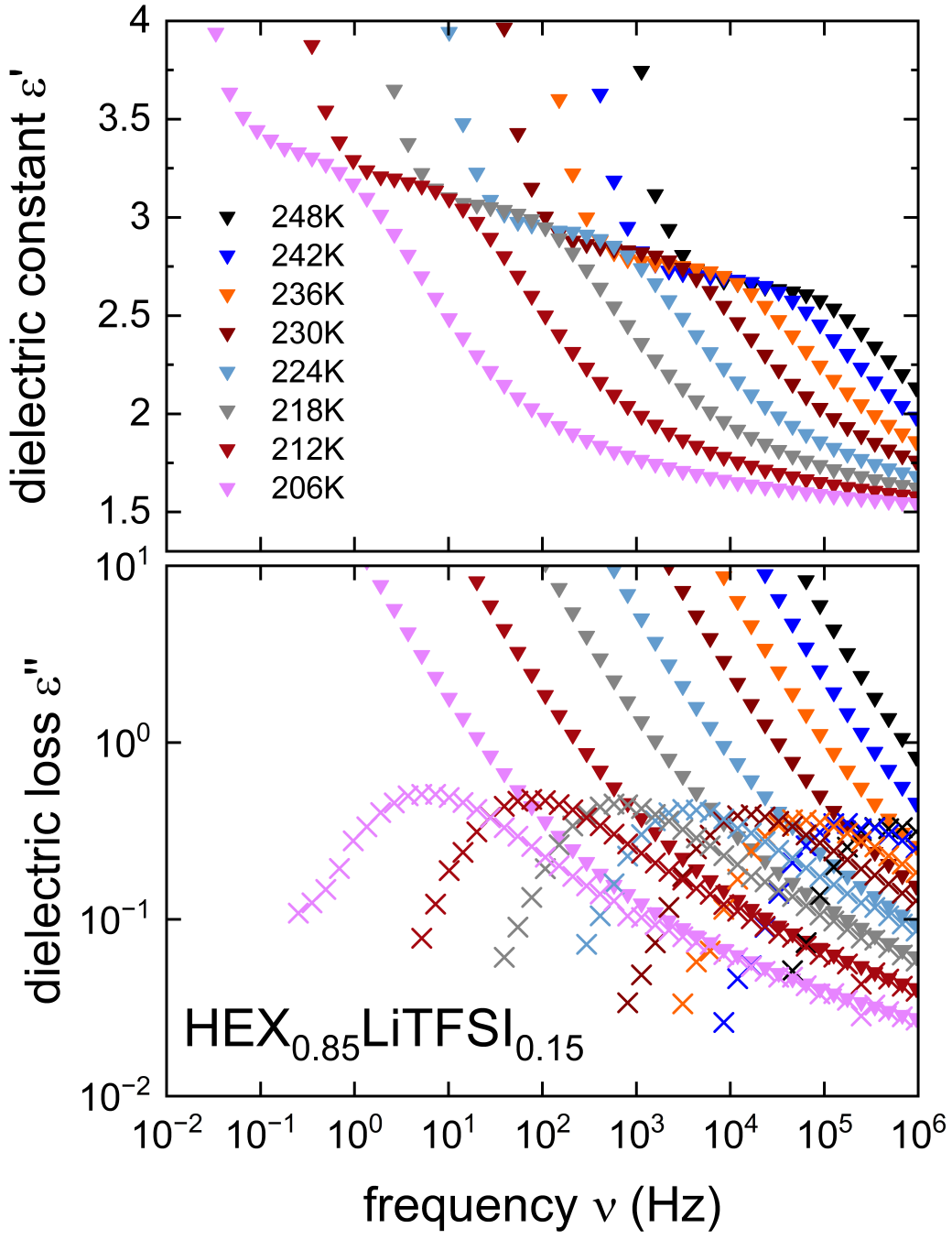

Figure 7.38: Frequency dependent measurements of (a) the real part and (b) the imaginary part of the complex dielectric permittivity of $HEX_{0.85}LiTFSI_{0.15}$. The crosses (×) in frame (b) are derived from the dielectric constant ϵ' according to Eq. (5.10). All data were acquired during cooling.

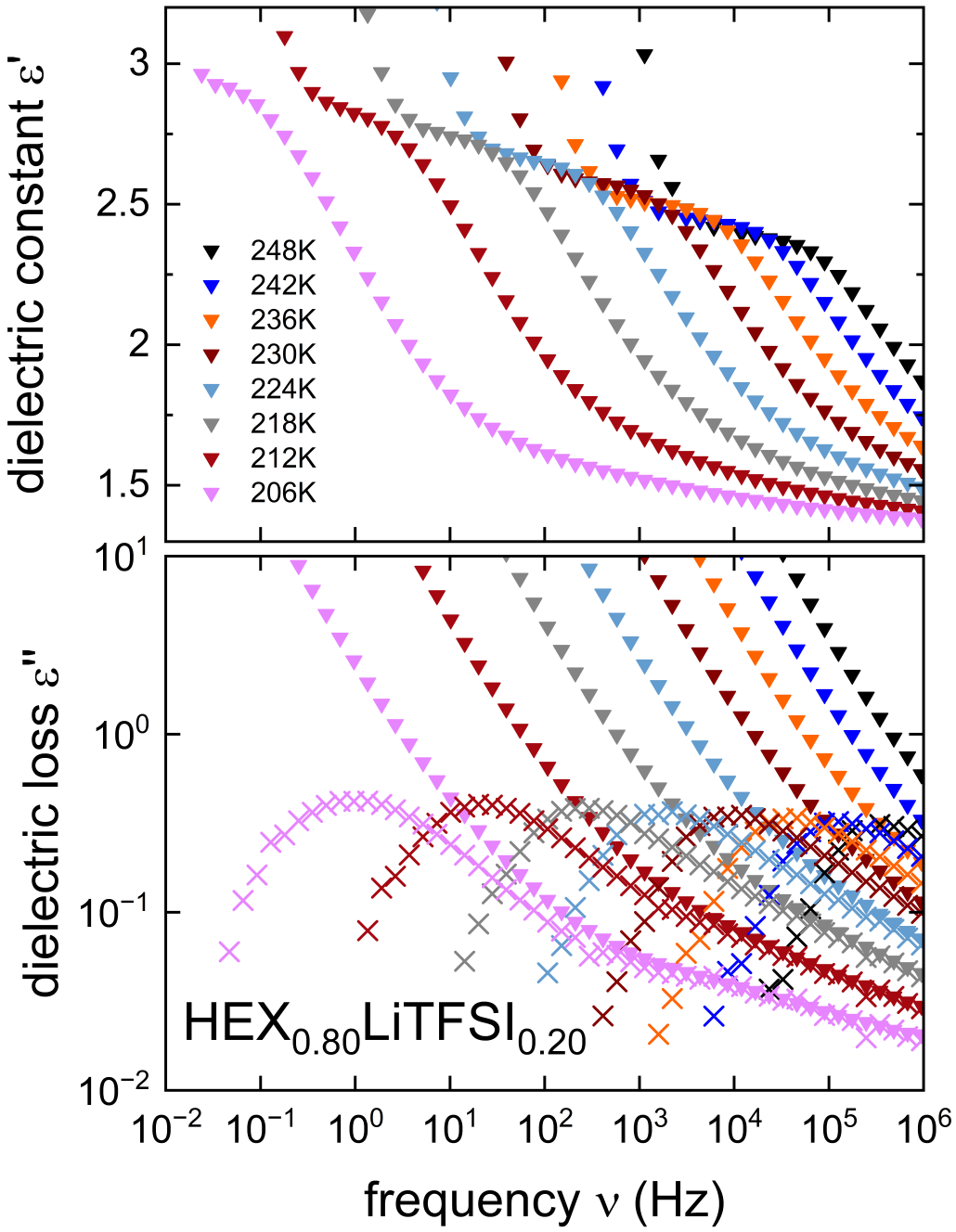

Figure 7.39: Frequency dependent measurements of (a) the real part and (b) the imaginary part of the complex dielectric permittivity of $HEX_{0.80}LiTFSI_{0.20}$. The crosses (×) in frame (b) are derived from the dielectric constant ϵ' according to Eq. (5.10). All data were acquired during cooling.

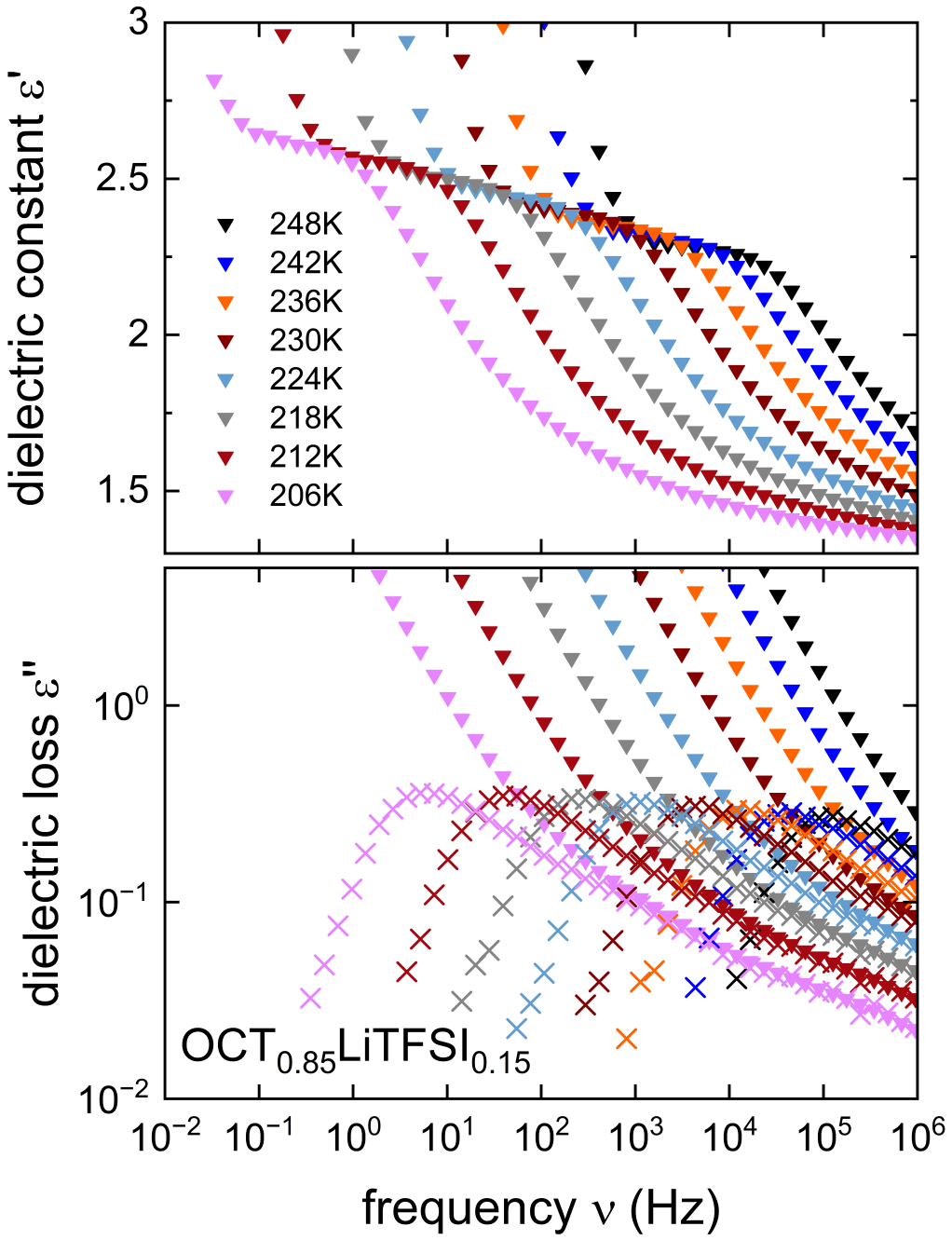

Figure 7.40: Frequency dependent measurements of (a) the real part and (b) the imaginary part of the complex dielectric permittivity of $OCT_{0.85}LiTFSI_{0.15}$. The crosses (×) in frame (b) are derived from the dielectric constant ϵ' according to Eq. (5.10). All data were acquired during cooling.

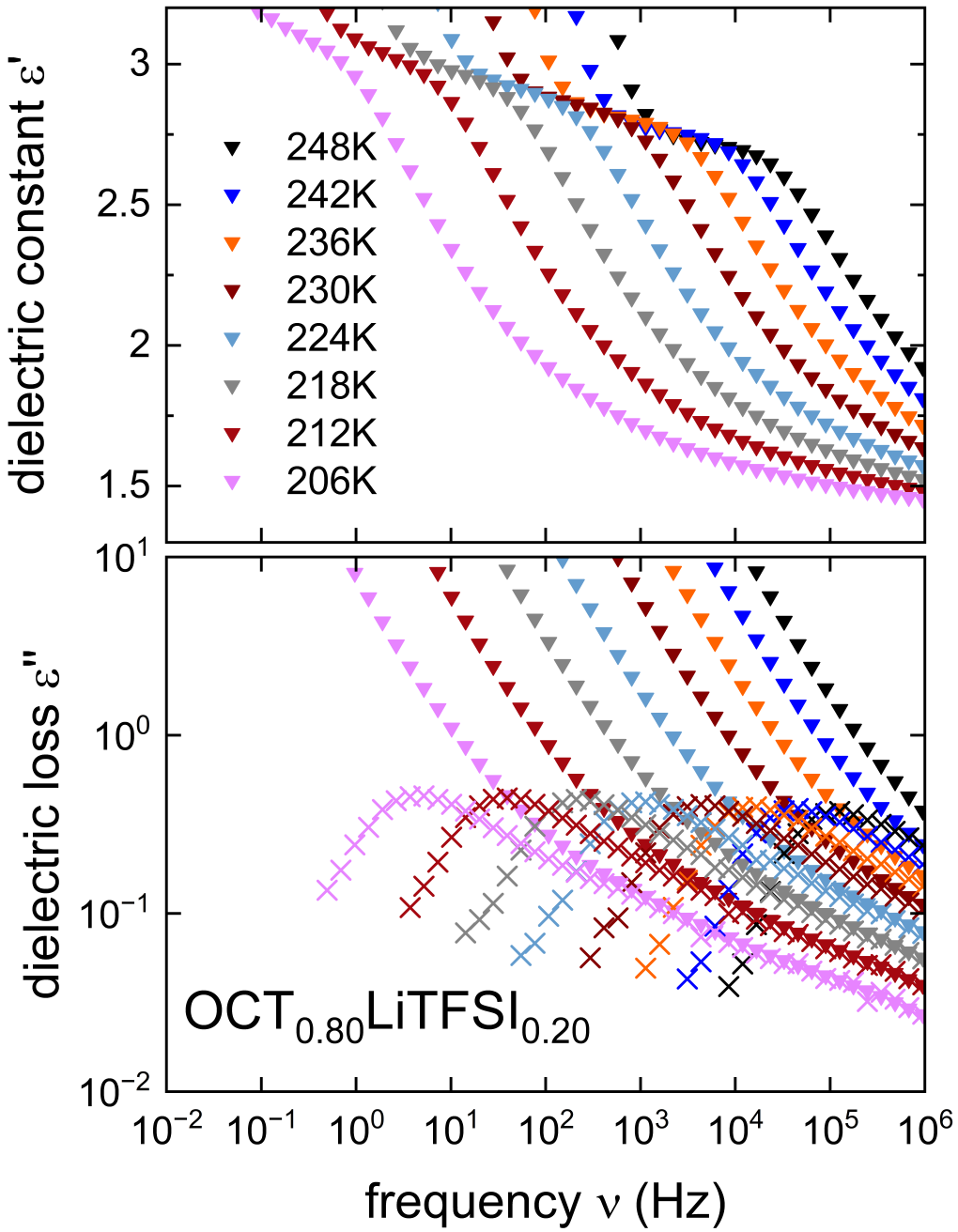

Figure 7.41: Frequency dependent measurements of (a) the real part and (b) the imaginary part of the complex dielectric permittivity of $OCT_{0.80}LiTFSI_{0.20}$. The crosses (×) in frame (b) are derived from the dielectric constant ϵ' according to Eq. (5.10). All data were acquired during cooling.

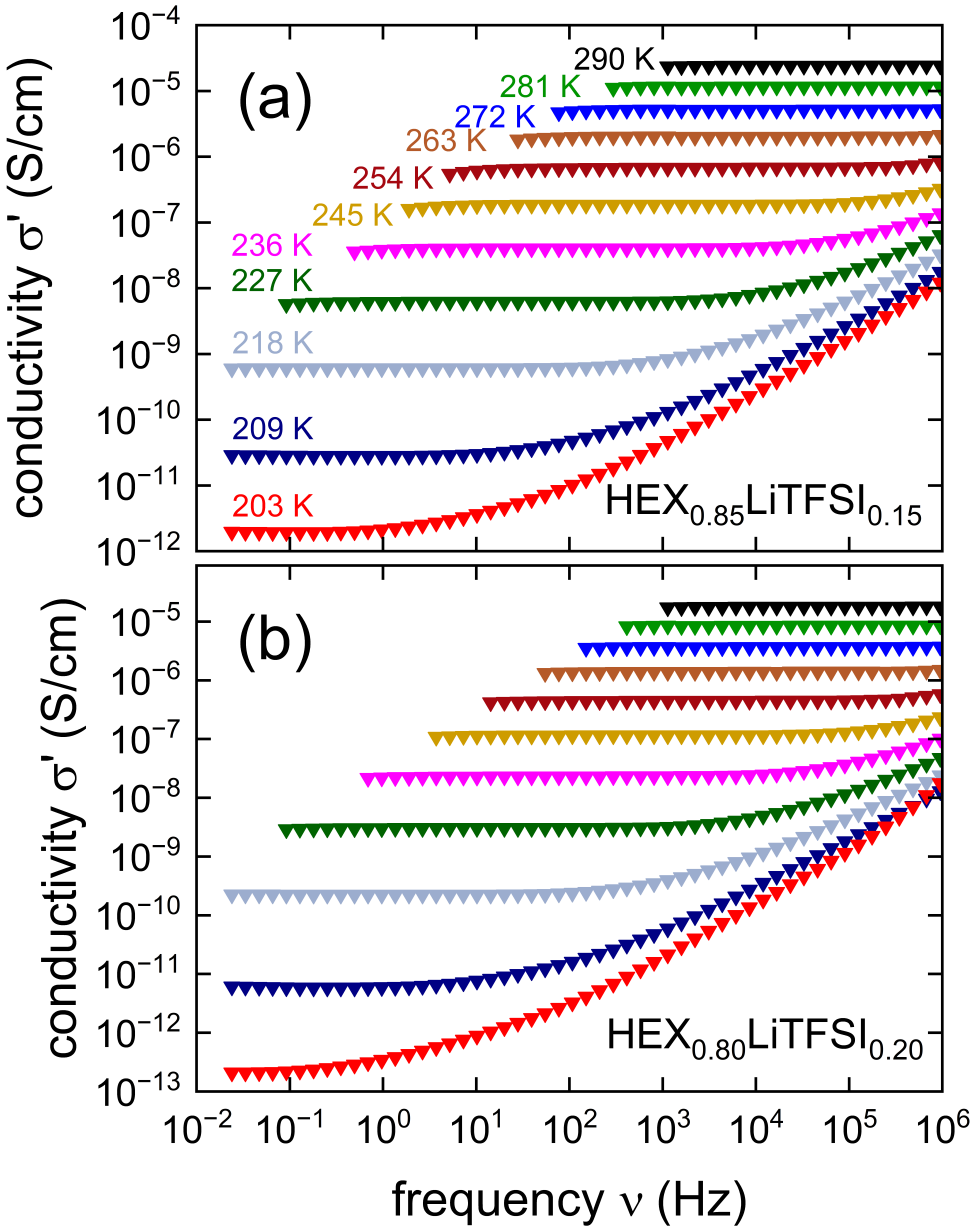

Figure 7.42: Frequency dependent measurements of the real part of the conductivity σ' for (a) $HEX_{0.85}LiTFSI_{0.15}$ and (b) $HEX_{0.80}LiTFSI_{0.20}$. All data were acquired during cooling.

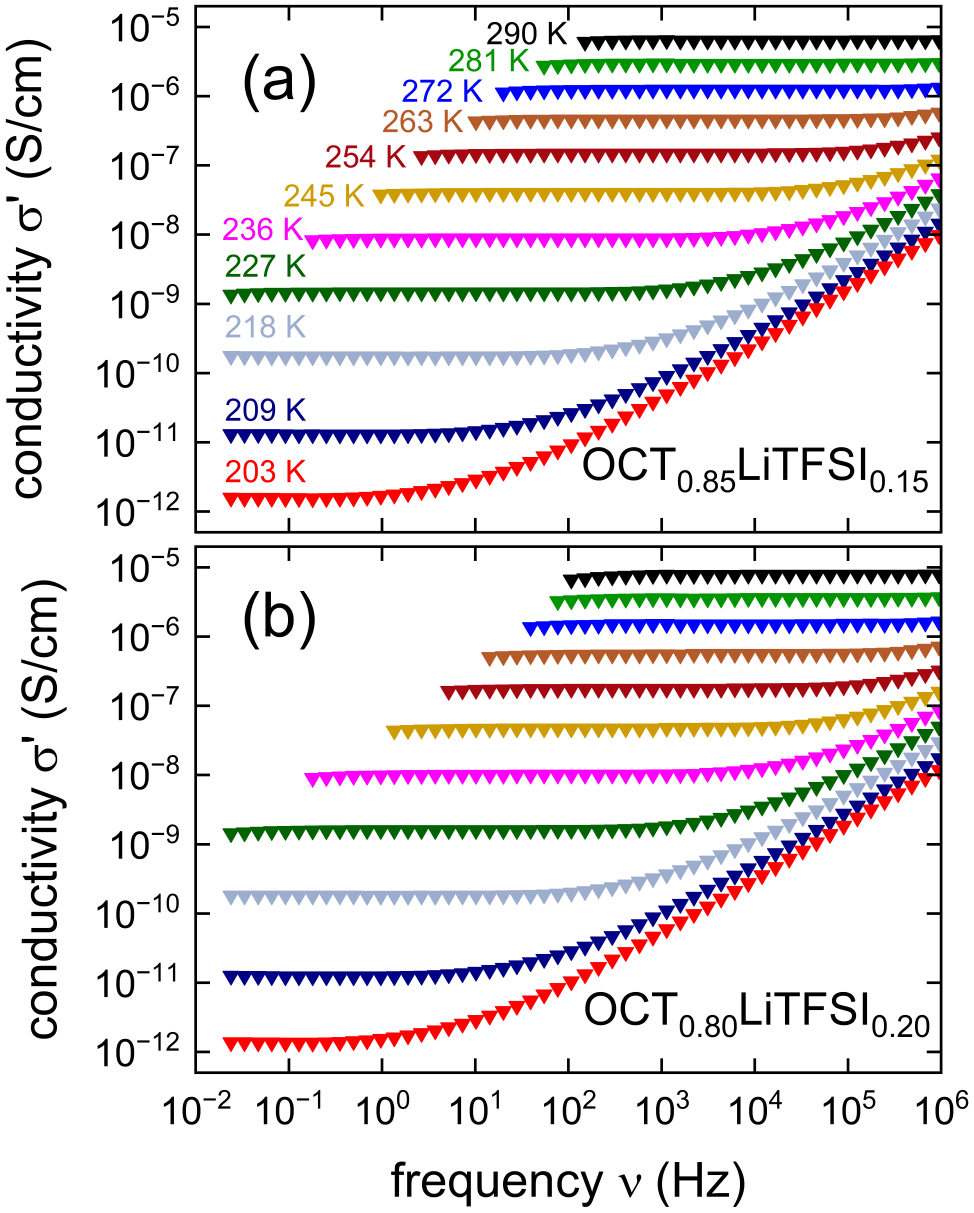

Figure 7.43: Frequency dependent measurements of the real part of the conductivity σ' for (a) $OCT_{0.85}LiTFSI_{0.15}$ and (b) $OCT_{0.80}LiTFSI_{0.20}$. All data were acquired during cooling.

To examine potential phase transitions occurring in these highly doped cycloalcohol samples, we plotted Figures 7.44 and 7.45, showing the temperature-dependent dielectric loss across various frequencies for (a) HEX or OCT doped with 15%LiTFSI and (b) HEX or OCT doped with 20%LiTFSI. These experiments were carried out during a cooling run (solid triangles pointing down) or a heating run (open triangles pointing up).

Although not previously observable in the conductivity data measured during the cooling run (see Figures 7.42 and 7.43), a phase transition between 220 and 240 K is now discernable in the dielectric loss data of all four investigated samples acquired during the heating run. Considering the phase diagram of HEX, see Section 2.2, a transition from the plastic phase (phase I) to the perfectly ordered phase (phase II) should occur around 265 K. However, such a phase transition should be reflected in a significant jump in the dielectric data, which is not the case for σ'.

Furthermore, another phase transition according to HEX's phase diagram that would explain the discontinuities observed in the dielectric loss data in Figure 7.44, is the phase transition from [phase III to phase I. Indeed, when cooling at sufficiently high rates to 100 K and subsequent heating, the plastic phase of HEX undergoes a phase transition at around 195 K to a metastable and ordered phase III. This latter one can transition to phase I at around 245 K, which would correspond well with the observation made on the dielectric loss data acquired during the heating run, see empty triangles pointing upward in Figure 7.44. Such an interpretation would also explain why the discontinuities in the dielectric loss data is not observed in the cooling run.

Moreover, two phase transitions are known for OCT within our investigated temperature range: a phase transition around 265 K from the plastic phase to a partially ordered phase and a second one around 220 K to a fully ordered phase.[82, 168, 169]. Thus, a possible explanation of the dielectric features observed in Figure 7.45 for the OCT samples, involves a phase transition to a partially ordered phase around 230 K that is only healed at temperatures near 270 K. These phase transitions based on the dielectric loss data for the highly doped samples are further discussed in Section 7.2.3.

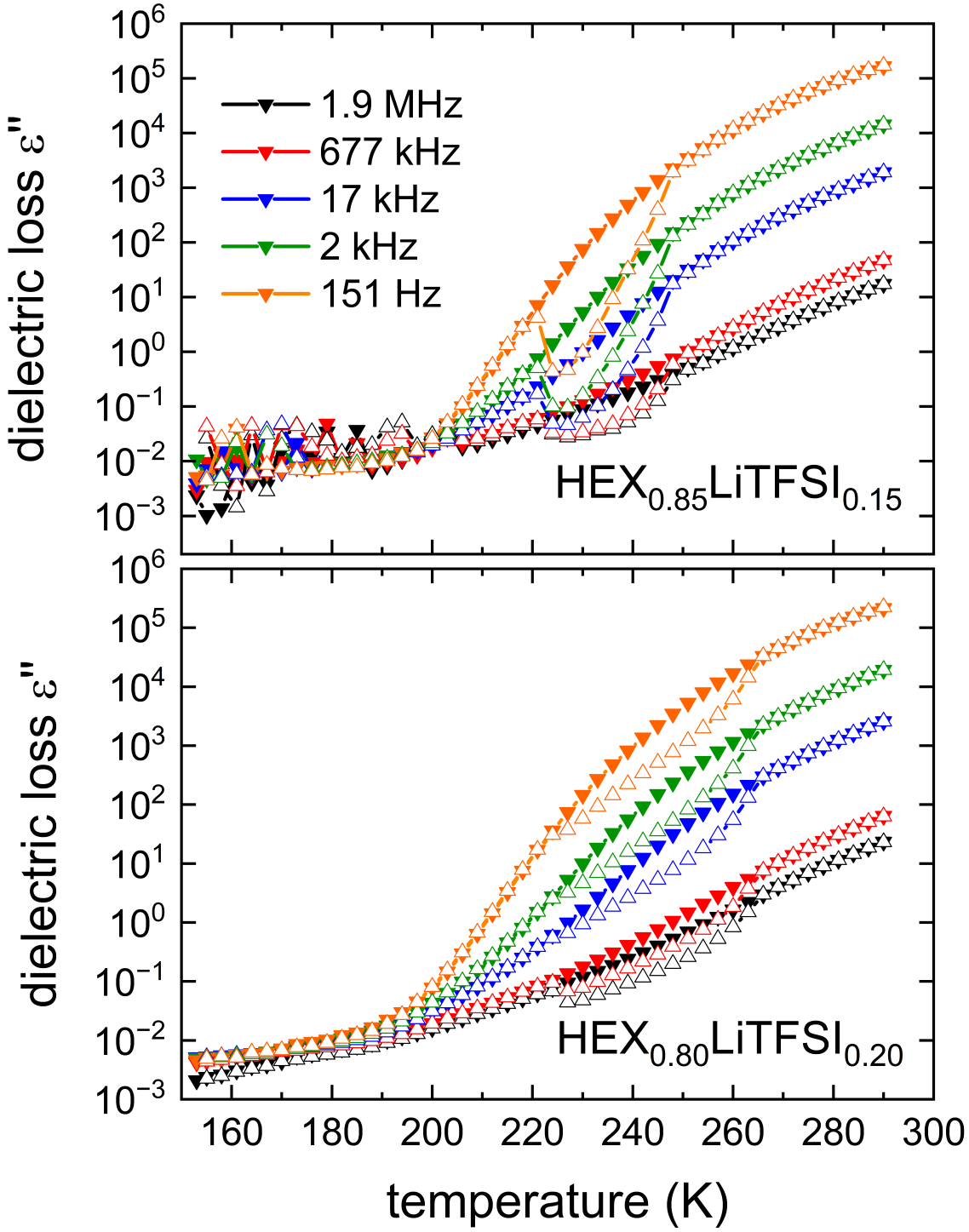

Figure 7.44: Temperature dependent dielectric loss across various frequencies of (a) $HEX_{0.85}LiTFSI_{0.15}$ and (b) $HEX_{0.80}LiTFSI_{0.20}$. Measurements were conducted during cooling (solid triangles pointing down) or heating (open triangles pointing up). The lines are drawn to guide the eye.

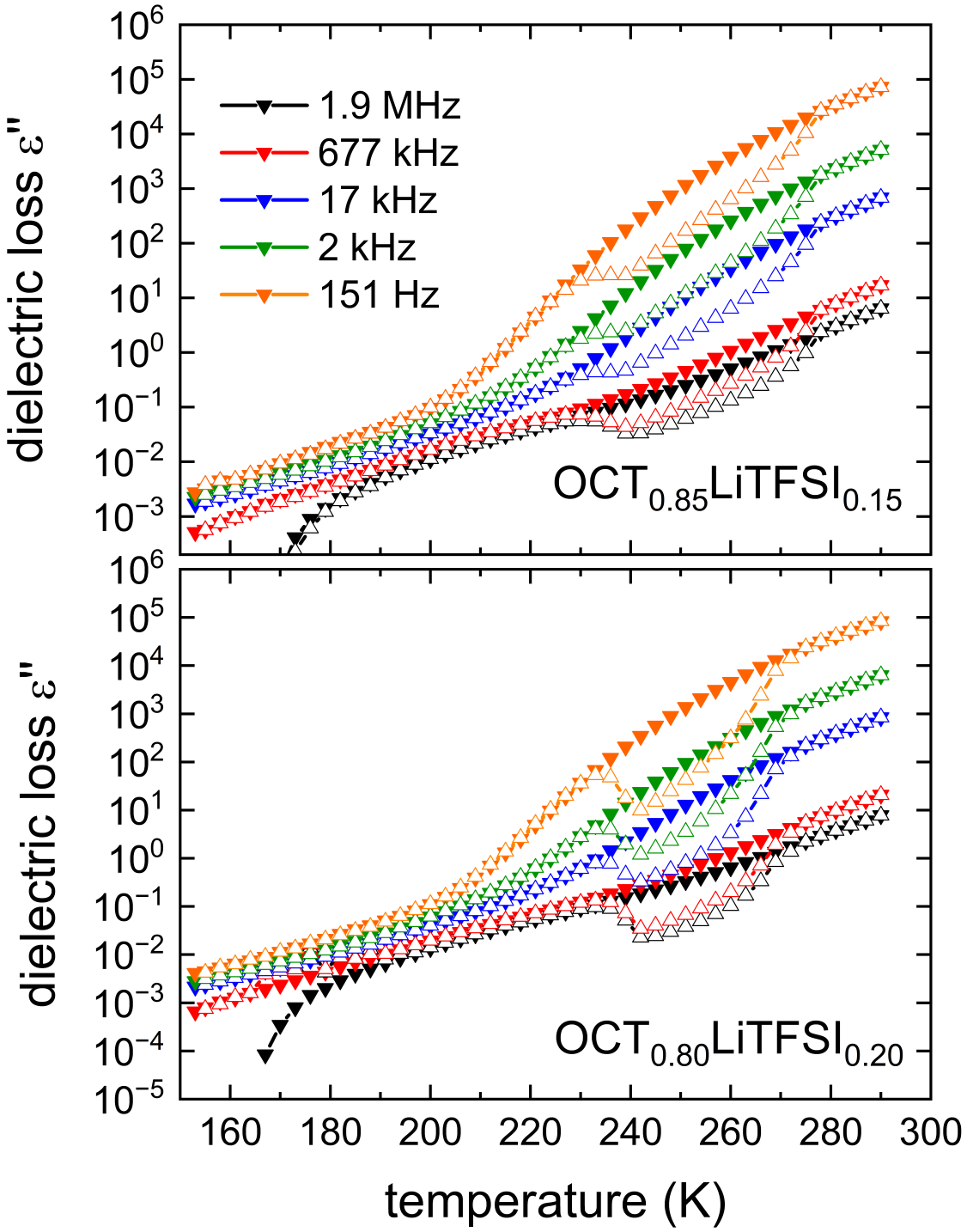

Figure 7.45: Temperature dependent dielectric loss across various frequencies of (a) $OCT_{0.85}LiTFSI_{0.15}$ and (b) $OCT_{0.80}LiTFSI_{0.20}$. Measurements were conducted during cooling (solid triangles pointing down) or heating (open triangles pointing up). The lines are drawn to guide the eye.

7.2.3 Discussion of transport and reorientation

In this section, we further explore the conductivity and dynamics of cycloalcohol mixtures based on the dielectric and NMR data previously presented. Figure 7.46 illustrates the phase transitions observed in the dielectric loss ϵ'' for $HEX_{0.6}OCT_{0.4}$ doped with various concentrations of LiTFSI, plotted against the Li concentration. The figure includes transition temperatures observed during both cooling T_f and heating T_m of the samples.

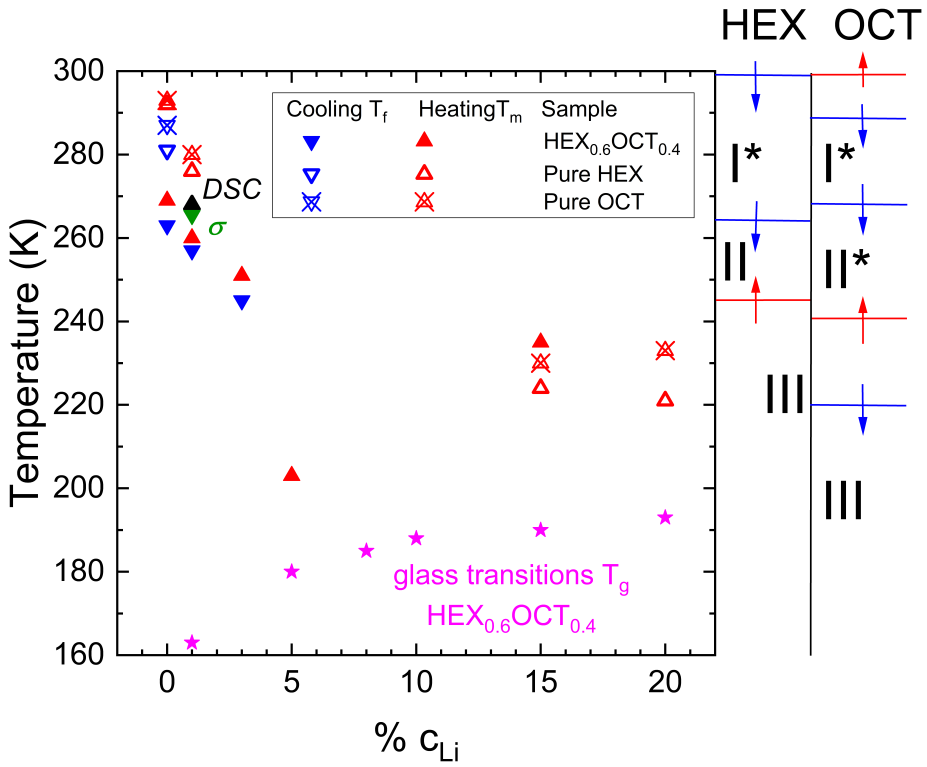

Figure 7.46: Phase diagram of Li-doped $HEX_{0.6}OCT_{0.4}$ based on the transitions observed in the dielectric loss ϵ''. Upward-pointing triangles denote the freezing temperature (T_f), while downward-pointing triangles represent the melting temperature (T_m). Transition temperatures for pure HEX or pure OCT are indicated by empty and crossed triangles, respectively. The filled black and green triangles correspond to transition temperatures reported in ref.[80] for $HEX_{0.6}OCT_{0.4}$ doped with 1% $LiPF_6$ detected by means of DSC or observed in the conductivity σ, respectively. Phase reported for HEX or OCT in refs.[79, 83] are indicated at the left axis of the figure. The PC phases are denoted by an asterisk (*). Glass transition temperatures were determined from the dielectric relaxation times based on $T = T_g \rightarrow \tau = 100$ s, refer to Appendix C.

Additionally, transition temperatures to the first orientationally disordered plastic crystalline phase (I*), as reported by Reuter et al. [80] in DSC for pure HEX and pure OCT, are incorporated. Additional transitions are indicated along the left axis of the figure, with the PC phases denoted by an asterisk (*). Moreover, phase transitions reported by the same

authors for $HEX_{0.6}OCT_{0.4}$ doped with 1% $LiPF_6$, observed in the conductivity data σ, are indicated by filled black and green triangles, respectively. We include in our figure as well, the glass transitions obtained from the dielectric relaxation times based on $T = T_g \rightarrow \tau = 100$ s, see Figure 7.48.

Upon closer examination of the phase transitions in the undoped samples, it becomes evident that the introduction of HEX with OCT significantly lowers the transition temperature to the plastic crystalline phase, occurring at approximately 263 K. Following the addition of 1% LiTFSI, this transition experiences a slight reduction of a few Kelvins, reaching 258 K. This value closely approximates that reported for the same mixture doped with 1% $LiPF_6$.[80] Further doping with Li salt results in a continuous reduction of the phase transition as evidenced by the melting temperatures. This reduction in T_m is accompanied by an increase in the glass transition temperatures. Similar observations were made regarding the T_g of glutaronitrile doped with high concentrations of LiTFSI.[165]

Furthermore, Figures 7.47(a) and (b) illustrate the Arrhenius plots of the DC conductivity for $HEX_{0.6}OCT_{0.4}$ and pure cycloalcohols doped with various LiTFSI concentrations, respectively. In frame (a), we include the ionic conductivity reported for $HEX_{0.4}OCT_{0.6}$ doped with 1% $LiPF_6$, and in frame (b), that reported for pure HEX and pure OCT, both doped with 1% $LiPF_6$.[80]

Considering the ionic conductivity of the cycloalcohol mixture in Figure 7.47(a), one can observe that the addition of only 1% LiTFSI results in an increase of approximately three orders of magnitude. At this Li salt concentration, a comparison between the ionic conductivity of doped $HEX_{0.6}OCT_{0.4}$ and $HEX_{0.4}OCT_{0.6}$ reveals slightly higher values for the latter mixture. This effect could be attributed to either better conductivity through 1% $LiPF_6$ doping or a smaller amount of OCT. Noteworthy, the phase transition observed in undoped $HEX_{0.6}OCT_{0.4}$ at 260 K, and appearing around 254 K in $HEX_{0.6}OCT_{0.4}$ doped with 1% LiTFSI, is not observed in $HEX_{0.4}OCT_{0.6}$ doped with 1% $LiPF_6$.

Moreover, higher doping concentrations than 1% lead to only a slight increase of about one order of magnitude, suggesting that the concentration optimum for the highest ionic conductivity lies around 3%. At these doping concentrations, the phase transition is slightly discernible in the conductivity data of the 3% before completely disappearing for higher concentrations.

Taking a closer look at the ionic conductivity measured for doped pure HEX and pure OCT in Figure 7.47(b), one can distinguish that the optimum conductivity previously measured for $HEX_{0.6}OCT_{0.4}$ doped with 3% LiTFSI and higher is already achieved by simply doping pure HEX with 1% $LiPF_6$. Pure OCT doped with 1% $LiPF_6$ on the other hand, exhibits a one order of magnitude lower conductivity with an apparent phase transition around 263 K. Higher doping concentrations at 15 and 20% LiTFSI of both pure HEX and pure OCT lead to conductivities close to the optimal one measured for pure HEX doped with 1% $LiPF_6$. Interestingly, this latter mixture, compared to the other samples, demonstrates an Arrhenius behavior in its temperature dependency of ionic conductivity, instead of the VFT behavior typically expected for plastic crystals and observed for the dinitrile mixtures.

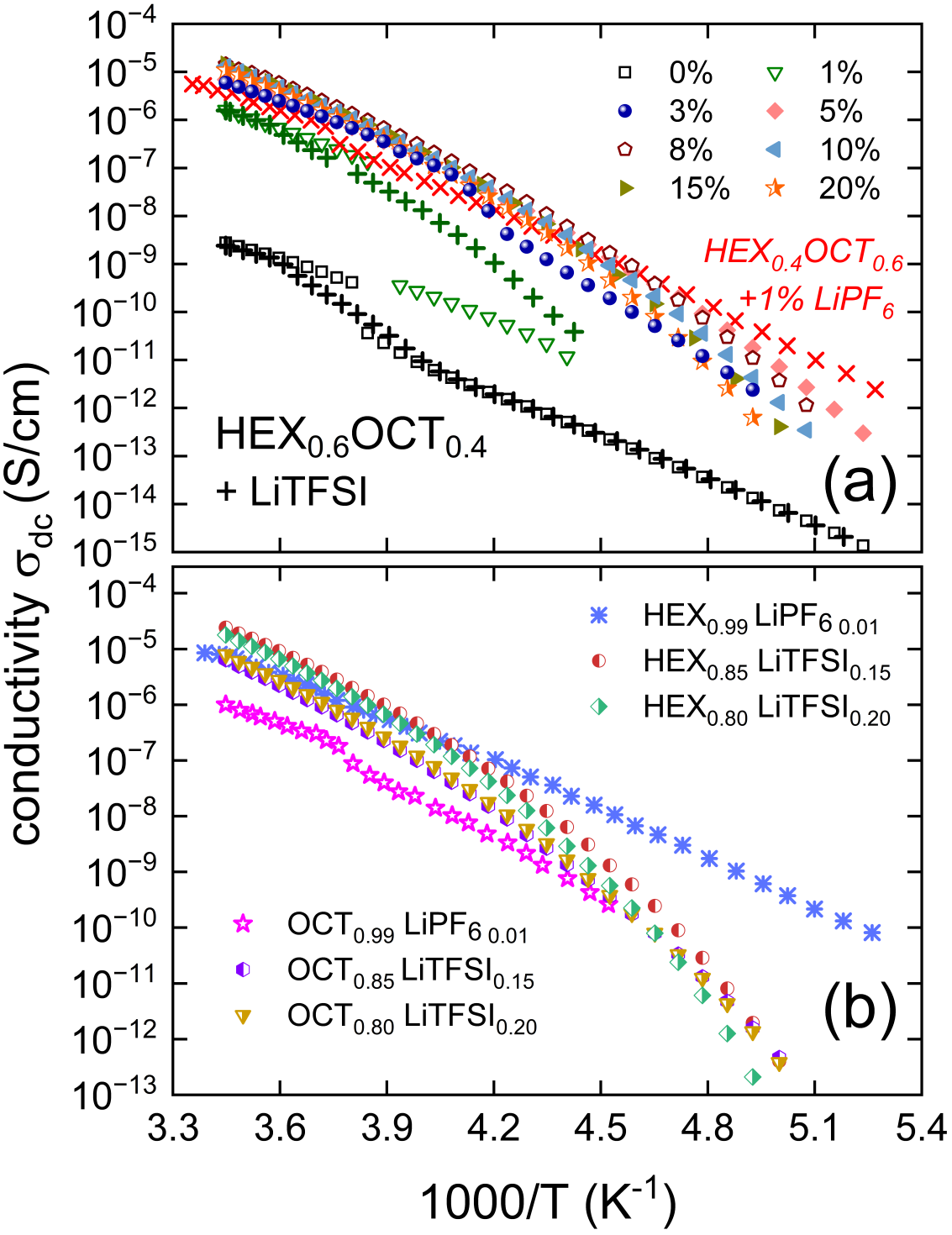

Figure 7.47: Arrhenius plot of the temperature-dependent conductivity of (a) $HEX_{0.6}OCT_{0.4}$ doped with different concentrations of LiTFSI (b) pure HEX or OCT doped with $LiPF_6$ or LiTFSI. The black and green plusses (+) in frame (a) refer to data measured after quenching the sample. The red crosses (×) represent data reported in ref.[80] for $HEX_{0.6}OCT_{0.4}$ doped with 1% $LiPF_6$. In frame (b) data for $HEX_{0.99}LiPF6_{0.01}$ and $OCT_{0.99}LiPF6_{0.01}$ were taken from ref.[80].

We now investigate the reorientational behavior of the cycloalcohol matrix and Li ions, as depicted in Figure 7.48, which presents the Arrhenius plot showing the reorientational relaxation time of all the investigated cycloalcohol samples in this work. Additionally, we incorporate the dielectric relaxation constants reported by Reuter et al.[80] for $HEX_{0.4}OCT_{0.6}$ doped with 1% LiTFSI. Furthermore, for better comparison with the dinitrile system discussed in Section 7.1.4, we include the VFT fit describing the reorientational behavior of the SN-GN matrix as well as that obtained for the HEX-OCT mixtures. The fit parameters are reported in Appendix C. We also include in Figure 7.48 the correlation times accessed through NMR for $HEX_{0.6}OCT_{0.4}$ doped with 5% LiTFSI.

By examining the data obtained for the $HEX_{0.6}OCT_{0.4}$ mixture both before and after doping with Li salt, two distinct dynamic regimes can be identified: The first regime, characterized by faster dynamics, describes the reorientational motion of the cycloalcohols in the undoped sample and in samples doped with Li salt concentrations up to 3%. In contrast, a second, much slower regime is observed, where the dynamics of the $HEX_{0.6}OCT_{0.4}$ mixture doped with Li salt concentrations higher than 3%, as well as those of HEX or OCT doped with high LiTFSI concentration, are effectively described.

The observed change in dynamic behavior at a 3% limit is consistent with prior postulations regarding the optimum concentration of Li salt. Specifically, at Li salt concentrations equal to or below 3%, the addition of Li ions enhances overall ionic conductivity without disrupting the rapid reorientational dynamics of the cycloalcohol molecules. However, at higher Li salt concentrations, although no significant decrease in ionic conductivity is detected, a notable reduction in the reorientational dynamics of the matrix becomes apparent.

Moreover, the decrease in the reorientational dynamics of samples doped with high Li concentrations (> 3%) does not necessarily result in a decrease in the overall ionic conductivity. This suggests a decoupling between the matrix dynamics and that of the charge carrier. However, this decoupling appears to be true only for samples doped with 3% Li salt or higher. Indeed, correlation times obtained through NMR for $HEX_{0.6}OCT_{0.4}$ doped with 5% LiTFSI align well with the VFT fit describing the fast reorientational regime. This suggests that the charge carrier is consistently well-coupled to the matrix dynamics following the fast reorientational regime. Such an observation explains why the ionic conductivity of samples doped with Li salt concentrations higher than 3% remains constant even though the reorientational motion of the cycloalcohol molecules is much slower.

Taking into account the above observations, the transport mechanism in doped cycloalcohols can be explained as follows: At lower Li salt concentrations ($\geq$ 3%), the temperature-dependence of the reorientational times of the HEX-OCT matrix mirrors that of the Li ion motion. In this scenario, the increase in ionic conductivity can be attributed to the rise in charge carrier density. Conversely, at higher Li salt concentrations (> 3%), the translational motion of the Li ions remains unchanged, maintaining the ionic conductivity. However, the reorientational dynamics of the HEX-OCT matrix slow down significantly due to the increased amount of Li salt. This scenario aligns well with the ”revolving-door” mechanism, where a similar temperature dependence of the matrix and charge carrier is expected, as

it is the case for samples doped with lower Li salt (> 3%). Unlike the paddle-wheel mechanism, the revolving-door mechanism does not require sufficient free volume. Therefore, even at higher Li salt concentrations and despite the slower matrix dynamics, the optimal conductivity remains achievable as long as the reorientational motion of the cycloalcohols is efficient with respect to charge transport. In other words, there are still sufficient "doors" that open for an effective charge transport. These findings are consistent with those of Reuter *et al.*[80], who reported a revolving-door mechanism in doped HEX-OCT mixtures, with little influence observed from the mixing ratio.

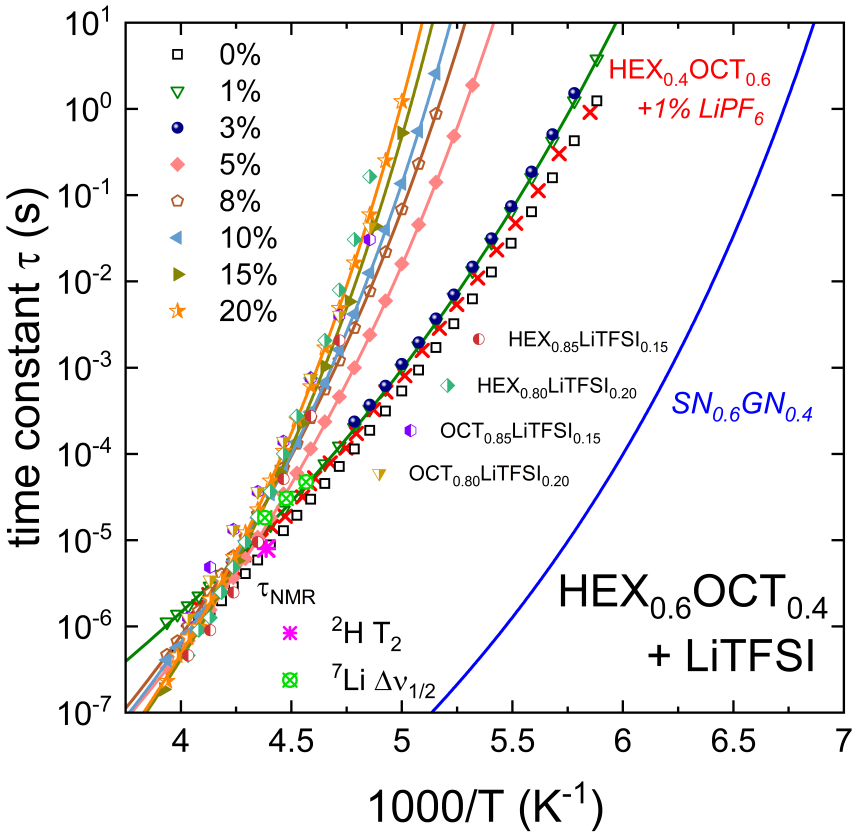

Figure 7.48: Arrhenius plot of the reorientational relaxation time of $HEX_{0.6}OCT_{0.4}$ doped with different concentrations of LiTFSI. Data for pure HEX or OCT doped with 15% or 20% LiTFSI is included. The red crosses (×) represent data reported in ref.[80] for $HEX_{0.6}OCT_{0.4}$ doped with 1% $LiPF_6$. Solid lines are VFT fits with the parameters mentioned in Appendix C. The solid blue line corresponds to the previously discussed VFT fit for $SN_{0.6}GN_{0.4}$, provided for comparison.

8 Conclusion

In this work, we conducted a thorough investigation of two types of plastic crystals using a combination of dielectric spectroscopy, NMR, and rheology techniques. Our analysis focused on a dinitrile plastic crystal composed of a mixture of succinonitrile (SN) and glutaronitrile (GN), revealing a strong coupling between the matrix's reorientation motion and the translational dynamics of the added Li ions. Indeed, our comparison of conductivity data obtained from dielectric spectroscopy with that derived from diffusion ^{7}Li NMR or viscosity measurements yielded consistent results. Notably, we observed a pronounced correlation between the timescales governing the SN-GN matrix motion and the charge carrier's dynamics, indicating a paddle-wheel mechanism. This dynamic coupling remained unaffected by variations in the type or concentration of Li salt within the mixture, at least up to the optimal Li-salt concentration of approximately 5%.

Furthermore, our comparative analysis of the SN-GN data collected in this study and existing literature suggests a plausible connection between volume defects within the SN matrix and the effectiveness of the paddle-wheel mechanism.

The second plastic crystal investigated was a mixture of cyclohexanol (HEX) and cyclooctanol (OCT). Unlike the dinitrile plastic crystal, this mixture exhibits a different type of coupling between the host matrix and the charge carrier. Comparison of the ionic conductivities and time scales describing the reorientational motion of the cycloalcohol molecules revealed similar values and temperature dependencies up to the concentration optimum of approximately 3%. At higher doping concentrations, the ionic conductivity remained optimal, although the matrix dynamics became significantly slower. This was found also true for highly Li doped HEX or OCT. We attribute such observations to the revolving door mechanism.

As compared to previous findings, our research offeres additional insights into the dynamic coupling occurring in mixtures of dinitriles and cycloalcohols. Our study underscores the disparities in charge transport between these two plastic crystals and presents compelling arguments for interpreting dynamic correlations. We believe that conducting additional structural investigations on both mixtures could provide deeper insights into the charge transport within these plastic electrolytes. Exploring the variances in structural configurations between the paddle-wheel and revolving-door mechanisms would be particularly intriguing. Such investigations could elucidate the underlying reasons behind the volume effect observed in the paddle-wheel mechanism in the dinitrile mixtures. Similarly, in the case of the revolving-door mechanism, such inquiries could shed light on the conditions under which the efficacy of the revolving doors is compromised. For instance, one approach

to such investigations could involve varying the size of the cations or replacing one of the constituent host molecules with a static and immobile counterpart.

A Dynamic model for the stimulated echo experiment

To analyze and interpret the ^{2}H STE experiments carried out on the $(SN\text{-}d_4)_{0.6}(GN)_{0.4}$ sample, we formulated a model grounded in the isomeric characteristics of the SN molecule. The dynamic model was conceptualized together with *Dr. Joachim Beerwerth*, who also executed the simulation work. Random Walk simulations were employed to calculate the final-state amplitudes,[170] in conjuction with the Euler angles corresponding to twelve equilibrium orientations of the C-D bound (see below). General information regarding Random Walk simulations is documented in Beerwerth's and Schildmann's PhD theses.[171, 172]

In Figure A.1, the directional vector of the C-D bond in SN-d_4 is depicted, based on the isomeric behavior described in Section 2.1. Each color corresponds to a C-D bond with its three equilibrium positions, obtained through a 120° rotation about the four threefold axes. Since NMR is sensitive only to magnetic non-equivalent positions, only half of the equilibrium positions shown in Figure A.1 are actually NMR relevant.

In addition to Euler angles, we consider the first-order quadrupolar interactions and assume equal population and identical EFG parameters for all sites. The results, illustrating the ratio between the experimentally determined lifetime (τ_c, see Figure 7.11) and the set lifetime value ($\tau_{\text{fixed}} = 1$ ms) for simulation, along with the final-state amplitudes Z as a function of the evolution time t_p are presented in Figures A.2(a) and (b), respectively.

Both the ratio of the lifetime and the final state correlation remain independent with respect to the evolution time. However, this observation contradicts the experimental results that demonstrate a clear correlation between t_p and τ_c (see Section 7.1.1). Therefore, additional assumptions regarding the dynamic model of SN are necessary. We propose introducing additional dynamic disorder by assuming that the vector pointing upwards (represented by the stretched black arrow) is slightly tilted by an angle α with respect to the (001) vector, enabling it to move freely around the base of a cone. Notably, this movement is faster than the reorientational motion of the C-D bond. The results for various angles α are presented in Figures A.3 and A.4.

A careful examination of Figure A.3 reveals a clear dependence on t_p in the $\tau_c/\tau_{\text{fixed}}$ ratio. The rate at which this ratio decays becomes more pronounced as the angle α increases. Conversely, the final state correlation, as depicted in Figure A.4 for $\alpha = 1°$, $3°$ and $5°$, does not exhibit a strong dependence on the angle α. Indeed, at low evolution times, Z displays consistent behavior regardless of the angle α, with slight variations emerging at higher evolution times.

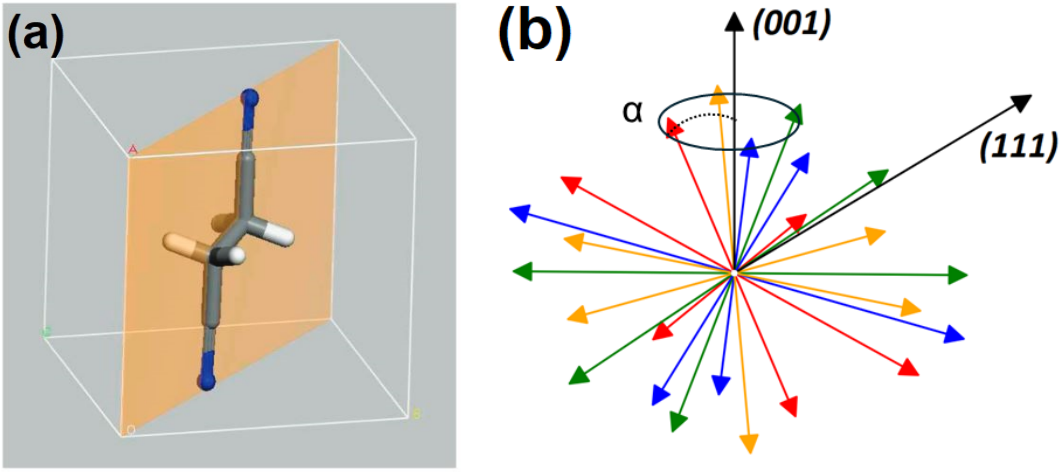

Figure A.1: (a) SN molecule in the *trans* conformation within the unit cell as published in ref.[173]. (b) Possible orientations of the C-D bonds deduced from the isomeric behavior of the SN molecule. α is the angle between the vector pointing upwards (represented by the stretched black arrow) and the (001) vector. Consequently, the C-D arrows are also tilted by angle α from their original positions.

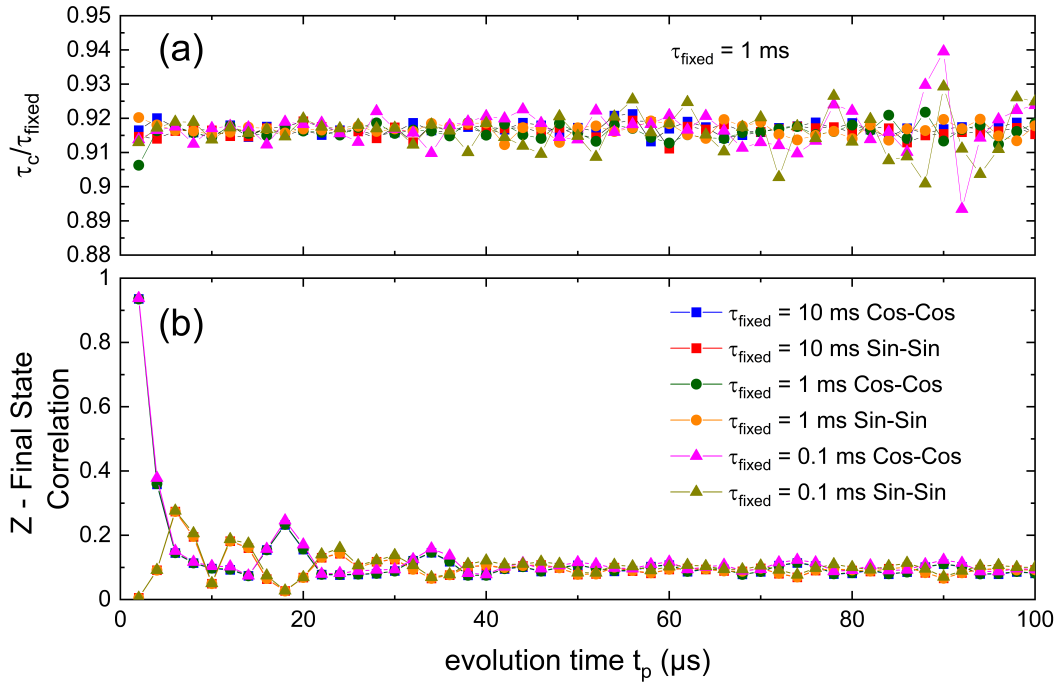

Figure A.2: (a) Ratio of measured and simulated lifetimes (τ_c/τ_{fixed}) and (b) Final state correlation Z obtained through simulation. The lifetime values were either acquired by experimental measurements or set for simulations of three pulses cos-cos (solid lines) or sin-sin (dashed lines) ^{2}H STE experiment on $(SN\text{-}d_4)_{0.6}(GN)_{0.4}$. The simulation experiments were based on the dynamic model described in the text for $\alpha = 0$.

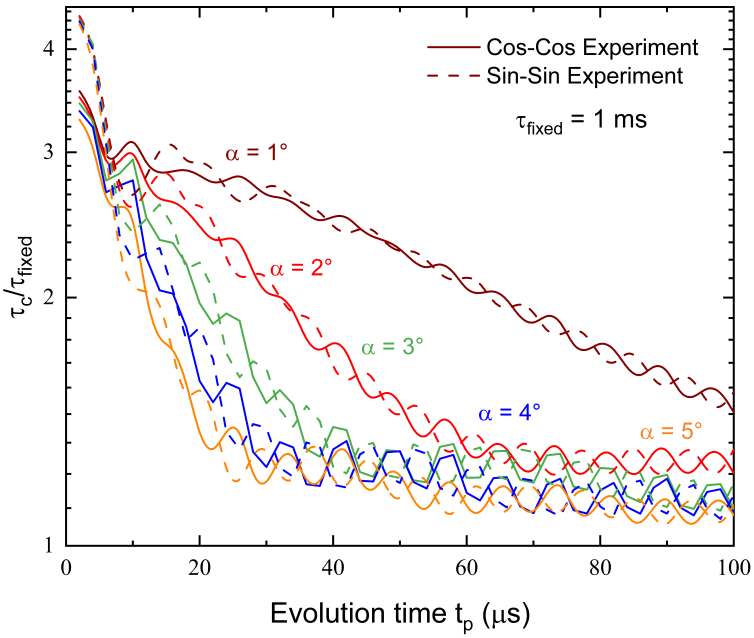

Figure A.3: Ratio of measured and simulated lifetimes (τ_c/τ_{fixed}). The lifetime values were either acquired by experimental measurements or set for simulations of three pulses cos-cos (solid lines) or sin-sin (dashed lines) ^{2}H STE experiment on $(SN\text{-}d_4)_{0.6}(GN)_{0.4}$. The simulation experiments were based on the dynamic model described in the text for angles α between 1° and 5°.

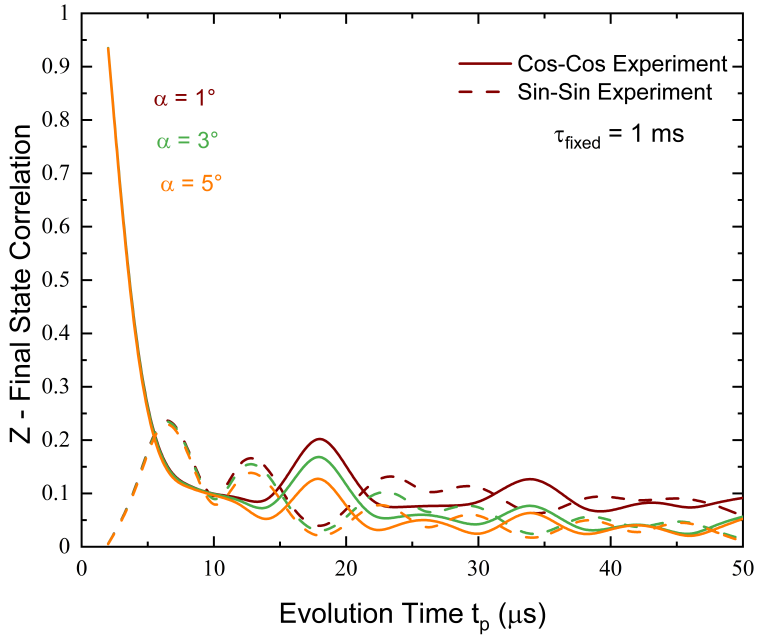

Figure A.4: Final state correlation Z obtained by simulating cos-cos (solid lines) or sin-sin (dashed lines) ^{2}H STE experiment on $(SN\text{-}d_4)_{0.6}(GN)_{0.4}$.

B Dielectric spectroscopy measurements on doped $HEX_{0.6}OCT_{0.4}$

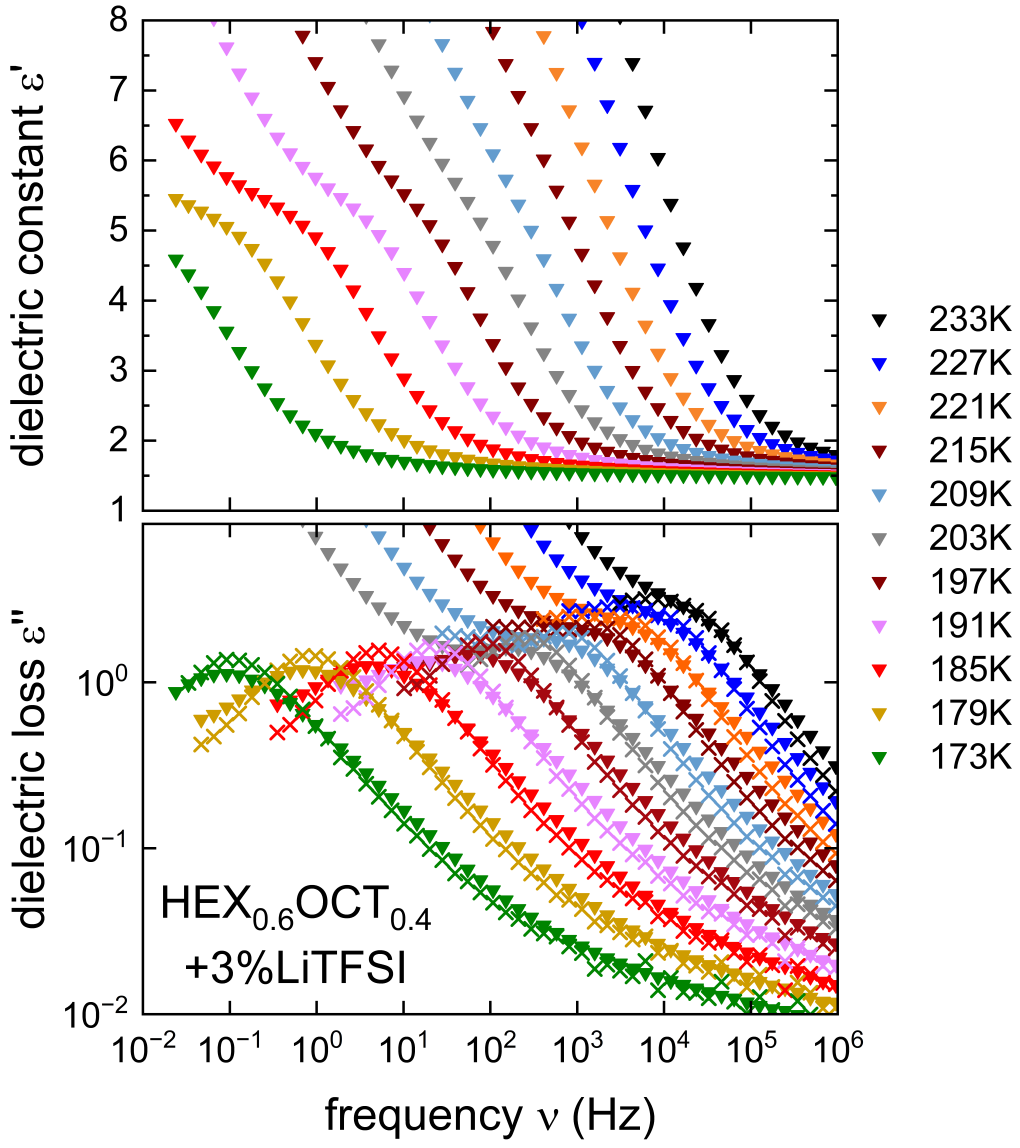

Figure B.1: Frequency dependent measurements of (a) the real part and (b) the imaginary part of the complex dielectric permittivity of $HEX_{0.6}OCT_{0.4}$ doped with 3%LiTFSI. The crosses (×) in frame (b) are derived from the dielectric constant ϵ' according to Eq. (5.10). The measurements were conducted during cooling.

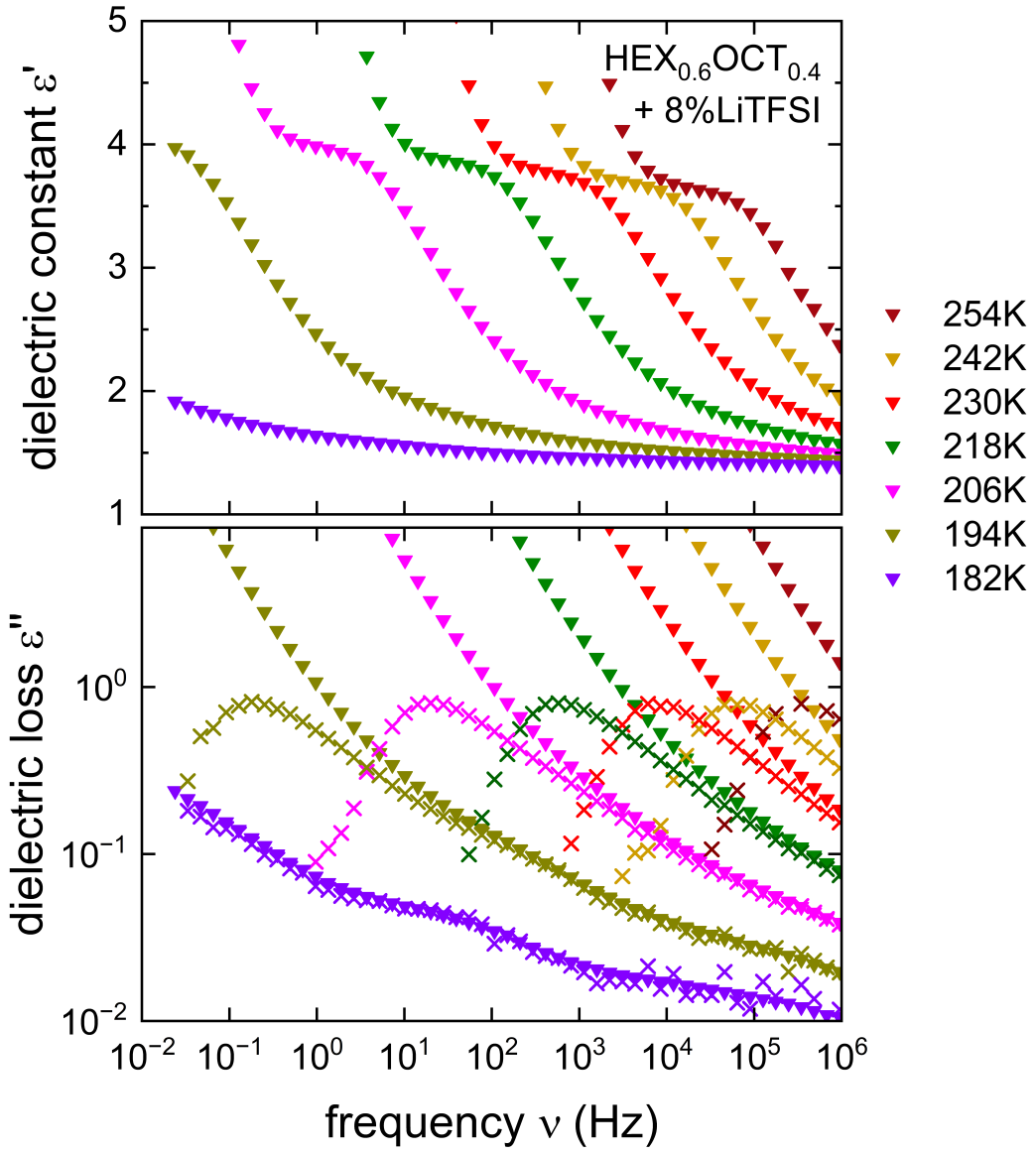

Figure B.2: Frequency dependent measurements of (a) the real part and (b) the imaginary part of the complex dielectric permittivity of $HEX_{0.6}OCT_{0.4}$ doped with 8%LiTFSI. The crosses (×) in frame (b) are derived from the dielectric constant ϵ' according to Eq. (5.10). The measurements were conducted during cooling.

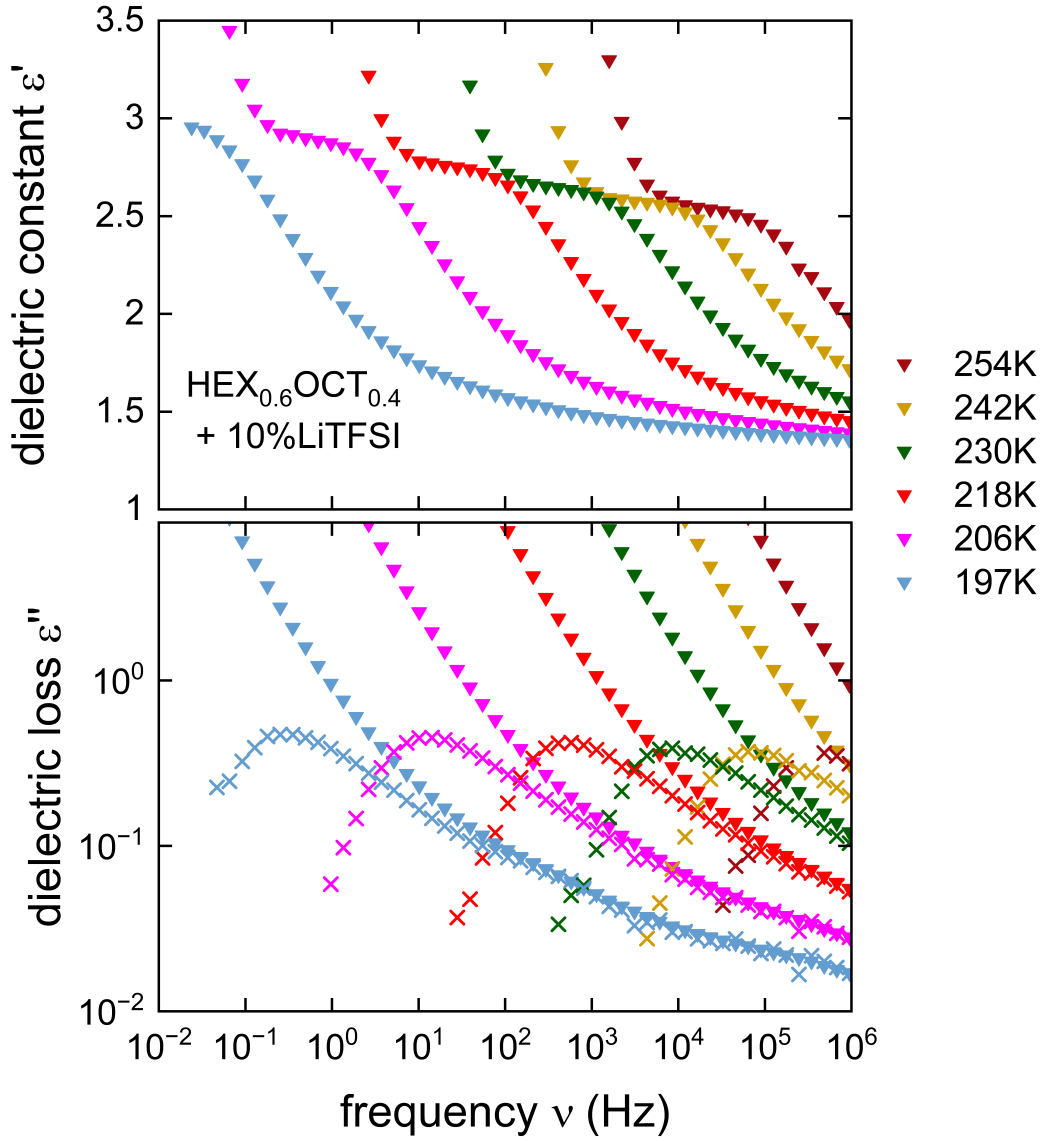

Figure B.3: Frequency dependent measurements of (a) the real part and (b) the imaginary part of the complex dielectric permittivity of $HEX_{0.6}OCT_{0.4}$ doped with 10%LiTFSI. The crosses (×) in frame (b) are derived from the dielectric constant ϵ' according to Eq. (5.10). The measurements were conducted during cooling.

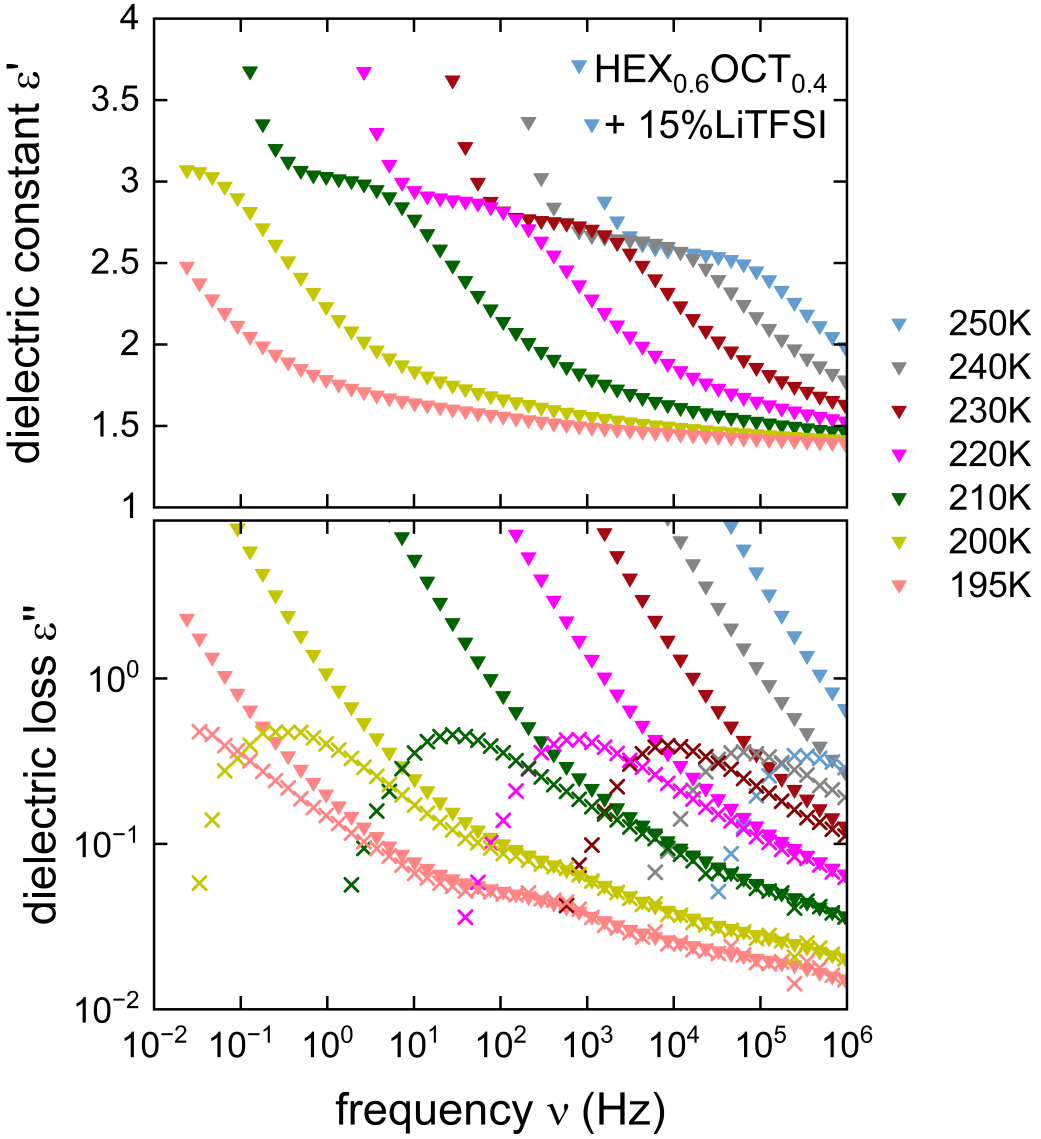

Figure B.4: Frequency dependent measurements of (a) the real part and (b) the imaginary part of the complex dielectric permittivity of $HEX_{0.6}OCT_{0.4}$ doped with 15%LiTFSI. The crosses (×) in frame (b) are derived from the dielectric constant ϵ' according to Eq. (5.10). The measurements were conducted during cooling.

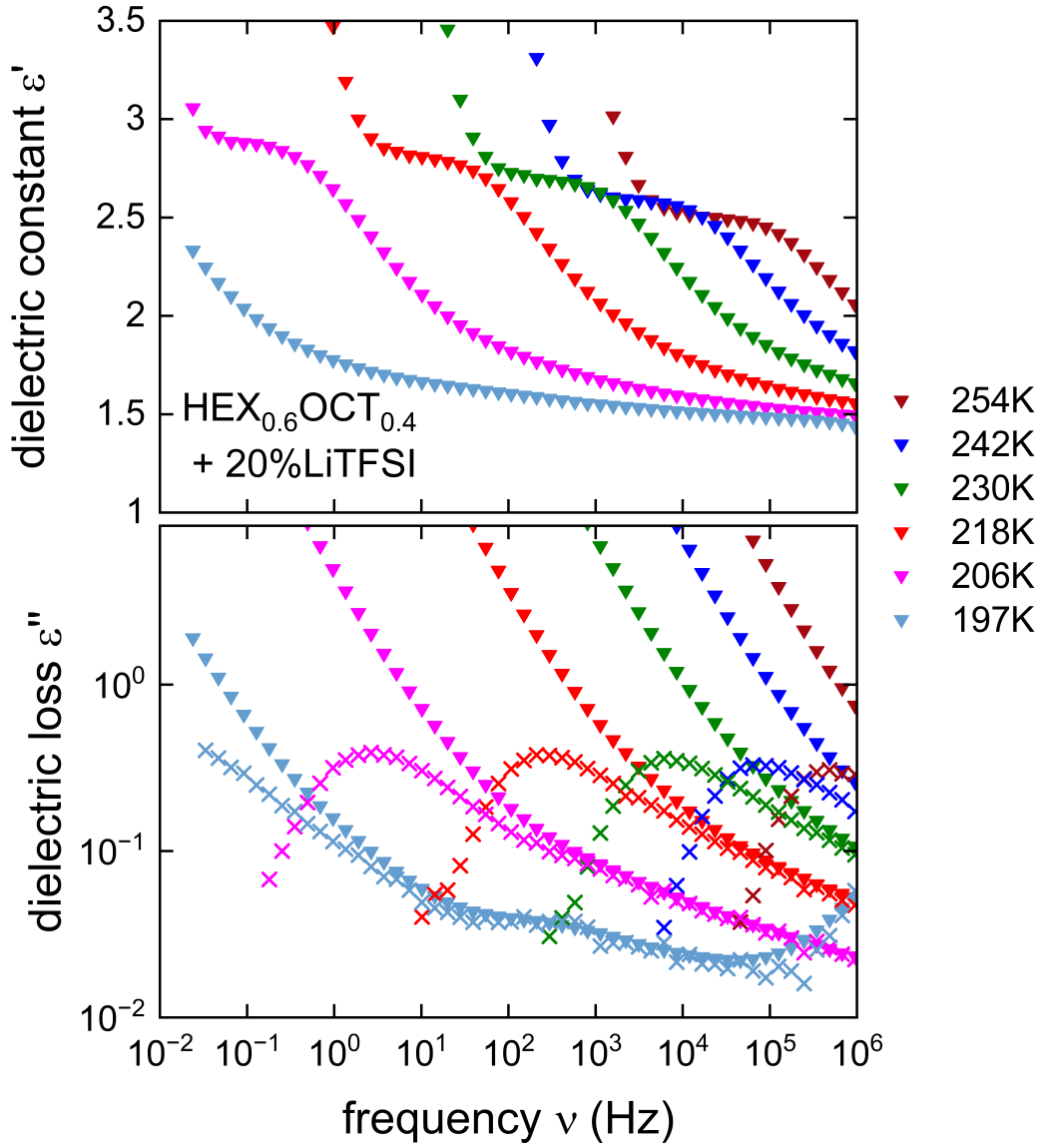

Figure B.5: Frequency dependent measurements of (a) the real part and (b) the imaginary part of the complex dielectric permittivity of $HEX_{0.6}OCT_{0.4}$ doped with 20%LiTFSI. The crosses (×) in frame (b) are derived from the dielectric constant ϵ' according to Eq. (5.10). The measurements were conducted during cooling.

C Vogel-Fulcher-Tammann fit parameters for doped $HEX_{0.6}OCT_{0.4}$

Sample	τ_∞ (s)	D_τ	T_τ (K)	T_g (K)
1 %	2.7×10^{-12}	20.3	98	163
5 %	6.2×10^{-14}	16.6	122	180
8 %	9.6×10^{-14}	14.7	130	185
10 %	1.6×10^{-13}	12.8	137	188
15 %	2.2×10^{-14}	13.2	140	190
20 %	2.2×10^{-14}	12.7	143	193

Table C.1: Vogel-Fulcher-Tammann fit parameters (see Eq. (3.2)) of the reorientational relaxation time for doped $HEX_{0.6}OCT_{0.4}$. The glass transition temperature were determined from the dielectric relaxation times based on $T = T_g \rightarrow \tau = 100$ s.

Bibliography

[1] IEA. *Innovation in Batteries and Electricity Storage: A global analysis based on patent data.* Tech. rep. 2020.

[2] D. Manz, R. Piwko, and N. Miller. "Look Before You Leap: The Role of Energy Storage in the Grid." In: *IEEE Power and Energy Magazine* 10 (2012), pp. 75–84.

[3] B. Dunn, H. Kamath, and J-M. Tarascon. "Electrical Energy Storage for the Grid: A Battery of Choices." In: *Science* 334 (2011), pp. 928–935.

[4] J. B. Goodenough and K-S. Park. "The Li-Ion Rechargeable Battery: A Perspective." In: *J. Am. Chem. Soc.* 135 (2013), pp. 1167–1176.

[5] D. Larcher and J-M. Tarascon. "Towards greener and more sustainable batteries for electrical energy storage." In: *Nat. Chem.* 7 (2014), pp. 19–29.

[6] K. Xu. "Electrolytes and Interphases in Li-Ion Batteries and Beyond." In: *Chem. Rev.* 114 (2014), pp. 11503–11618.

[7] N. Nitta, F. Wu, J. Tae Lee, and G. Yushin. "Li-ion battery materials: present and future." In: *Mater Today* 18 (2015), pp. 252–264.

[8] M. Li, J. Lu, Z. Chen, and K. Amine. "30 Years of Lithium-Ion Batteries." In: *Adv. Mater.* 30 (2018), p. 1800561.

[9] J. B. Goodenough and Y. Kim. "Challenges for Rechargeable Li Batteries." In: *Chem. Mater.* 22 (2010), pp. 587–603.

[10] V. Etacheri, R. Marom, R. Elazari, G. Salitra, and D. Aurbach. "Challenges in the development of advanced Li-ion batteries: a review." In: *Energy Environ. Sci.* 4 (2011), pp. 3243–3262.

[11] P. Albertus, S. Babinec, S. Litzelman, and A. Newman. "Status and challenges in enabling the lithium metal electrode for high-energy and low-cost rechargeable batteries." In: *Nat. Energy* 3 (2017), pp. 16–21.

[12] J. Kalhoff, G. G. Eshetu, D. Bresser, and S. Passerini. "Safer Electrolytes for Lithium-Ion Batteries: State of the Art and Perspectives." In: *ChemSusChem* 8 (2015), pp. 2154–2175.

[13] W. Zhao, J. Yi, P. He, and H. Zhou. "Solid-State Electrolytes for Lithium-Ion Batteries: Fundamentals, Challenges and Perspectives." In: *Electrochem. Energ. Rev.* 2 (2019), pp. 574–605.

[14] Y-K. Liu, C-Z. Zhao, J. Du, X-Q. Zhang, A-B. Chen, and Q. Zhang. "Research Progresses of Liquid Electrolytes in Lithium-Ion Batteries." In: *Small* 19 (2023), p. 2205315.

[15] M. Keller, A. Varzi, and S. Passerini. "Hybrid electrolytes for lithium metal batteries." In: *J. Power Sources* 392 (2018), pp. 206–225.

[16] S. E. Sloop, J. B. Kerr, and K. Kinoshita. "The role of Li-ion battery electrolyte reactivity in performance decline and self-discharge." In: *J. Power Sources* 119–121 (2003), pp. 330–337.

[17] L. O. Valøen and J. N. Reimers. "Transport Properties of LiPF[sub 6]-Based Li-Ion Battery Electrolytes." In: *J. Electrochem. Soc.* 152 (2005), A882.

[18] S. Long, D. R. MacFarlane, and M. Forsyth. "Fast ion conduction in molecular plastic crystals." In: *Solid State Ion.* 161 (2003), pp. 105–112.

[19] P.-J. Alarco, Y. Abu-Lebdeh, A. Abouimrane, and M. Armand. "The plastic-crystalline phase of succinonitrile as a universal matrix for solid-state ionic conductors." In: *Nat. Mater.* 3 (2004), pp. 476–481.

[20] A. Abouimrane and I. J. Davidson. "Solid electrolyte based on succinonitrile and LiBOB: interface stability and application in lithium batteries." In: *J. Electrochem. Soc.* 154 (2007), A1031.

[21] A. Abouimrane, P. S. Whitfield, S. Niketic, and I.J. Davidson. "Investigation of Li salt doped succinonitrile as potential solid electrolytes for lithium batteries." In: *J. Power Sources* 174 (2007), pp. 883–888.

[22] L.-Z. Fan, Y.-S. Hu, A. J. Bhattacharyya, and J. Maier. "Succinonitrile as a Versatile Additive for Polymer Electrolytes." In: *Adv. Funct. Mater.* 17 (2007), pp. 2800–2807.

[23] Y. Abu-Lebdeh and I. Davidson. "High-Voltage Electrolytes Based on Adiponitrile for Li-Ion Batteries." In: *J. Electrochem. Soc.* 156 (2009), A60.

[24] G. P. Pandey, T. Liu, C. Hancock, Y. Li, X. S. Sun, and J. Li. "Thermostable gel polymer electrolyte based on succinonitrile and ionic liquid for high-performance solid-state supercapacitors." In: *J. Power Sources* 328 (2016), pp. 510–519.

[25] D. Farhat, J. Maibach, H. Eriksson, K. Edström, D. Lemordant, and F. Ghamouss. "Towards high-voltage Li-ion batteries: Reversible cycling of graphite anodes and Li-ion batteries in adiponitrile-based electrolytes." In: *Electrochim. Acta.* 281 (2018), pp. 299–311.

[26] J. Villarreal, R. Orrostieta Chavez, S. A. Chopade, T. P. Lodge, and M. Alcoutlabi. "The Use of Succinonitrile as an Electrolyte Additive for Composite-Fiber Membranes in Lithium-Ion Batteries." In: *Membranes* 10 (2020), p. 45.

[27] J. Möller, V. van Laack, K. Koschek, P. Bottke, and M. Wark. "Solid-State NMR Revealing the Impact of Polymer Additives on Li-Ion Motions in Plastic-Crystalline Succinonitrile Electrolytes." In: *J. Phys. Chem. C* 127 (2023), pp. 1464–1474.

[28] D. Farhat, D. Lemordant, J. Jacquemin, and F. Ghamouss. "Alternative Electrolytes for Li-Ion Batteries Using Glutaronitrile and 2-methylglutaronitrile with Lithium Bis(trifluoromethanesulfonyl) Imide." In: *J. Electrochem. Soc.* 166 (2019), A3487–A3495.

[29] M. Yao, R. Pan, Y. Ren, Y. Fu, Y. Qin, C. Mao, Z. Zhang, X. Guo, and G. Li. "Regulating solvation shells and interfacial chemistry in zinc-ion batteries using glutaronitrile based electrolyte." In: *J. Mater. Chem. A* 10 (2022), pp. 14345–14354.

[30] N. Voigt and L. van Wüllen. "The effect of plastic-crystalline succinonitrile on the electrolyte system PEO:LiBF4: Insights from solid state NMR." In: *Solid State Ion.* 260 (2014), pp. 65–75.

[31] Th. Bauer, M. Köhler, P. Lunkenheimer, A. Loidl, and C. A. Angell. "Relaxation dynamics and ionic conductivity in a fragile plastic crystal." In: *J. Chem. Phys.* 133 (2010).

[32] M. Götz, Th. Bauer, P. Lunkenheimer, and A. Loidl. "Supercooled-liquid and plastic-crystalline state in succinonitrile-glutaronitrile mixtures." In: *J. Chem. Phys.* 140 (2014).

[33] M. Zachariah, M. Romanini, P. Tripathi, J. Ll. Tamarit, and R. Macovez. "Molecular diffusion and dc conductivity perfectly correlated with molecular rotational dynamics in a plastic crystalline electrolyte." In: *Phys. Chem. Chem. Phys.* 17 (2015), pp. 16053–16057.

[34] M. Zachariah, M. Romanini, P. Tripathi, M. Barrio, J. L. Tamarit, and R. Macovez. "Self-Diffusion, Phase Behavior, and Li+ Ion Conduction in Succinonitrile-Based Plastic Cocrystals." In: *J. Phys. Chem. C* 119 (2015), pp. 27298–27306.

[35] S. Davidowski, A. R. Young-Gonzales, R. Richert, and C. A. Yarger J.and Angell. "Relation of Ionic Conductivity to Solvent Rotation Times in Dinitrile Plastic Crystal Solvents." In: *J. Electrochem. Soc.* 167 (2020), p. 070553.

[36] S. K. Davidowski, J. L. Yarger, R. Richert, and C. A. Angell. "Reorientation Times for Solid-State Electrolyte Solvents and Electrolytes from NMR Spin–Lattice Relaxation Studies." In: *J. Phys. Chem. Letters* 11 (2020), pp. 3301–3304.

[37] P. Derollez, J. Lefebvre, M. Descamps, W. Press, and H. Fontaine. "Structure of succinonitrile in its plastic phase." In: *J. Phys. Condens. Matter* 2 (1990), pp. 6893–6903.

[38] C. A. Angell. "Relaxation in liquids, polymers and plastic crystals — strong/fragile patterns and problems." In: *J. Non Cryst. Solids.* 131–133 (1991), pp. 13–31.

[39] K. Geirhos, P. Lunkenheimer, M. Michl, D. Reuter, and A. Loidl. "Communication: Conductivity enhancement in plastic-crystalline solid-state electrolytes." In: *J. Chem. Phys.* 143 (2015), p. 081101.

[40] W. J. Orville-Thomas. "Tables of experimental dipole moments, vol. 2." In: *J. Mol. Struct.* 36 (1977), p. 165.

[41] Y. Ugata, M. L. Thomas, T. Mandai, K. Ueno, K. Dokko, and M. Watanabe. "Li-ion hopping conduction in highly concentrated lithium bis(fluorosulfonyl)amide/dinitrile liquid electrolytes." In: *Phys. Chem. Chem. Phys.* 21 (2019), pp. 9759–9768.

[42] Y. Ugata, R. Tatara, K. Ueno, K. Dokko, and M. Watanabe. "Highly concentrated LiN(SO2CF3)2/dinitrile electrolytes: Liquid structures, transport properties, and electrochemistry." In: *J. Chem. Phys.* 152 (2020), p. 104502.

[43] O. Borodin, J. Self, K. A. Persson, Ch. Wang, and K. Xu. "Uncharted Waters: Super-Concentrated Electrolytes." In: *Joule* 4 (2020), pp. 69–100.

[44] Y. Yamada, K. Furukawa, K. Sodeyama, K. Kikuchi, M. Yaegashi, Y. Tateyama, and A. Yamada. "Unusual Stability of Acetonitrile-Based Superconcentrated Electrolytes for Fast-Charging Lithium-Ion Batteries." In: *J. Am. Chem. Soc.* 136 (2014), pp. 5039–5046.

[45] Y. Yamada and A. Yamada. "Review—Superconcentrated Electrolytes for Lithium Batteries." In: *J. Electrochem. Soc.* 162 (2015), A2406–A2423.

[46] Y. Yamada, J. Wang, S. Ko, E. Watanabe, and A. Yamada. "Advances and issues in developing salt-concentrated battery electrolytes." In: *Nat. Energy* 4 (2019), pp. 269–280.

[47] J. Wang, Y. Yamada, K. Sodeyama, C. H. Chiang, Y. Tateyama, and A. Yamada. "Super-concentrated electrolytes for a high-voltage lithium-ion battery." In: *Nat. Commun.* 7 (2016), p. 12032.

[48] R. Böhmer, M. Storek, and M. Vogel. "NMR studies of ionic dynamics in solids." In: *Modern Methods in Solid-State NMR: A Practitioner's Guide* (2018), pp. 193–230.

[49] A. Kuhn, M. Kunze, P. Sreeraj, H.-D. Wiemhöfer, V. Thangadurai, M. Wilkening, and P. Heitjans. "NMR relaxometry as a versatile tool to study Li ion dynamics in potential battery materials." In: *Solid State Nucl. Magn. Reson.* 42 (2012), pp. 2–8.

[50] O. Pecher, J. Carretero-González, K. J. Griffith, and Clare P. Grey. "Materials' Methods: NMR in Battery Research." In: *Chem. Mater.* 29 (2016), pp. 213–242.

[51] C. P. Grey and N. Dupré. "NMR Studies of Cathode Materials for Lithium-Ion Rechargeable Batteries." In: *Chem. Rev.* 104 (2004), pp. 4493–4512.

[52] N. Dupre, M. Cuisinier, and D. Guyomard. "Electrode/Electrolyte Interface Studies in Lithium Batteries Using NMR." In: *Electrochem. Soc. Interface* 20 (2011), pp. 61–67.

[53] B. M. Meyer, N. Leifer, S. Sakamoto, S. G. Greenbaum, and C. P. Grey. "High Field Multinuclear NMR Investigation of the SEI Layer in Lithium Rechargeable Batteries." In: *Electrochem. Solid-State Lett.* 8 (2005), A145.

[54] J. Z. Hu, N. R. Jaegers, M. Y. Hu, and K. T. Mueller. "In situ and ex situ NMR for battery research." In: *J. Phys. Condens. Matter* 30 (2018), p. 463001.

[55] C. P. Grey and Y. J. Lee. "Lithium MAS NMR studies of cathode materials for lithium-ion batteries." In: *Solid State Sci.* 5 (2003), pp. 883–894.

[56] K. S. Han, J. D. Bazak, Y. Chen, T. R. Graham, N. M. Washton, J. Z. Hu, V. Murugesan, and K. T. Mueller. "Pulsed Field Gradient Nuclear Magnetic Resonance and Diffusion Analysis in Battery Research." In: *Chem. Mater.* 33 (2021), pp. 8562–8590.

[57] L. A. K. Staveley. "Phase Transitions in Plastic Crystals." In: *Annu. Rev. Phys. Chem.* 13 (1962), pp. 351–368.

[58] M. Descamps and G. Coulon. "Dielectric constant of disordered dipoles with steric hindrance." In: *Chem. Phys.* 19 (1977), pp. 347–352.

[59] J. N. Sherwood. *The Plastically crystalline state: orientationally disordered crystals.* John Wiley, 1979.

[60] C. A Wulff and Edgar F. Westrum Jr. "Heat capacities and thermodynamic properties of globular molecules. VI. Succinonitrile." In: *J. Phys. Chem.* 67 (1963), pp. 2376–2381.

[61] J. Timmermans. "Plastic crystals: A historical review." In: *J. Phys. Chem. Solids.* 18 (1961), pp. 1–8.

[62] G.W. Gray and P. A. Winsor. *Liquid Crystals & Plastic Crystals: Physico-chemical properties and methods of investigation.* Vol. 2. Ellis Horwood series in physical chemistry. E. Horwood, 1974.

[63] C. A. Angell, A. Dworkin, P. Figuiere, A. Fuchs, and H. Szwarc. "Strong and fragile plastic crystals." In: *J. Chim. Phys. Phys.- Chim. Biol.* 82 (1985), pp. 773–777.

[64] A. H. Fuchs, J. Virlet, D. Andre, and H. Szwarc. "Glassy crystals. V: structural and dynamic studies of large amplitude molecular motions." In: *J. Chim. Phys. Phys.-Chim. Biol.* 82 (1985), pp. 293–303.

[65] A. Würflinger. "Dielectric studies under pressure of the plastic phases of some alcohols." In: *Berichte der Bunsengesellschaft für physikalische Chemie* 95 (1991), pp. 1040–1046.

[66] Y-S. Kim, T.-H. Kim, H. Lee, and H.-K. Song. "Electronegativity-induced enhancement of thermal stability by succinonitrile as an additive for Li ion batteries." In: *Energy Environ. Sci.* 4 (2011), pp. 4038–4045.

[67] Q. Zhang, K. Liu, F. Ding, W. Li, X. Liu, and J. Zhang. "Safety-reinforced succinonitrile-based electrolyte with interfacial stability for high-performance lithium batteries." In: *ACS Appl. Mater. Interfaces* 9 (2017), pp. 29820–29828.

[68] T. Yan, L. Zhu, Y. Wu, J. Gao, W. Tian, and W. Tang. "Enlarging potential window and enhancing stability of poly (ethylene oxide)-based composite solid electrolyte via succinonitrile additive for advanced solid lithium batteries." In: *Funct. Mater. Lett.* 14 (2021), p. 2141004.

[69] P. Pal and A. Ghosh. "Robust succinonitrile plastic crystal-based Ionogel for all-solid-state Li-ion and dual-ion batteries." In: *ACS Appl. Energy Mater.* 3 (2020), pp. 4295–4304.

[70] H. Fontaine. "Structure et réorientations moléculaires du succinonitrile en phase plastique." PhD thesis. Université des sciences et techniques de lille, June 1973.

[71] S. Das, S. Mitra, J. Combet, R. Mukhopadhyay, and A. J. Bhattacharyya. "Study of solvent relaxation of pristine succinonitrile and succinonitrile–salt mixtures using quasielastic neutron scattering." In: *Solid State Ion.* 279 (2015), pp. 72–77.

[72] K. Adachi, H. Suga, and S. Seki. "Phase Changes in Crystalline and Glassy-Crystalline Cyclohexanol." In: *Bull. Chem. Soc. Jpn.* 41 (1968), pp. 1073–1087.

[73] D. Ceccaldi. "X-ray diffuse scattering by cyclohexanol in the plastic phase: A theoretical model including orientational and translational molecular correlations." In: *Phys. Rev. B* 31 (1985), pp. 8221–8225.

[74] L. P. Singh and S. S. N. Murthy. "Dielectric and calorimetric investigation of an unusual two-component plastic crystal: cyclohexanol-neopentylglycol." In: *Phys. Chem. Chem. Phys.* 11 (2009), p. 5110.

[75] M. Tyagi and S. S. N. Murthy. "Study of the nature of glass transitions in the plastic crystalline phases of cyclo-octanol, cycloheptanol, cyanoadamantane and cis-1, 2-dimethylcyclohexane." In: *J. Chem. Phys.* 114 (2001), pp. 3640–3652.

[76] E. Novak, N. Jalarvo, S. Gupta, K. Hong, S. Förster, T. Egami, and M. Ohl. "Dynamics in the Plastic Crystalline Phases of Cyclohexanol and Cyclooctanol Studied by Quasielastic Neutron Scattering." In: *J. Phys. Chem. B* 122 (2018), pp. 6296–6304.

[77] D. W. James, H. F. Shurvell, and R. M. Parry. "Polymorphism in cyclohexanol: A Raman spectroscopic study." In: *J. Raman Spectrosc.* 5 (1976), pp. 201–209.

[78] R. M. Ibberson, S. Parsons, D. R. Allan, and A. M. T. Bell. "Polymorphism in cyclohexanol." In: *Acta Crystallogr., Sect. B: Struct. Sci* 64 (2008), pp. 573–582.

[79] H. Suzuki, H. Hoshina, and C. Otani. "Kinetics of polymorphic transitions of cyclohexanol investigated by terahertz absorption spectroscopy." In: *Cryst. Growth Des.* 14 (2014), pp. 4087–4093.

[80] D. Reuter, C. Geiß, P. Lunkenheimer, and A. Loidl. "Variation of ionic conductivity in a plastic-crystalline mixture." In: *J. Chem. Phys.* 147 (2017), p. 104502.

[81] R. Brand, P. Lunkenheimer, and A. Loidl. "Relaxations and fast dynamics of the plastic crystal cyclo-octanol investigated by broadband dielectric spectroscopy." In: *Phys. Rev. B: Condens. Matter* 10 (1997), R5713.

[82] M. Shablakh, L. A. Dissado, and R. M. Hill. "Structure and dipole relaxation mechanisms in the cyclic alcohols cyclopentanol to cyclo-octanol." In: *J. Chem. Soc., Faraday Trans. 2* 79 (1983), pp. 369–417.

[83] D. L. Leslie-Pelecky and N. O. Birge. "Dielectric measurement of the model glass transition in orientationally disordered cyclo-octanol." In: *Phys. Rev. B: Condens. Matter* 50 (1994), p. 13250.

[84] Gangasharan and S. S. N. Murthy. "Study of α-, β-, and γ-relaxation processes in some supercooled liquids and supercooled plastic crystals." In: *J. Chem. Phys.* 99 (1993), pp. 9865–9873.

[85] A. A. Baida, A. V. Rudakov, and S. G. Agaev. "Dielectric spectroscopy of monatomic alcohols." In: *Russ. J. Phys. Chem. A* 87 (2013), pp. 645–648.

[86] B. Riechers, K. Samwer, and R. Richert. "Structural recovery in plastic crystals by time-resolved non-linear dielectric spectroscopy." In: *J. Chem. Phys.* 142 (2015).

[87] L. P. Singh and S. S. N. Murthy. "Dielectric and calorimetric investigation of an unusual two-component plastic crystal: cyclohexanol-neopentylglycol." In: *Phys. Chem. Chem. Phys.* 11.25 (2009), pp. 5110–5118.

[88] P. L. Kuhns and M. S. Conradi. "NMR study of molecular motions in cyclohexanol, a glass-forming rotor crystal." In: *J. Chem. Phys* 80 (1984), pp. 5851–5858.

[89] J. B. Lambert, S. C. Johnson, and L. Xue. "Dynamics of five-membered rings in the solid state by nmr spectroscopy." In: *J. Am. Chem. Soc* 116 (1994), pp. 6167–6174.

[90] A. Dworkin, A. H. Fuchs, M. Ghelfenstein, and H. Szwarc. "Cristaux vitreux. I: RMN large bande, thermocourants de dépolarisation et analyse enthalpique dans quelques cycloalcools." In: *J. Phys.* 43 (1982), pp. 21–27.

[91] T. Eguchi, G. Soda, and H. Chihara. "Molecular motion and polymorphic forms in cyclohexanol as studied by nuclear magnetic resonance." In: *JMR* 23 (1976), pp. 55–65.

[92] L. Bonazzola, A. H. Fuchs, J. Roncin, and H. Szwarc. "Glassy crystals. 2. Electron paramagnetic resonance study of molecular motions and free-radical diffusion near the glass transition in cycloalkanols: evidence for chemical diffusion." In: *J. Phys. Chem.* 88 (1984), pp. 3003–3006.

[93] J. Hassoun, K.-S. Lee, Y.-K. Sun, and B. Scrosati. "An advanced lithium ion battery based on high performance electrode materials." In: *J. Am. Chem. Soc.* 133 (2011), pp. 3139–3143.

[94] Q. Wang, L. Jiang, Y. Yu, and J. Sun. "Progress of enhancing the safety of lithium ion battery from the electrolyte aspect." In: *Nano Energy* 55 (2019), pp. 93–114.

[95] T. Sun, Z.-J. Li, H.-G. Wang, D. Bao, F.-L. Meng, and X.-B. Zhang. "A Biodegradable Polydopamine-Derived Electrode Material for High-Capacity and Long-Life Lithium-Ion and Sodium-Ion Batteries." In: *Angew. Chem. Int. Ed.* 55 (2016), pp. 10662–10666.

[96] D. Zhang, C. Tan, T. Ou, S. Zhang, L. Li, and X. Ji. "Constructing advanced electrode materials for low-temperature lithium-ion batteries: A review." In: *Energy Rep.* 8 (2022), pp. 4525–4534.

[97] C. Cao, Y. Zhong, and Z. Shao. "Electrolyte Engineering for Safer Lithium-Ion Batteries: A Review." In: *Chin. J. Chem.* 41 (2023), pp. 1119–1141.

[98] S. K. Heiskanen, J.g Kim, and B. L. Lucht. "Generation and Evolution of the Solid Electrolyte Interphase of Lithium-Ion Batteries." In: *Joule* 3 (2019), pp. 2322–2333.

[99] X-B. Cheng, R. Zhang, Ch.-Z. Zhao, F. Wei, J.-G. Zhang, and Q. Zhang. "A Review of Solid Electrolyte Interphases on Lithium Metal Anode." In: *Adv. Sci.* 3 (2015), p. 1500213.

[100] Z. Li, J. Huang, Bor Y. L., V. Metzler, and J. Zhang. "A review of lithium deposition in lithium-ion and lithium metal secondary batteries." In: *J. Power Sources* 254 (2014), pp. 168–182.

[101] ser_igor. *Li-ion battery diagram stock illustration.* Purchased via iStockphoto: 2023-12-29. URL: https://www.istockphoto.com/en/vector/li-ion-battery-diagram-gm825367806-133778177.

[102] C. T. Imrie, M. D. Ingram, and G. S. McHattie. "Ion transport in glassy polymer electrolytes." In: *J. Phys. Chem. B* 103 (1999), pp. 4132–4138.

[103] M. C Lonergan, A. Nitzan, M. A. Ratner, and D. F. Shriver. "Dynamically disordered hopping, glass transition, and polymer electrolytes." In: *J. Chem. Phys.* 103 (1995), pp. 3253–3261.

[104] C. A. Angell. "Perspective on the glass transition." In: *J. Phys. Chem. Solids.* 49 (1988), pp. 863–871.

[105] N. Okui. "Relationships between melting temperature, maximum crystallization temperature and glass transition temperature." In: *Polymer* 31 (1990), pp. 92–94.

[106] H. Vogel. "Das Temperaturabhangigkeitsgesetz der Viskosität von Flüssigkeiten." In: *Phys. Z.* 22 (1921), pp. 645–646.

[107] G. Tammann and W. Hesse. "The dependence of viscosity upon the temperature of supercooled liquids." In: *Z. Anorg. Allg. Chem* 156 (1926), pp. 245–257.

[108] G. S. Fulcher. "Analysis of recent measurements of the viscosity of glasses." In: *J. Am. Ceram. Soc.* 8 (1925), pp. 339–355.

[109] R. Böhmer and C. A. Angell. "Elastic and viscoelastic properties of amorphous selenium and identification of the phase transition between ring and chain structures." In: *Phys. Rev. B* 48 (1993), p. 5857.

[110] R. Böhmer, K. L. Ngai, C. A. Angell, and D. J. Plazek. "Nonexponential relaxations in strong and fragile glass formers." In: *J. Chem. Phys.* 99 (1993), pp. 4201–4209.

[111] S. Lansab, Ph. Münzner, H. Zimmermann, and R. Böhmer. "Deuteron nuclear magnetic resonance and dielectric studies of molecular reorientation and charge transport in succinonitrile-glutaronitrile plastic crystals." In: *J. Non Cryst. Solids.: X* 14 (2022), p. 100097.

[112] T. Scopigno, G. Ruocco, F. Sette, and G. Monaco. "Is the fragility of a liquid embedded in the properties of its glass?" In: *Science* 302 (2003), pp. 849–852.

[113] A. Vispa, M. Romanini, M. A. Ramos, L. C. Pardo, F. J. Bermejo, M. Hassaine, A. I. Krivchikov, J. W. Taylor, and J. Ll. Tamarit. "Thermodynamic and kinetic fragility of freon 113: The most fragile plastic crystal." In: *Phys. Rev. Lett.* 118 (2017), p. 105701.

[114] E. Kamińska, O. Madejczyk, M. Tarnacka, K. Jurkiewicz, K. Wolnica, W. Edyta Śmiszek-Lindert, K. Kamiński, and M. Paluch. "Anhydrosaccharides—A new class of the fragile plastic crystals." In: *J. Chem. Phys.* 148 (2018).

[115] A. Kubo, A. Yogo, F. Imashiro, and T. Terao. "Deuterium NMR study of the glassy crystal pentachlorotoluene. Hadamard quadrupole-order exchange NMR." In: *J. Chem. Phys.* 100 (1996), pp. 15933–15941.

[116] M. C. Lonergan, D. F. Shriver, and M. A. Ratner. "Polymer electrolytes: The importance of ion-ion interactions in diffusion dominated behavior." In: *Electrochim. Acta* 40 (1995), pp. 2041–2048.

[117] H. Mehrer. *Diffusion in solids: fundamentals, methods, materials, diffusion-controlled processes.* Vol. 155. Springer Science & Business Media, 2007.

[118] A. Kvist and A. Bengtzelius. "Tracer diffusion and electrical conductivity of cubic lthium sulphate and a transport model for cubic sulphates." In: *Fast ion transport in solids, Solid State Batteries and Devices* (1973). Ed. by W. van Gool, pp. 193–199.

[119] B. Jansson and C.-A. Sjöblom. "The rheological properties of AgI and Li_2SO_4 solid electrolytes, I." In: *Rheol. Acta* 16 (1977), pp. 628–634.

[120] B. Jansson and C.-A. Sjöblom. "The rheological properties of AgI and Li_2SO_4 solid electrolytes, II." In: *Rheol. Acta* 20 (1981), pp. 360–369.

[121] A. Benrath and K. Drekopf. "Über die elektrische Leitfähigkeit von Salzen und Salzgemischen." In: *Z. Phys. Chem.* 99 (1921), pp. 57–70.

[122] T. Forland, J. Krogh-Moe, M. Moutschen-Dahmen, B. Noer, and L. Reio. "The Structure of the High Temperature Modification of Lithium Sulfate." In: *Acta Chem. Scand.* 11 (1957), pp. 565–567.

[123] T. Förland and J. Krogh-Moe. "The structure of the high-temperature modification of sodium lithium sulfate." In: *Acta Crystallogr.* 11 (1958), pp. 224–225.

[124] A. Lundén. "Ionic conduction in sulphates." In: *Fast Ion Transport in Solids*. 1993, pp. 181–201.

[125] L. Nilsson, J. O. Thomas, and B. C. Tofield. "The structure of the high-temperature solid electrolyte lithium sulphate at 908K." In: *J. Phys. C: Solid State Phys.* 13 (1980), p. 6441.

[126] R. Tärneberg and A. Lundén. "Ion diffusion in the high-temperature phases Li_2SO_4, $LiNaSO_4$, $LiAgSO_4$ and $Li_4Zn(SO_4)_3$." In: *Solid State Ion.* 90 (1996), pp. 209–220.

[127] R. Kaber, L. Nilsson, N. H. Andersen, A. Lundén, and JO. Thomas. "A single-crystal neutron diffraction study of the structure of the high-temperature rotor phase of lithium sulphate." In: *J. Phys. Condens. Matter* 4 (1992), p. 1925.

[128] M. Ferrario, M. L. Klein, and I. R. McDonald. "Cation transport in lithium sulphate based crystals." In: *Mol. Phys.* 86 (1995), pp. 923–938.

[129] A. Lundén. "On the Paddle-Wheel Mechanism for Cation Conduction in Lithium Sulphate." In: *Z. Nat. Forsch. A* 50 (1995), pp. 1067–1076.

[130] M. Jansen. "Volume effect or paddle-wheel mechanism—fast alkali-metal ionic conduction in solids with rotationally disordered complex anions." In: *Angew. Chem. Int. Ed.* 30 (1991), pp. 1547–1558.

[131] K. Schmidt-Rohr and H. W. Spiess. *Multidimensional solid-state NMR and polymers*. Academic Press, 1994.

[132] M. J. Duer. *Solid state NMR spectroscopy: principles and applications*. John Wiley & Sons, 2008.

[133] J. Keeler. *Understanding NMR spectroscopy*. John Wiley & Sons, 2010.

[134] P. A. Beckmann. "Spectral densities and nuclear spin relaxation in solids." In: *Phys. Rep.* 171 (1988), pp. 85–128.

[135] A. Steigel, H. W. Spiess, and H. W. Spiess. "Rotation of molecules and nuclear spin relaxation." In: *Dynamic NMR spectroscopy*. Springer. 1978, pp. 55–214.

[136] P. Spegt, B. Meurer, and G. Weill. "Deuterium resonance in the solid state. Experimental determination of moments from quadrupolar solid echo with corrections for finite pulse width and bandwidth." In: *J. Phys. E: Sci. Instrum.* 18 (1985), p. 869.

[137] J. F. Hon and PJ. Bray. "Nuclear Quadrupole Coupling Constants of Li 7 in Lithium Compounds." In: *Phys. Rev.* 110 (1958), p. 624.

[138] Böhmer, Geil, and Suter. *Magnetische Resonanz: Echo-Experimente (Versuchsanleitungen)*. Downloaded: 2023-12-01. URL: https://qnap.e3.physik.tu-dortmund.de/suter/Vorlesung/Magnetische_Resonanz_07/4_Echo-Experimente.pdf.

[139] E. O. Stejskal and J. E. Tanner. "Spin diffusion measurements: spin echoes in the presence of a time-dependent field gradient." In: *J. Chem. Phys* 42 (1965), pp. 288–292.

[140] B. Geil. "Measurement of translational molecular diffusion using ultrahigh magnetic field gradient NMR." In: *Concepts Magn. Reson.* 10 (1998), pp. 299–321.

[141] P. T. Callaghan. *Principles of nuclear magnetic resonance microscopy*. Clarendon press, 1993.

[142] G. Fleischer and F. Fujara. "NMR as a generalized incoherent scattering experiment." In: *Solid-State NMR I Methods*. Springer, 1994, pp. 159–207.

[143] A. K. Jonscher. "The 'universal'dielectric response." In: *nature* 267 (1977), pp. 673–679.

[144] P. Debye. "Polar molecules, the chemical catalog company." In: *Inc., New York* 89 (1929).

[145] F. Kremer and A. Schönhals. *Broadband dielectric spectroscopy*. Springer Science & Business Media, 2002.

[146] S. Havriliak and S. Negami. "A complex plane analysis of α-dispersions in some polymer systems." In: *J. Polym. Sci., Part C: Polym. Lett.* Vol. 14. Wiley Online Library. 1966, pp. 99–117.

[147] P. A. M. Steeman and J. Van Turnhout. "Fine structure in the parameters of dielectric and viscoelastic relaxations." In: *Macromolecules* 27 (1994), pp. 5421–5427.

[148] W-M. Kulicke and C. Clasen. *Viscosimetry of polymers and polyelectrolytes*. Springer Science & Business Media, 2004.

[149] A. Ponton and J-L. Grossiord. *La mesure en rhéologie: des avancées récentes aux perspectives*. EDP Sciences, 2021.

[150] A. Golemme, S. Zamir, R. Poupko, H. Zimmermann, and Z. Luz. "Self-diffusion in the plastic phase of succinonitrile by 2H NMR quadrupole echo train." In: *Mol. Phys.* 81 (1994), pp. 569–578.

[151] D. H. Wu, A. D. Chen, and C. S. Johnson. "An improved diffusion-ordered spectroscopy experiment incorporating bipolar-gradient pulses." In: *J. Magn. Reson., Ser. A* 115 (1995), pp. 260–264.

[152] S. Berger and S. Braun. *200 and more NMR experiments*. Wiley-Vch Weinheim, 2004.

[153] D. Reuter, P. Lunkenheimer, and A. Loidl. "Plastic-crystalline solid-state electrolytes: Ionic conductivity and orientational dynamics in nitrile mixtures." In: *J. Chem. Phys* 150 (2019), pp. 27298–27306.

[154] R. Brand, P. Lunkenheimer, and A. Loidl. "Relaxation dynamics in plastic crystals." In: *J. Chem. Phys* 116 (2002), pp. 10386–10401.

[155] R. Böhmer and G. Hinze. "Reorientations in supercooled glycerol studied by two-dimensional time-domain deuteron nuclear magnetic resonance spectroscopy." In: *J. Chem. Phys* 109 (1998), pp. 241–248.

[156] S. Lansab, B. Grabe, and R. Böhmer. "Paddle-wheel mechanism in doped succinonitrile–glutaronitrile plastic electrolyte: a joint magnetic resonance, dielectric, and viscosimetry study of Li ion translational and molecular reorientational dynamics." In: *Phys. Chem. Chem. Phys.* 25 (2023), pp. 9382–9393.

[157] N. Bloembergen, E. M. Purcell, and R. V. Pound. "Relaxation effects in nuclear magnetic resonance absorption." In: *Phys. Rev.* 73 (1948), p. 679.

[158] A. Abragam. *The principles of nuclear magnetism*. 32. Oxford university press, 1961.

[159] H. Nelson, A. Ihrig, .R Kahlau, P. Kibies, S. M. Kast, and R. Böhmer. "Deuteron magnetic resonance and dielectric studies of guest reorientation and water dynamics in six clathrate hydrates containing ring-type guests." In: *J. Non-Cryst. Solids* 407 (2015), pp. 431–440.

[160] J. H. Strange and M. Terenzi. "Self-diffusion in solid succinonitrile by nuclear magnetic resonance." In: *Mol. Phys.* 19 (1970), pp. 275–278.

[161] S. Stapf and R. Kimmich. "Translational versus rotational molecular dynamics in plastic crystals studied by NMR relaxometry and diffusometry." In: *Mol. Phys.* 92 (1997), pp. 1051–1060.

[162] M. Brissaud-Lancin, C. Marhic, and A. Rivére. "Selfdiffusion in 'plastic'succinonitrile (butanedinitrile)." In: *Philos. Mag. A* 53 (1986), pp. 61–72.

[163] H. M. Hawthorne and J. N. Sherwood. "Lattice defects in plastic organic solids. Part 2.—Anomalous self-diffusion in succinonitrile." In: *Trans. Faraday Soc.* 66 (1970), pp. 1792–1798.

[164] T. Schwan. "Scherrheologische und dielektrische Untersuchungen an Lithium-Ionen in Nitril- und Polymermatrizen." Master's thesis. Technische Universität Dortmund, 2023.

[165] S. Lansab, T. Schwan, K. Moch, and R. Böhmer. "Shear rheology senses the electrical room-temperature conductivity optimum in highly Li doped dinitrile electrolytes." In: *J. Chem. Phys* 160 (2024), p. 084503.

[166] M. L. Martins, X. Lin, C. Gainaru, J. K. Keum, P. T. Cummings, A. P. Sokolov, R. L. Sacci, and E. Mamontov. "Structure–Dynamics Interrelation Governing Charge Transport in Cosolvated Acetonitrile/LiTFSI Solutions." In: *J. Phys. Chem. B* 127 (2022), pp. 308–320.

[167] J. R. Green and W. T. Griffith. "Phase transformations in solid cyclohexanol." In: *J. Phys. Chem. Solids* 26 (1965), pp. 631–637.

[168] O. Andersson and R. G. Ross. "Thermal conductivity, heat capacity and phase diagram of cyclooctanol in liquid, solid and glassy crystal states under high pressure." In: *Mol. Phys.* 71 (1990), pp. 523–539.

[169] H. Forsman and O. Andersson. "Dielectric relaxation and a new phase of cyclooctanol at pressures to 1 GPa." In: *J. Non-Cryst. Solids* 131 (1991), pp. 1145–1148.

[170] G. Hinze. "Geometry and time scale of the rotational dynamics in supercooled toluene." In: *Phys. Rev. E* 57 (1998), p. 2010.

[171] J. Beerwerth. "Zentrallinien-NMR an stark quadrupolar gestörten Kernen in molekularen und ionischen Kristallen." PhD thesis. Technische Universität Dortmund, 2022.

[172] S. Schildmann. "Aufklärung der molekularen Dynamik in glasbildenden Monoalkoholen mithilfe der Kernspinresonanz-Spektroskopi." PhD thesis. Technische Universität Dortmund, 2012.

[173] L. Van Eijck, A. S. Best, S. Long, F. Fernandez-Alonso, D. MacFarlane, M. Forsyth, and G. J. Kearley. "Localized relaxational dynamics of succinonitrile." In: *J. Phys. Chem. C* 113 (2009), pp. 15007–15013.